UNIVERSITY OF CALIFORNIA, SAN DIEGO

High Efficiency Planar and RFIC-Based Antennas for Millimeter-Wave Communication Systems

A dissertation submitted in partial satisfaction of the
requirements for the degree
Doctor of Philosophy

in

Electrical Engineering (Electronic Circuits and Systems)

by

Ramadan A. Alhalabi

Committee in charge:

Professor Gabriel M. Rebeiz, Chair
Professor Gert Cauwenberghs
Professor William S. Hodgkiss
Professor Lawrence E. Larson
Professor Kevin B. Quest

2010

ProQuest LLC
789 East Eisenhower Parkway
P.O. Box 1346
Ann Arbor, MI 48106-1346

The dissertation of Ramadan A. Alhalabi is approved, and it is acceptable in quality and form for publication on microfilm and electronically:

_____

_____

_____

_____

_____

Chair

University of California, San Diego

2010

DEDICATION

To my parents, Abdulraheem and Layla
My wife, Alaa and our sons, Osama and Abdulraheem
and
To my brothers and sisters

TABLE OF CONTENTS

LIST OF FIGURES

LIST OF TABLES

ACKNOWLEDGEMENTS

First and foremost, I would like to sincerely thank my advisor Prof. Gabriel M. Rebeiz for his unlimited support throughout my doctoral program. It was very much a pleasure to meet him and work with him, and it is a great honor for me to be one of his students. I also would like to thank Prof. Rebeiz so much for helping me to get a nice job as RF engineer at Cavendish-Kinetics, Inc. His support and strong recommendations were the main keys behind my successful job interviews with Cavendish-Kinetics.

Next, I would like to thank my dissertation committee members, Prof. Lawrence E. Larson, Prof. Kevin B. Quest, Prof. Gert Cauwenberghs and Prof. William S. Hodgkiss. I also thank the center for wireless communications (CWC) and Intel corporation for supporting my PhD projects.

I thank my colleagues for giving me a lot of support and making my long journey more cheerful. My thanks go to all of the TICS group including Michael Chang, Chris Galbraith, Carson White, Byung-Wok Min, Sang-June Park, Jeonggeun Kim, Balaji Lakshminarayana, Mohammad El-Tanani, Tiku Yu, Sangyoung Kim, Kwangjin Koh, Isak Reines, Jason May, Alex Girchner, DongWoo Kang, Jung-Mu Kim, Berke Cetinoneri, Yusuf Atesal, Chirag Patel, Kevin Ho, Mehmet Uzunkol, Jennifer M. Edwards, Woorim Shin, Donghyup Shin, Yu-Chin Ou, Ozgur Inac, Yi-Chyun Chiou, Chih-Chieh Cheng and special thanks for Dr. Rashed Mahameed and Hojr Sedaghat Pisheh for their great help in the clean room during the fabrication of my antennas.

My special and deepest appreciations go to my family in Gaza for encouraging me and supporting me to complete my PhD. Completing my PhD would not have been possible without their support and encouragement. I also sincerely thank my wife Alaa for her great support and patience all the time during my PhD. Our sons, Osama and Abdulraheem have also great impact on our life. Since we were blessed with them, they made our life full with joy, happiness and a lot of excitement.

My thanks extends also to all the friends I met in San Diego especially the following friends and their families: Dr. Rashed Mahameed, Dr. Fadi Khraim, Dr. Wael Aldelaimy, Dr. Ahmad Kousba, Sharif Albattekhi and Dr. Khaled Almaleh. I also thank my friends, Mohammad Mushtaha and Musbah Shaath for hosting me in Jordan when I was applying for my visa. My deep thanks also go to My friends Mohammad Alashqar, Ahmad El-Tanani, Rami Alroubi and Mohammad Altalmas for their great support especially in the first few months for me in San Diego.

Chapter 2 is mostly a reprint of the material as it appears in IEEE Transactions on Antennas and Propagation, 2008. Ramadan A. Alhalabi; Gabriel M. Rebeiz. The dissertation author was the primary author of this material.

Chapter 3, in part, is mostly a reprint of the material as it appears in IEEE Transactions on Antennas and Propagation, 2009. Ramadan A. Alhalabi; Gabriel M. Rebeiz. The dissertation author was the primary author of this material. Chapter 3, in part, is also mostly a reprint of the material as it appears in IEEE Transactions on Antennas and Propagation, 2010. Ramadan A. Alhalabi; Gabriel M. Rebeiz. The dissertation author was the primary author of this material.

Chapter 4 is mostly a reprint of the material that is submitted for publications in IEEE Transactions on Antennas and Propagation, 2010 . Ramadan A. Alhalabi; Yi-Chyun Chiou; Gabriel M. Rebeiz. The dissertation author was the primary author of this material.

Chapter 5 is mostly a reprint of the material that is submitted for publications in IEEE Transactions on Antennas and Propagation, 2010 . Ramadan A. Alhalabi; Gabriel M. Rebeiz. The dissertation author was the primary author of this material.

Chapter 6 is mostly a reprint of the material that is submitted for publications in IEEE Transactions on Antennas and Propagation, 2010 . Ramadan A. Alhalabi; Gabriel M. Rebeiz. The dissertation author was the primary author of this material.

Ramadan A. Alhalabi
La Jolla, CA
April, 2010.

VITA

1998 - 2003	B. S. in Electrical Engineering, Islamic University of Gaza, Gaza Strip, Palestine
2006 - 2008	M. S. in Electrical Engineering, University of California, San Diego, USA
2008 - 2010	Ph. D. in Electrical Engineering, University of California, San Diego, USA

PUBLICATIONS

R. A. Alhalabi and G. M. Rebeiz,"High-Efficiency Angled-Dipole Antennas for Millimeter-Wave Phased Array Applications," *IEEE Transactions on Antennas and Propagation*, vol. 56, no. 10 , pp. 3136−3142, October 2008.

R. A. Alhalabi and G. M. Rebeiz,"High-Gain Yagi-Uda Antennas for Millimeter-Wave Switched-Beam Systems," *IEEE Transactions on Antennas and Propagation*, vol. 57, no. 11 , pp. 3672−3676, November 2009.

R. A. Alhalabi and G. M. Rebeiz,"Differentially-fed millimeter-wave Yagi-Uda antennas with folded dipole feed," *IEEE Transactions on Antennas and Propagation*, vol. 58, no. 3 , pp. 966−969, March 2010.

R. A. Alhalabi and G. M. Rebeiz,"Planar Millimeter-Wave Monopole Antennas," *submitted for publication in IEEE Transactions on Antennas and Propagation*, January 2010.

R. A. Alhalabi and G. M. Rebeiz,"High-Efficiency On-Chip Electromagnetically-Coupled MM-Wave Silicon Microstrip Antennas," *submitted for publication in IEEE Transactions on Antennas and Propagation*, January 2010.

R. A. Alhalabi and Y. Chiou and G. M. Rebeiz,"Self-Shielded High-Efficiency Yagi-Uda Antennas for 60 GHz Communications," *submitted for publication in IEEE Transactions on Antennas and Propagation*, April 2010.

J. W. May and R. A. Alhalabi and G. M. Rebeiz,"A 3 G-Bit/s W-Band SiGe ASK Receiver with a High-Efficiency On-Chip Electromagnetically-Coupled Antenna," *to be presented at the IEEE 2010 Radio Frequency Integrated Circuits (RFIC) Symposium.*, May 2010.

Y. A. Atesal and B. Cetinoneri and R. A. Alhalabi and G. M. Rebeiz,"Wafer-Scale W-Band Power Amplifiers Using On-Chip Antennas," *to be presented at the IEEE 2010 Radio Frequency Integrated Circuits (RFIC) Symposium.*, May 2010.

Yi-Chyun Chiou and Ramadan A. Alhalabi and Gabriel M. Rebeiz,"High-Efficiency 60 GHz Dipole-Box Antennas," *to be presented at the IEEE 2010 Symposium on Antennas and Propagation*, July 2010.

W. Shin and M. Uzunkol and Ramadan A. Alhalabi and Gabriel M. Rebeiz,"60 GHz Low Power 1.5 Gb/s ASK Transmitter in 90 nm CMOS with On-Board Yagi-Uda Antenna," *to be presented at the 2010 European Microwave Week*, September 2010.

ABSTRACT OF THE DISSERTATION

High Efficiency Planar and RFIC-Based Antennas for Millimeter-Wave Communication Systems

by

Ramadan A. Alhalabi

Doctor of Philosophy in Electrical Engineering (Electronic Circuits and Systems)

University of California, San Diego, 2010

Professor Gabriel M. Rebeiz, Chair

The dissertation presents the design and measurements of several planar and RFIC-based high efficiency antennas for mm-wave applications. The high-efficiency microstrip-fed endfire angled-dipole antenna is designed mainly for phased-array applications. It is built on both sides of a Teflon substrate ($\epsilon_r = 2.2$) and allows a wideband feed from the single-ended microstrip line to the differential dipole. The design results in wide radiation patterns for scanning purposes with a gain of around 2.5 dB at 20 - 26 GHz and a cross-polarization level of $<$ -15 dB at 24 GHz. A mutual coupling of $<$ -23 dB is measured between adjacent elements with 6.8 mm center-to center spacing (0.50 - 0.54λ_0 at 22 - 24 GHz). A variant of the angled-dipole antenna with a magnetic ground plane edge was also developed, and shows a measured gain of $>$ 6 dB at 23.2 - 24.6 GHz and very low mutual coupling between elements ($<$ -23 dB for a 6.8 mm spacing). Both

antennas result in a radiation efficiency of $> 93\%$ when referenced to the microstrip line feed. The usefulness of these antennas as phased-array radiators is demonstrated by several eight-element linear arrays at 22 - 24 GHz with scan angle up to 50°.

High-efficiency microstrip-fed and CPS-fed Yagi-Uda antennas have also been developed for point-to-point millimeter-wave communication systems. The antennas are built on Teflon substrates ($\epsilon_r = 2.2$); and utilize 5 directors to result in a gain of 8 - 12 dB at 24 GHz and 60 GHz. A mutual coupling of $<$ -20 dB is measured between two microstrip-fed Yagi-Uda antennas with a center-to center spacing of 8.75 mm ($0.7\lambda_0$ at 24 GHz), and a two-element array results in a measured gain of 11.5-13.0 dB at 22-25 GHz. The planar Yagi-Uda antennas result in high radiation efficiency ($> 90\%$) and is suitable for short-range mm-wave radars and high data-rate communication systems. A differential version was also developed using a folded dipole feed and is compatible with fully-differential RFICs.

Self-shielded microstrip-fed Yagi-Uda antenna has also been developed for 60 GHz communications. The antennas are built on a Teflon substrates ($\epsilon_r = 2.2$) with a thickness of 10 mils (0.254 mm). A 7-element design results in a gain $>$ 9.5 dB at 58 - 63 GHz. The antenna shows excellent performance in free space and in the presence of metal-planes used for shielding purposes. A parametric study is done with metal plane heights (h) from 2 mm to 11 mm, and the Yagi-Uda antenna results in a gain $>$ 12 dB at 58 - 63 GHz for h = 5 - 8 mm. A 60 GHz four-element switched-beam Yagi-Uda array is also presented with top and bottom shielding planes, and allows for 180° angular coverage with $<$ 3 dB amplitude variations. This antenna is ideal for inclusion in complex platforms, such as laptops, for point-to-point communication systems, either as a single element or a switched-beam system.

MM-wave planar monopole antennas have been also demonstrated. A triangular and a straight monopole antennas result in a measured $S_{11} <$ -10 dB at 20.7 - 37.9 GHz and 18 - 42 GHz respectively. Both antennas are suitable for ultra-wideband applications. These antennas show omni-directional patterns over almost the whole bandwidth but with high cross-polarization levels ($\sim$ equal to the co-polarization level). An alternate monopole design with a localized folded current choke was developed and results in lower cross-polarization levels (-6 dB), but with $S_{11} <$ -10 dB at 23.1 - 26.7 GHz. A variant of this design with a magnetic ground plane results in substantial reduction in the cross-polarization level (-13 dB) but with a bandwidth of only 1 GHz ($S_{11} <$ -10 dB

at 23.5 - 24.8 GHz). The measured gain of the antennas are in the range of -4.0 dB to + 2.9 dB, depending on the design, and with high radiation efficiency ($> 90\%$).

Finally, a W-band high-efficiency, electromagnetically-coupled on-chip silicon microstrip antenna has been demonstrated. The antenna is composed of a quartz substrate placed on top of a commercial low-resistivity SiGe BiCMOS silicon chip. Design criteria for the microstrip antenna taking into account the dielectric and metal-density rules for the different layers of the BiCMOS silicon chip are presented. The antenna results in $S_{11} <$ -10 dB at 91.7 - 98.5 GHz, a gain of 0.7 - 3.9 dB and a radiation efficiency of 44 +/- 13% at 91 - 100 GHz. The design is scalable to NxM elements and to wafer-scale arrays. To our knowledge, this is the first high-efficiency Silicon wafer-scale antenna to date.

Chapter 1

Introduction

1.1 Planar Antennas at mm-Wave Frequencies

The millimeter-wave band is defined as the portion of the electromagnetics spectrum extending from 30 - 300 GHz with corresponding wavelengths range of 10 - 1 mm. Historically, mm-wave frequencies were used mostly for defense and radio astronomy applications mainly because of the high cost and limited availability of electronic devices at these frequencies. The recent advancement of silicon technology and the rapidly growing mm-wave applications markets (such as automotive radars, high-resolution imaging and high-definition video transfer requirements) necessitate the development of broadband, highly integrated, low power and low cost wireless systems including high-efficiency planar antennas.

Integrated planar antennas have gained a lot of interest in the past years for mm-wave applications due to their low cost, ease of fabrication and potential for high efficiency operation. The small wavelength at mm-wave frequencies is an advantage for the design of small and efficient antennas. The size of the antenna is determined by the laws of physics; and for efficient radiation, the antenna size should be of the order of half wavelength or larger. Therefore, for f = 30 - 300 GHz (λ = 10 - 1 mm), it is feasible to build antennas that are physically small and at the same time electrically large enough to radiate efficiently. However, at mm-wave frequencies the losses are generally higher than at lower frequencies; and the antenna designer needs to carefully design the antenna and choose the appropriate substrate to minimize losses and achieve high radiation efficiency.

1.2 Previous Work on mm-Wave Planar and On-chip Antennas

1.2.1 Planar Antennas

Several planar antennas have been widely used at mm-wave frequencies for different applications, and the tapered slot antenna (TSA) is one of most prevalent designs. It can be designed to have a very wide bandwidth and a relatively high gain. However, it is usually several wavelength long and suffers from relatively high cross-polarization levels. A comprehensive study of tapered slot antennas is found in [1, 2]. A 60 GHz Fermi tapered slot antenna with improved radiation patterns is presented in [3, 4] where the authors have introduced corrugations in the side edges of the slot antenna ground plane to control the edge currents and as a result, improve the radiation patterns and lower the side lobes. Sato et al. used the same concept to design a narrow-width Fermi tapered slot antenna with symmetrical E- and H-plane patterns for imaging arrays [5]. Rizk and Rebeiz presented a 90 GHz Fermi tapered slot antenna on 100 μm-thick silicon substrate [6] where they selectively micromachined holes in the Silicon substrate to reduce its effective dielectric constant and improve the radiation patterns of the antenna. Schoenlinner et al. introduced a wide scanning angle radar array utilizing tapered slot antennas and a spherical Teflon lens for use at 77 GHz [7]. Recently, a compact 60 GHz tapered slot antenna fabricated on a low permittivity LCP substrate was presented in [8].

A more compact planar antenna that can be designed to achieve relatively high gain and low cross-polarization levels but with narrower bandwidth compared to the tapered slot antenna is the planar Yagi-Uda antenna. The Quasi-Yagi antenna presented in [9, 10] at X-band is built on a high dielectric constant substrate ($\epsilon_r = 10.2$) and based on the generation of a TE_0 surface wave along the dielectric substrate and the reflection of this mode from a truncated ground plane. The antenna shows a broad-band characteristics of 48% bandwidth for SWR < 2. It also showed a 3 - 5 dB gain with $>$ 12 dB front-to-back ratio and $<$ -15 dB cross-polarization level. Grajek et al. presented an alternate design of a Yagi-Uda antenna on a thin low dielectric constant substrate ($\epsilon_r = 2.2$) [11] and used two directors and one reflector printed on the back-side of the substrate to achieve a directivity of 9.3 dB at 24 GHz.

The Yagi-Uda antennas presented in [9–11] utilize planar microstrip-to-coplanar

stripline (CPS) transition which is based on a half-wave delay line to achieve the 180° phase shift for the balanced dipole feed, and the frequency dependence of the balun limits the antenna performance versus frequency. A simplified feeding for the Yagi-Uda antenna that overcomes the issue of using $\lambda/2$ delay line by putting the dipole arms on both sides of the antenna substrate and feeding it using a parallel strip feed is presented in [12]. This feeding mechanism allows for wide-band transition to the antenna but at the expense of an increase in the cross-polarization level. The cross-polarization level increase depends on the substrate thickness and it is mainly due to the vertical component of the electric field between the dipole arms built on both sides of the substrate. This puts a limit on the allowed substrate thickness for applications which require low cross-polarization levels. A 38 GHz Yagi-Uda antenna using this feeding structure is presented in [13].

Another antenna suitable for mm-wave applications is the integrated horn antenna [14–19]. The integrated horn antenna can achieve high gain, high efficiency and wide operation bandwidth. It can be used as a single element or in a 2-dimensional arrays, but it usually requires special fabrication process and occupies a relatively large area. Arrays of conical horn antennas are presented in [20, 21]. Recently, an endfire CPW-fed 60 GHz integrated horn antenna is presented in [22] with a gain of 14.4 dB.

These antennas are directional antennas suitable for radars, phased arrays and other point-to-point mm-wave communication systems. Omnidirectional and relatively low gain antennas have been also used at mm-wave frequencies for broadcasting and base-station applications. A wide-band high efficiency folded dipole antennas are presented in [23, 24] for 60 GHz applications.

1.2.2 On-Chip Antennas

The antennas presented before can be integrated with mm-wave transceiver integrated circuits (ICs) using different methods such as using bond-wires, flip-chips, etc. However, for more integration and in order to minimize the losses and other mismatch effects encountered with interconnects to the on-board antennas, it is preferable to have the antenna integrated directly on the chip. On-Silicon-chip antennas usually suffer from low radiation efficiency due to the high dielectric losses in the low-resistivity silicon substrate (0.1 - 10 Ω-cm) and also due to the increased coupling into the substrate modes exited in the 250 - 750 μm thick substrate which is electrically-thick at mm-wave frequencies.

Several on-chip antennas have been previously presented at mm-wave frequencies. On-chip inverted-F and quasi-Yagi antennas are presented in [25] for 60 GHz applications. Both antennas suffer from the high dielectric losses in the low-resistivity (10 Ω-cm) silicon substrate. And although these antennas have the advantage of being directly integrated on the Silicon-chip, both antennas have very low gain and are not suitable for most mm-wave applications. The inverted-F antenna has a gain of -19 dB and the quasi-Yagi antenna has a gain of -12 dB. A 60 GHz on-chip dipole antenna fabricated with a 0.18 μm CMOS process is presented in [26] with a measured gain of -10 dB and simulated radiation efficiency of only 16%. A 24 GHz dipole antenna fabricated on a 10 Ω-cm silicon substrate is presented in [27] and demonstrated a gain of -8 to -10.5 dB. A 60 GHz CPW-fed on-chip triangular monopole antenna is presented in [28] and with a gain of $\sim$ -8.7 dB and a simulated efficiency of 12%. A dipole based on-chip antenna fabricated on a semi-insulating GaAs substrate with low loss tangent (tanδ = 0.005) is presented in [29] and showed a measured gain of 3.6 dB with VSWR $<$ 2 at 55 - 70 GHz. Also, 60 GHz dipole antenna fabricated on thick resin layer on the back side of a silicon chip with a simulated gain of 5.4 dB and a measured gain of 3.1 dB is presented in [30]. Both the GaAs antenna and the silicon-resin antenna require special substrate. A 140 GHz on-chip antenna with a gain of -25 dB gain is presented in [31].

Recently, integrated bondwire antennas have been used for mm-wave applications. A triangular bond-wire loop antenna adjacent to a lossy silicon substrate is presented in [32]; the antenna has a simulated gain of -0.4 dB at 60 GHz and a measured gain of 0.9 dB using a scaled model at 2 GHz. A gold bondwire with $\sim$1 mil diameter is presented as an antenna for 60 GHz short range high data-rate communication links at 60 GHz [33]. A Yagi-Uda array of six wire-bonds with a measured gain of 8 dB at 40 GHz and 82.5% radiation efficiency is presented in [34]. Although this antenna achieves high gain and radiation efficiency, it occupies a large space on wafer, and is not suitable for dense integrated circuits.

1.3 Thesis Overview

Planar antennas are an important part of any wireless system especially at mm-wave frequencies. In receivers, the losses in the antenna are the first losses encountered in the receive chain and contribute directly to the receiver noise figure. In transmitters, power generation is hard and expensive at mm-wave frequencies and it is necessary to

minimize the power losses in the antenna. Therefore it is necessary to have high-efficiency antennas that can transfer the input RF power into radiated electromagnetic waves with minimum amount of loss. This dissertation presents several high-efficiency planar and RFIC-based antennas for different mm-wave applications.

Chapter 2 presents a high-efficiency endfire angled-dipole antenna for phased array applications. The dipole antenna results in a wide beamwidth for wide angle scanning purposes. It also results in reduced mutual coupling, and has a wide frequency response. The antenna is characterized theoretically and experimentally versus frequency and substrate height, and particular attention is given to the cross-polarization level which is shown to be strongly dependent on the substrate height. Also, a novel design with a magnetic ground plane edge is also presented with a higher gain and still very low mutual coupling between adjacent elements. An 8-element array with 45° - 50° scan angle is built and measured at 22 - 24 GHz with the two different antennas, and both result in excellent performance.

Chapter 3 presents a seven-element microstrip-fed Yagi-Uda antenna with high gain, wide bandwidth and low cross-polarization levels. Two-element arrays with a center-to-center spacing of 8.75 mm ($0.7\lambda_0$ at 24 GHz) are also presented. The chapter also presents fully-differential mm-wave Yagi-Uda antenna using a Coplanar stripline (CPS) feed and shows very low cross-polarization levels (-25 dB).

In chapter 4, a microstrip-fed 60 GHz 7-element Yagi-Uda antenna with self-shielding capabilities is presented. The antenna is built on a Teflon substrate and its performance is characterized in free space and next to two metal sheets placed on top and bottom with different spacings. It is also characterized inside a metal shield four sides (top, bottom and with side-walls). The antenna is insensitive to its surrounding and can be embedded inside complex platforms such as laptops or mobile phones. A four-element switched-beam array based on Yagi-Uda antennas is also presented. This array allows for 180° coverage with < 3 dB amplitude variations over the 180° angle.

In Chapter 5, a microstrip-fed planar mm-wave straight and triangular monopole antennas with ultra wideband impedance matching bandwidth and with almost omni-directional radiation patterns over the whole bandwidth are presented. Also, two other modified planar monopole antennas with reduced cross-polarization levels are presented. The new designs are based on a localized current choke which greatly attenuates the ground plane edge current and reduces the cross-polarization level. This results in im-

proved patterns and lower cross-polarization but with a smaller impedance bandwidth.

Chapter 6 presents a high-efficiency electromagnetically-coupled W-band on-chip microstrip antenna. The antenna design eliminates the effects of the silicon substrate by shielding the microstrip antenna using a ground plane made from the above silicon metallization layers. However, the thickness of the metal/SiO_2 layers above the silicon substrate is only 10-12 μm in most RF processes (IBM 8HP, 9RF, etc.) and it is hard to build efficient antennas with such a ground spacing. A 125 μm substrate is therefore added on top of the silicon chip so as to have enough ground-plane spacing for efficient radiation. The antenna results in S_{11} < -10 dB at 91.7 - 98.5 GHz, a gain of 0.7 - 3.9 dB and a radiation efficiency of 44 +/- 13% at 91 - 100 GHz. The design is scalable to NxM elements and to wafer-scale arrays. To our knowledge, this is the first high-efficiency Silicon wafer-scale antenna to date.

Chapter 2

Endfire Angled-Dipole Antennas for Millimeter-Wave Phased Array Applications

2.1 Introduction

For phased-array systems, the antenna should have wide beamwidth in the scanning plane, low mutual coupling and a wide frequency of operation. Recently, Eldek et al. presented dipole antennas for C and X-band applications with a simple modified feed, and demonstrated a two-element array [35]. Chen et al. also showed a dipole antenna with a microstrip tapered balun at 2.5 GHz [36]. A low gain Yagi-Uda antenna and a bow-tie antenna with microstrip baluns were demonstrated by Zhen et al. at 8-11 GHz with excellent performance [12], [37], and the quasi-Yagi antenna developed by Deal et al. also showed good performance at X-band and mm-wave frequencies [9], [**?**] with a 180° planar balun. Grajeck et al. showed a planar high-gain Yagi-Uda antenna at 24 GHz [11], but this antenna is not suitable for phased array applications due to its high directivity. Finally, a printed dipole antenna with an integrated balun was used by Sowers et al. for high efficiency 94 GHz phased arrays [38].

This chapter presents a microstrip-fed dipole antenna with the dipole arms angled to 60° compared to a flat (0°) design. This design results in a wide beamwidth and reduced mutual coupling, and has a wide frequency response. The antenna is characterized theoretically and experimentally versus frequency and substrate height, and

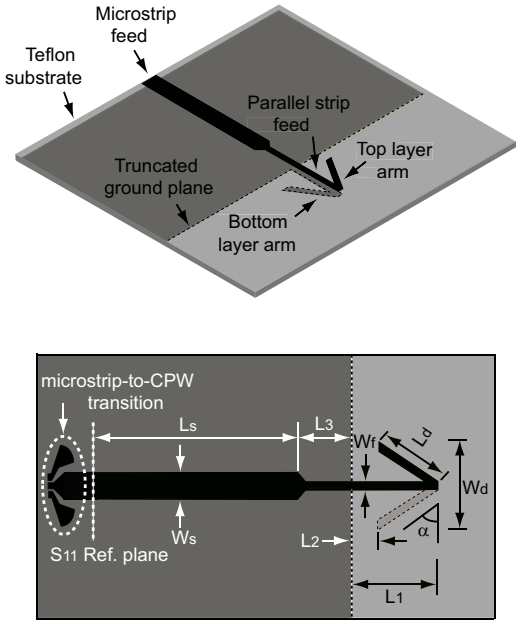

Figure 2.1: Angled-dipole antenna geometry: α= 60°, W_s = 1.2, W_f = 0.4, W_d = 3.7, L_1 = 3.9, L_2 = 1.2, L_3 = 2.2, L_d = 3.3, L_s = 23 and ground plane width = 26 (all dimensions are in mm).

particular attention is given to the cross-polarization level which is shown to be strongly dependent on the substrate height. Also, a novel design with a magnetic ground plane edge is also presented with a higher gain and still very low mutual coupling between adjacent elements. An 8-element array with 45° - 50° scan angle is built and measured at 22 - 24 GHz with the two different antennas, and both result in excellent performance.

2.2 Single Element Design And Measurements

2.2.1 Design

The layout of the angled-dipole antenna is shown in Fig. 2.1. The antenna consists of two identical 60° angled arms, one on the top-side and the other on the bottom-side of the substrate. The antenna is printed on a Rogers RT/Duroid 5880 substrate (ϵ_r=2.2) with a thickness of 15 mils (0.381 mm). The 60° angle was chosen to get the widest E-plane beamwidth for scanning purposes, and also results in low mutual coupling between adjacent elements. The antenna is designed to have an input

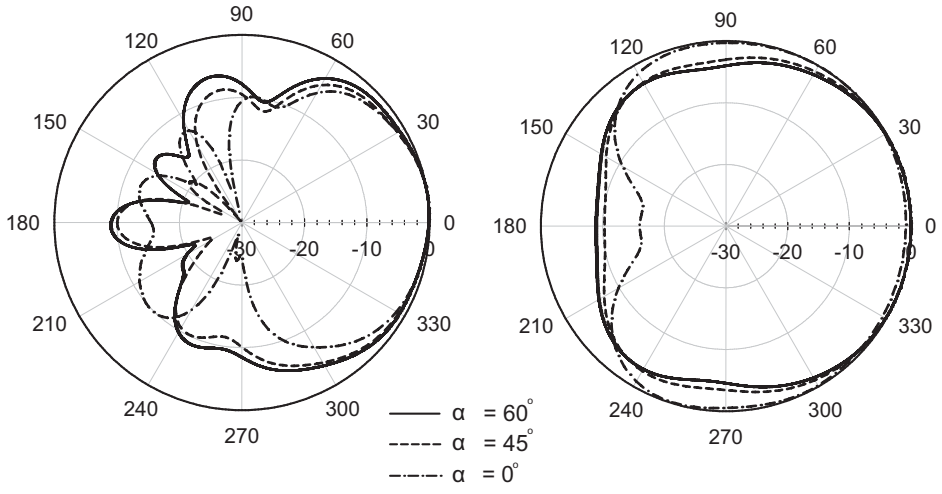

(a) (b)

Figure 2.2: Simulated radiation patterns at 24 GHz for three different angles: (a) E-plane, (b) H- plane.

impedance of 50 Ω and is connected to a microstrip line with W_s = 1.2 mm ($Z_\circ$ = 50 Ω). The antenna is fed by a parallel-plate transmission line of width W_f = 0.4 mm and impedance $Z_f \simeq$ 130 Ω, and this transmission line becomes a microstrip feed line of length L_3 = 2.2 mm and impedance Z_1 = 93 Ω (see Fig. 2.1). The feed design follows ideas presented in [35–37] where the balun between the microstrip feed and the balanced dipole feed is built using the top and bottom-sides of the Teflon substrate. The truncated microstrip ground plane is placed at L_1 = 3.9 mm from the dipole apex and acts as a reflector to result in a unidirectional dipole pattern. The simulated radiation patterns at 24 GHz of the angled-dipole are presented in Fig. 2.2 for $\alpha = 60°$, 45° and 0° designs. The calculated directivities using Ansoft-HFSS [39] are 2.8, 3.1 and 3.0 dB with an associated cross-polarization level of -10.5, -11.3, and -11.9 dB for the 60°, 45° and 0° dipoles, respectively (ϵ_r=2.2, t = 15 mils). The front-to-back power ratio is 9-10 dB for all designs due to the imperfect ground plane reflector. It is clear that the 60° design results in the widest E-plane pattern with only 2.0 dB drop at 50° off broadside, and is excellent for phased array applications. The H-plane pattern for all three antennas is very wide as shown in Fig. 2.2(b).

The antenna impedance for the 60° angled-dipole design is simulated using an abrupt transition and a transition taper in the ground plane (Fig. 2.3). In both cases, the top metal line remains unchanged. The simulated input impedance results in a

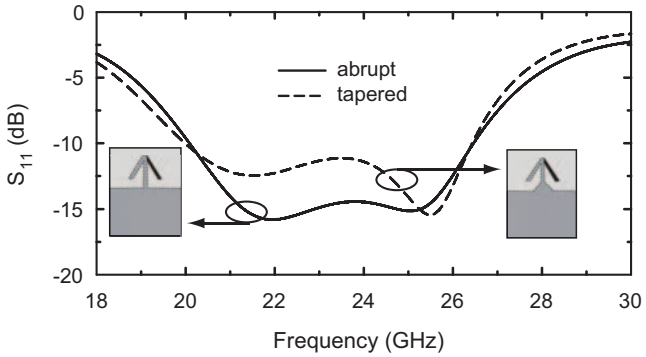

Figure 2.3: Simulated S_{11} of the 60° angled-dipole for abrupt and tapered ground plane transitions.

slightly better match for the abrupt transition. In our opinion, both abrupt and tapered transitions can be designed to yield a similar response if the top metal line is optimized for every design.

The mutual coupling between two angled-dipole antennas spaced 6.8 mm apart (0.50 - 0.54λ_0 at 22 - 24 GHz) is simulated with HFSS for three different angles. The 60° angled-dipole offers the lowest mutual coupling for all three designs (Fig. 2.4). It is not clear why there is a strong dip in the mutual coupling at 21 - 25 GHz for the 60° case, but even without this dip, this design still offers the lowest mutual coupling response. Fig. 2.5 shows the simulated 60° angled-dipole co- and cross-polarization patterns at 24 GHz for a 5, 10, 15 and 20 mils substrate thickness. The antenna dimensions were slightly modified so that the antenna resonates at 24 GHz for each case. It is seen that the cross-polarization level increases as the substrate thickness increases (Table 2.1). The

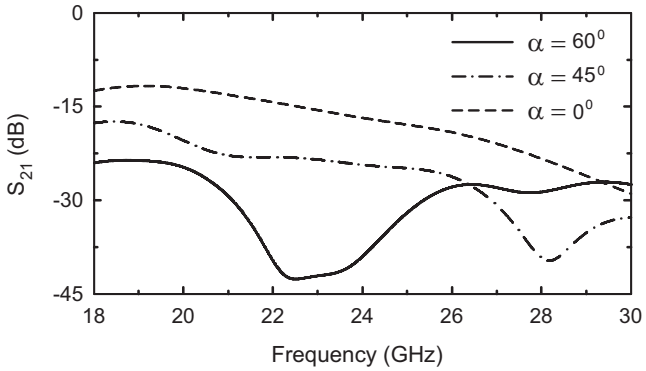

Figure 2.4: Simulated mutual coupling (S_{21}) for the three different dipole designs. Each antenna was designed to have a 50 Ω input impedance.

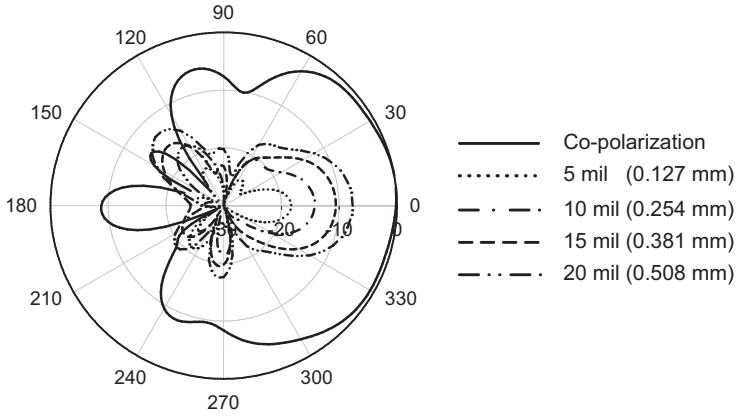

Figure 2.5: Simulated co- and cross-polarization of the 60° angled-dipole at 24 GHz for different substrate thickness.

Table 2.1: Simulated cross-polarization level vs. substrate thickness at 24 GHz.

Substrate Thickness (mil/mm)	X-pol Level (dB)
5 / 0.127	-18.0
10 / 0.254	-14.0
15 / 0.381	-10.5
20 / 0.508	-7.4

cross-polarization is mainly due to the vertical fields between the dipole arms placed at the two different substrate levels. It is clear that the maximum allowable substrate thickness is 15 mils at 24 GHz for relatively low cross-polarization levels.

2.2.2 Impedance and Pattern Measurements

The 60° angled-dipole impedance is measured using a ground-signal-ground CPW probe with a microstrip-to-CPW transition (see Fig. 2.1). A standard TRL calibration was done in order to remove the effect of the CPW-to-microstrip transition and bring the reference plane to the one indicated in Fig. 2.1. The measured S_{11} agrees well with HFSS simulation and it is below -10 dB from 20.0 to 26.2 GHz (Fig. 2.6(b)). The impedance measurements were also done using the microstrip to coaxial-line transition shown in Fig. 2.6(a) and result in essentially the same impedance.

The radiation patterns are measured in the receive mode using a zero-bias schottky diode detector (Krytar model 303B) and a lock-in amplifier (Stanford Research

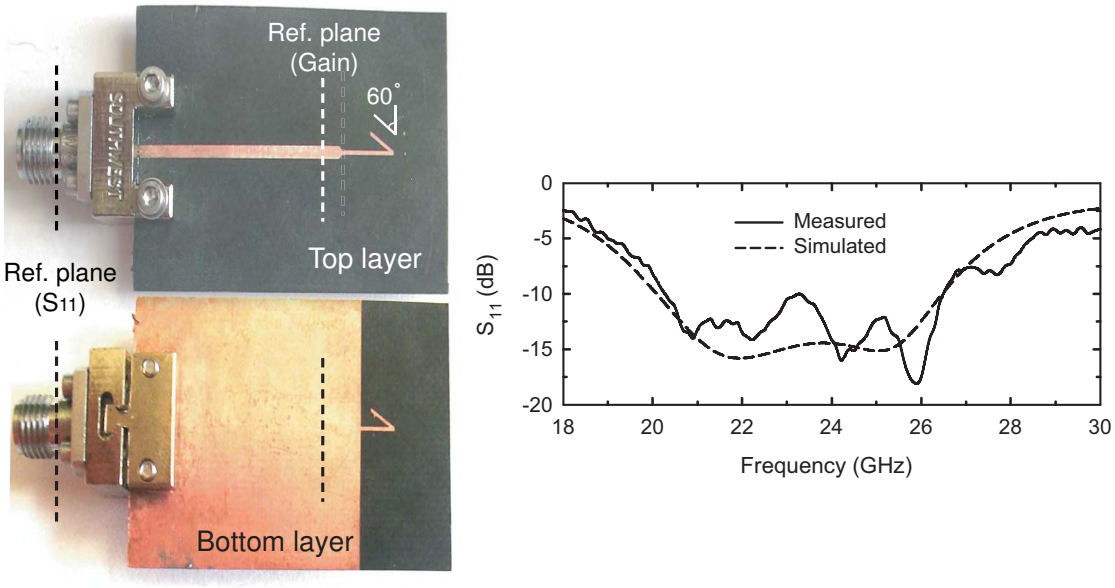

(a) (b)

Figure 2.6: (a) Fabricated 60° angled-dipole antenna. The ground plane width is 26 mm and the microstip line length is 21 mm, (b) measured and simulated S_{11}.

Systems, SR830 DSP Lock-in Amplifier). The diode detector was connected to the microstrip feed line using a high performance Southwest Microwave 2.92 mm connector [40]. The RF signal is amplitude modulated with a 1 kHz sine-wave signal and the rectified 1 kHz is measured using the lock-in amplifier. A thin absorber is used over the coaxial connector and the diode detector to reduce its scattering effects. The measured patterns agree well with HFSS simulations and show a wide radiation patterns over the whole antenna bandwidth (Fig. 2.7). The measured on-axis cross-polarization level is lower than predicted ($\sim$ -16.5 dB compared to -10.5 dB at 24 GHz). We believe that this is due to slight scattering from the coaxial connector which is reducing the cross polarization level.

2.2.3 Gain Measurements

The absolute gain of the 60° angled-dipole was measured using a standard gain (horn) antenna (Dorado GH-42-20 [41]). A 2.92 mm Southwest microwave connector is used with the angled-dipole antenna to minimize the reflection at the connector and maximize the measured power. The received power is measured using a calibrated Agilent Power Meter (E4417) [42], and this same power meter is used to measure the transmit

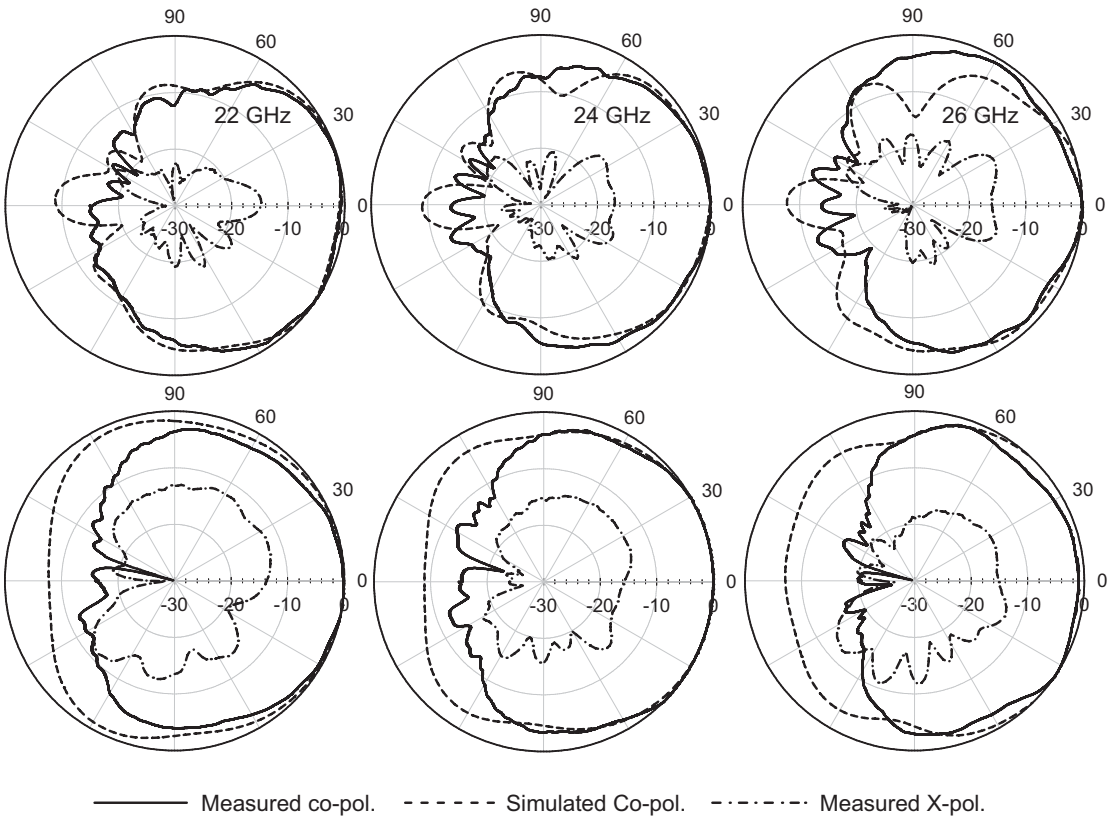

Figure 2.7: E-plane (top) and H-plane (bottom) radiation patterns of the 60° angled-dipole antenna.

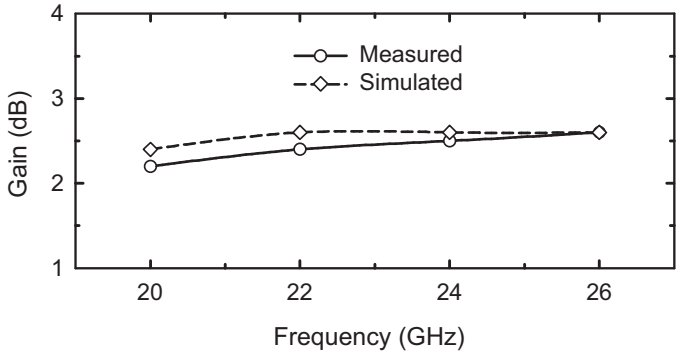

Figure 2.8: Measured and simulated gain vs. frequency for the 60° angled-dipole antenna.

power. The gain of the 60° angled-dipole is then obtained using the Friis transmission formula. The antenna impedance mismatch is not taken out of the measurement. However, the loss of the microstrip line between the antenna and the Southwest connector was measured independently and was taken out of the measurements (0.46 dB). This places the reference plane at the microstrip line as seen in Fig. 2.6(a). Fig. 2.8 presents the measured 60° angled-dipole gain at 20, 22, 24 and 26 GHz. The measured gain is approximately constant over the antenna bandwidth and has a value of about 2.5 dB. Ansoft-HFSS reported gain is 2.6 dB with a directivity of 2.82 dB at 24 GHz and the difference is mostly due to impedance mismatch (see Fig. 2.6(b)). The 60° angled-dipole antenna has a measured efficiency of ∼93% (including mismatch loss), within the +/-0.1 dB measurement error.

2.2.4 Angled-Dipole with a Corrugated (Magnetic) Ground-Plane Edge

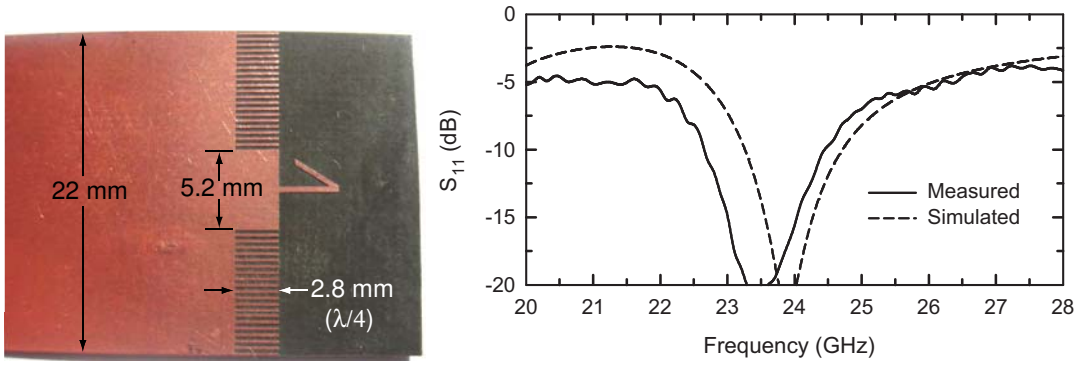

(a) (b)

Figure 2.9: (a) Bottom side of the fabricated 60° angled-dipole with ground plane corrugations, (b) measured and simulated S_{11}.

The measured radiation patterns of the angled-dipole in Fig. 2.7 show a front-to-back ratio of about 10 dB. One way to get a better front-to-back ratio is by optimizing the width of the reflector (the ground plane edge). The effective width of the ground plane edge can by decreased by introducing $\lambda/4$-length corrugations in the ground plane as shown in Fig. 2.9(a) [43]. These corrugations introduce a magnetic plane and greatly attenuate the lateral edge currents. The corrugations are 2.8 mm long, 0.2 mm wide and with a gap of 0.2 mm, resulting in ∼30 corrugations per λ. A parametric study was done with HFSS for different ground plane widths behind the dipole (no corrugations) and it was found that a width of 4 - 6 mm results in the highest gain and best front-to-back

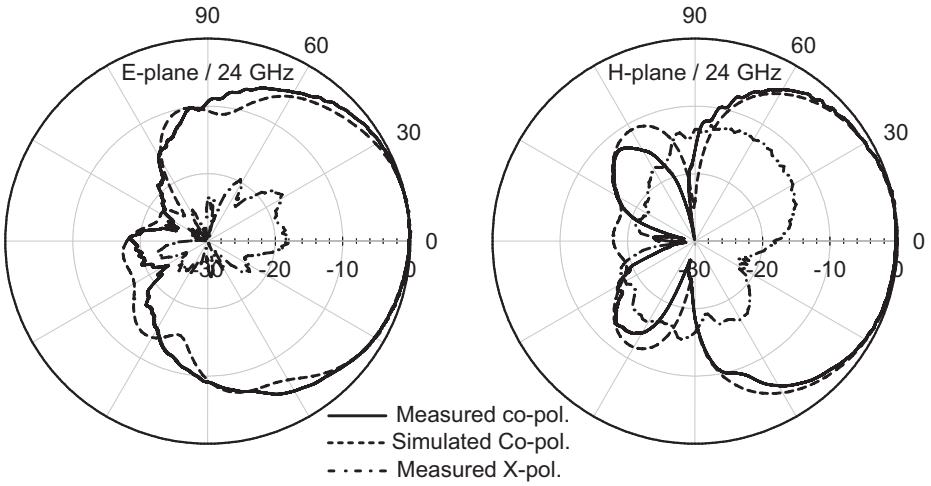

Figure 2.10: Radiation patterns of the 60° angled-dipole with ground plane corrugations at 24 GHz.

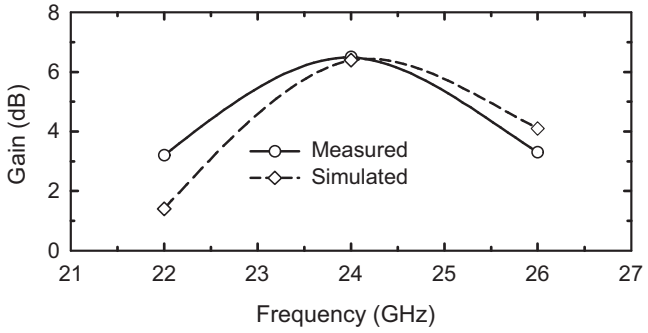

Figure 2.11: Measured and simulated gain vs. frequency for the 60° angled-dipole with ground plane corrugations.

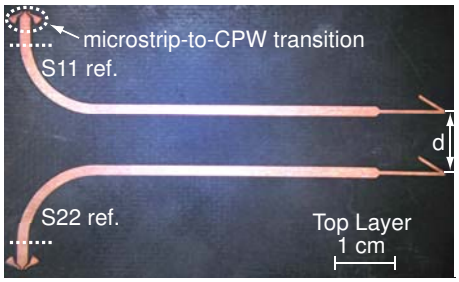

(a)

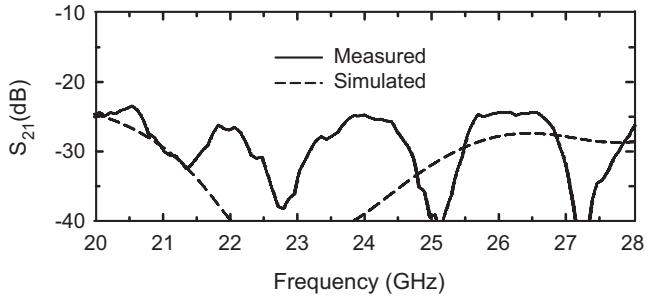

(b)

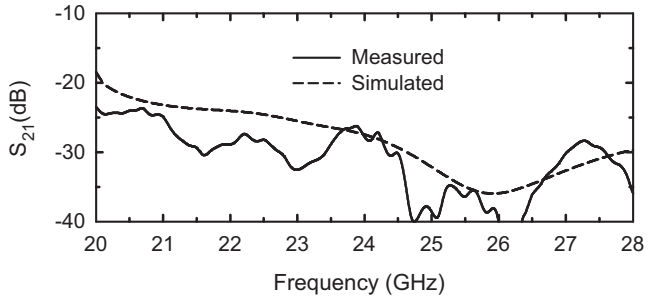

(c)

Figure 2.12: (a) Fabricated two 60° angled-dipoles with a center-to-center spacing of d = 6.8 mm (top layer). Measured mutual coupling (S_{21}) (b) without ground plane corrugations, (c) with ground plane corrugations.

ratio. A ground plane width of 5.2 mm was chosen for demonstration as seen in Fig. 2.9(a) (compared to the 22 - 26 mm ground plane width for the original design).

The angled-dipole with a corrugated (magnetic) ground plane results in S_{11} < -10 dB from 22.5 - 24.5 GHz compared to 20.0 - 26.2 GHz for the original design (Fig. 2.9(b)), and agrees well with simulations. The design results in a higher front-to-back ratio of about 19 dB at 24 GHz (as compared to only 10 dB for the standard design) and also a much narrower H-plane pattern (Fig. 2.10). The E-plane shows a 3.2 dB drop at 50° off-broadside (as compared to 2.0 dB for the standard design), and the on-axis

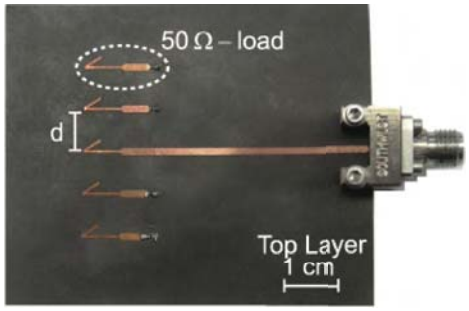

Figure 2.13: Fabricated five 60° angled-dipoles for active pattern measurements (top side), d = 6.8 mm.

cross-polarization levels remains at -17 dB. The measured absolute gain is 6.5 dB at 24 GHz (HFSS predicted 6.4 dB) and is higher than the 2.5 dB gain for the original design (Fig. 2.11). The gain enhancement is due to the E- and H-plane pattern narrowing and the reduced power in the back lobe. The corrugated (magnetic) ground plane edge results in a highly efficient antenna which is well suited for phased-array applications.

2.3 Antenna Array Measurements

2.3.1 Mutual Coupling

The mutual coupling between two 60° angled-dipole antennas for both designs (with and without ground plane corrugations) is measured using the antenna layout shown in Fig. 2.12(a). Again, TRL calibration is used to calibrate out the CPW-to-microstrip transition effects. The angled-dipoles were fabricated with a center to center spacing of 6.8 mm (0.50 - 0.54λ_0 at 22 - 24 GHz). The measurement shows a mutual coupling < -23 dB over a very wide bandwidth (Fig. 2.12(b), 2.12(c)). The 50 Ω microstrip line loss is 0.22 dB/cm at 24 GHz and contributes only 1.8 dB to the measured S_{21} between the antennas.

2.3.2 Active Pattern Measurements

The active E- and H-plane patterns of the angled-dipoles (with and without ground plane corrugations) were also measured using five elements with a center-to-center spacing of 6.8 mm (Fig. 2.13). Four of the antennas were terminated with 50 Ω and the patterns of the center element were measured and are shown in Fig. 2.14. The measured active patterns are very close to the single-element patterns due to the low

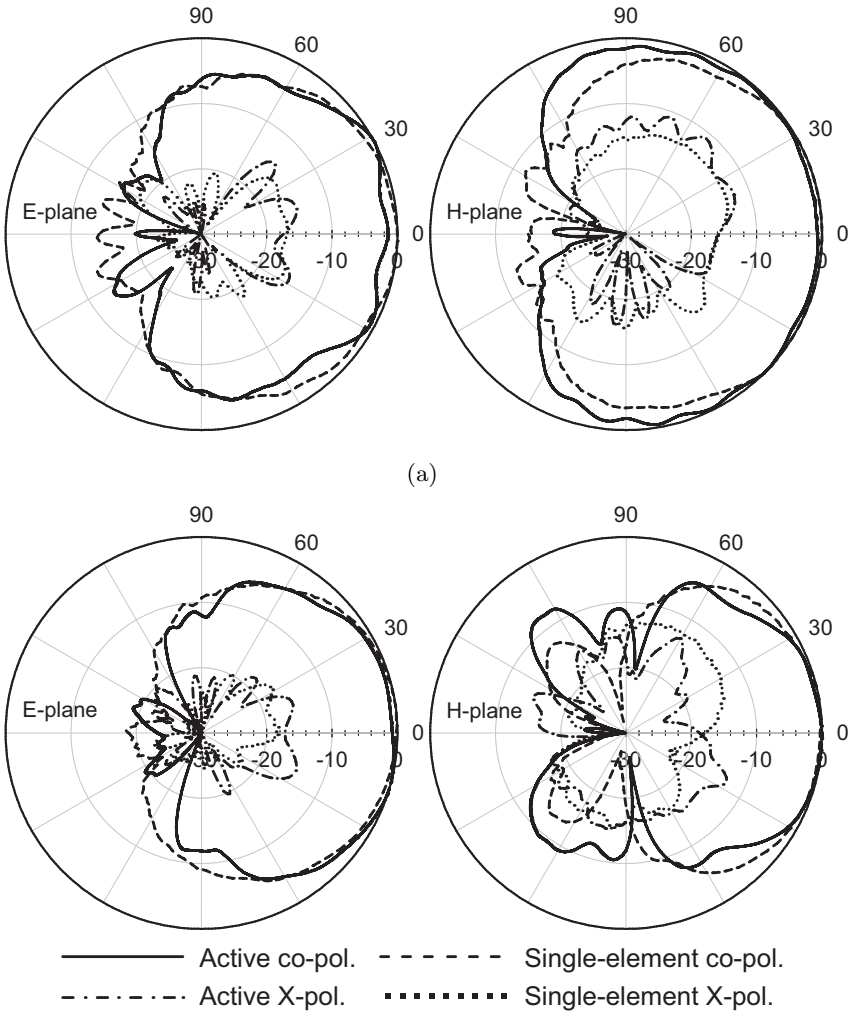

(a)

(b)

Figure 2.14: Measured active radiation patterns at 24 GHz:(a) without ground plane corrugations,(b) with ground plane corrugations.

mutual coupling between the elements.

2.3.3 Eight-Element Array Measurements at 22 - 24 GHz

Several eight-element linear arrays with a center to center spacing of 6.8 mm (0.50 - 0.54λ_0 at 22 - 24 GHz) and different fixed scanning angles were fabricated and tested (Fig. 2.15(a), 2.15(b)). The measured input impedance for the 8-element arrays is shown in Fig.2.15(c), and the measured S_{11} is $<$ -8dB from 20 - 26 GHz ($<$ -10 dB from 21.5 - 26 GHz). The measurement above 26 GHz is limited by the coaxial calibration

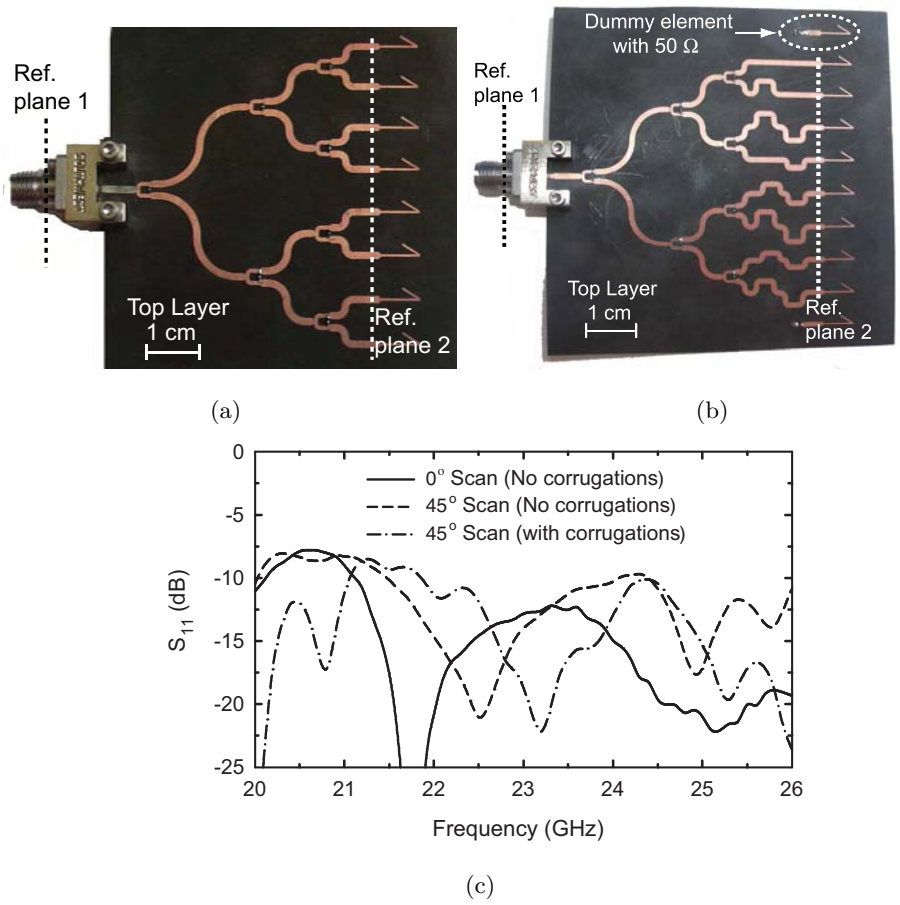

Figure 2.15: Fabricated eight-element array: (a) without scanning, (b) with 45° fixed scan angle at 24 GHz (50° scan at 22 GHz), (c) measured S_{11}.

kit. The array feed is a standard corporate design with Wilkinson couplers and off-chip 100 Ω resistors. The array in Fig. 2.15(b) employs fixed microstrip line delays in order to achieve a 45° scan angle at 24 GHz (50° scan at 22 GHz). The measured E-plane radiation patterns show good agreement with simulations and a cross-polarization level of about -12 to -13 dB (Fig. 2.16). The measured 3 dB beamwidth at 24 GHz is 17° and 16° for the scanned 8-element arrays with and without corrugations, respectively. The measured cross-pol. level agrees well with the simulated values of $\sim$ -11 dB (Table 2.1). In this case, the connector plays a minor role since it is far away from the radiators and scatters differently from the 8 radiating antennas. As expected, there is a grating lobe in the 45° scanned pattern at 24 GHz due to the $0.54\lambda_0$ spacing between the elements. It is clear from Fig. 2.16(b), 2.16(c) that the grating lobe level at 24 GHz for the case with the corrugated (magnetic) ground plane is lower than for the standard dipole ground plane

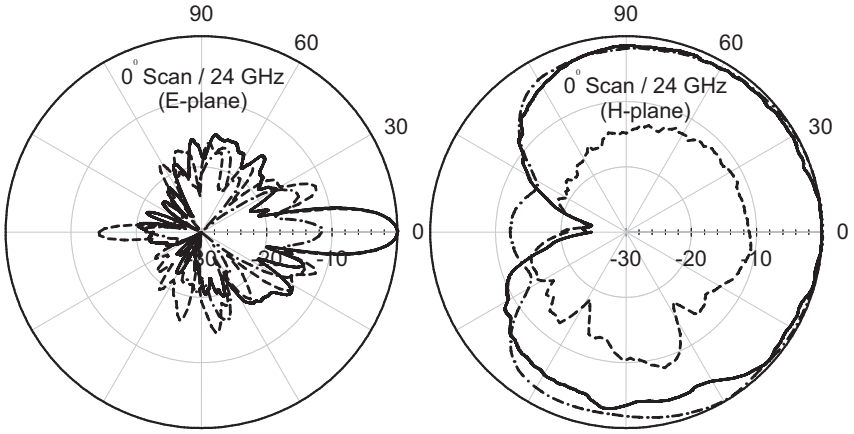

(a)

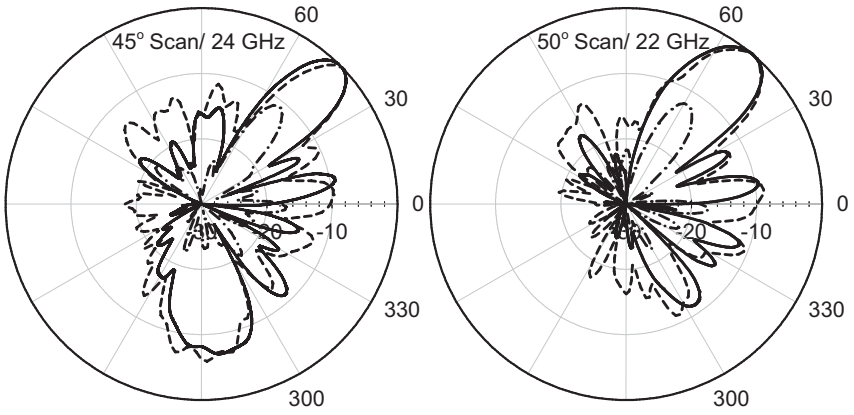

(b)

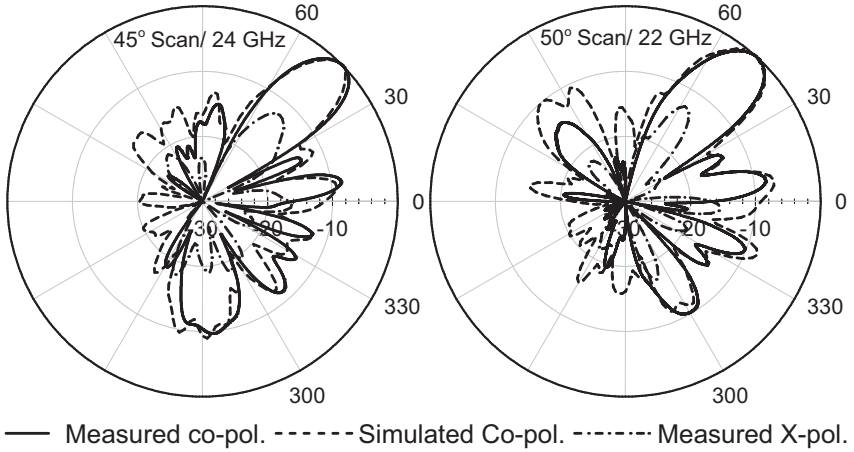

(c)

Figure 2.16: Eight-element array E-plane radiation patterns: (a) without scanning, (b) with ground plane corrugations, (c) withot corrugations.

due to the E-plane element pattern. The 8-element array pattern with no scanning is also shown in Fig. 2.16(a) and agrees well with simulations with a 3 dB beamwidth of 12°.

A gain of 10.7 dB and 8.3 dB (at Ref. plane 1) were measured at 24 GHz for the 8-element, 45° scanned arrays with and without ground plane corrugations, respectively. The estimated loss between Ref. plane 1 and 2 in Fig. 2.15(b) is ∼1.6 dB (transmission line loss, 3x Wilkinson coupler loss) and therefore, the measured gains of the 8-element 45° scanned arrays at Ref. plane 2 are 12.3 and 9.9 dB with and without ground plane corrugations, respectively. The simulated HFSS gains for these scanned arrays are 12.0 dB and 10.6 dB, respectively, and good agreement is achieved between measurements and simulations. The antenna array with a corrugated ground plane resulted in a 2.4 dB increase in the measured gain at a 45° scan angle due to a narrower E- and H-plane element patterns and lower backside radiation. A gain of 9.9 dB was measured at Ref. plane 1 for the 8-element un-scanned array without ground plane corrugations. The estimated loss between Ref. planes 1 and 2 is ∼1.3 dB, and therefore the measured gain of the 8-element un-scanned array is 11.2 dB at Ref. plane 2 (HFSS predicted gain = 11.6 dB). No gain measurements were done for the un-scanned array with ground plane corrugations, and HFSS predicted gain is 13.9 dB. The 8-element array measurements are summarized in Table 2.2.

Table 2.2: Summary of 24 GHz 8-element array measurements.

	0º/without corrugations	45º/without corrugations	45º/with corrugations
E-plane 3 dB BW	12º	16º	17º
H-plane 3 dB BW	169º	NA	NA
Measured Gain	11.2	9.9	12.3
Simulated Gain	11.6	10.6	12.0

2.4 Extension to 60 GHz

Fig. 2.17(a) presents the 60 GHz 45° angled-dipole antenna fabricated on a Rogers RT/Duroid 5880 substrate (ϵ_r=2.2) with a thickness of 10 mils (0.254 mm). As presented in Fig. 2.2, a wide beamwidth is achieved for α = 45° and 60° and we

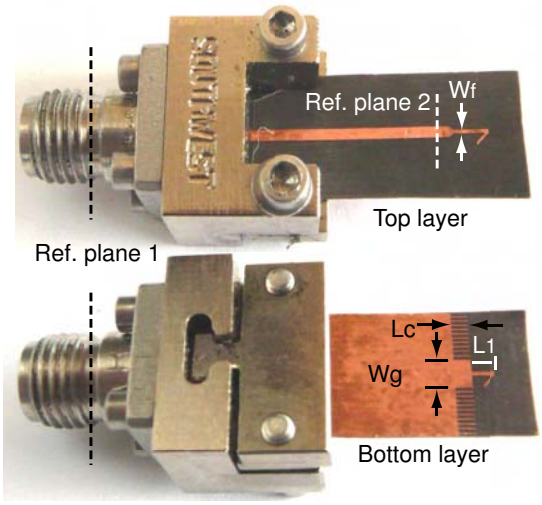

(a)

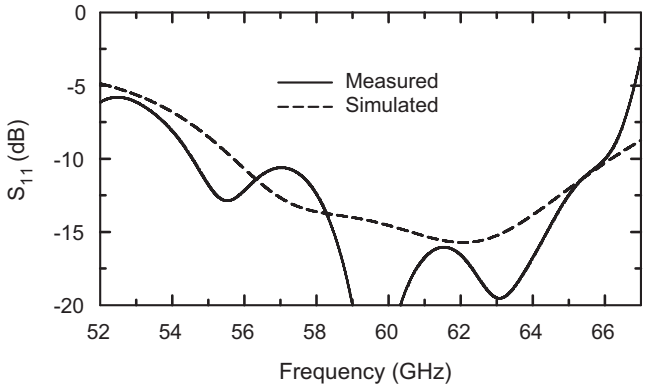

(b)

Figure 2.17: (a) Fabricated 60 GHz 45° angled-dipole antenna: $W_f = 0.3$, $W_g = 2.1$, $L_1 = 1.6$, $L_c = 1.1$, ground plane width = 8 (all dimensions are in mm), (b) measured and simulated S_{11} at Ref. plane 1.

have chosen $\alpha = 45°$ for the 60 GHz angled-dipole implementation. The angled-dipole antenna consists of two 45° angled arms, one on the top-side and the other on the bottom-side of the substrate. It is designed for an input impedance of 50 Ω and is fed by a microstrip line with $W_s = 0.8$ mm (50 Ω). As in the 24 GHz case, the balun between the microstrip feed and the balanced dipole feed is built using the top and bottom-sides of the Teflon substrate to allow a wideband antenna feed. The truncated microstrip ground plane is placed at 1.5 mm from the dipole apex and acts as a reflector so as to result in a unidirectional dipole pattern. Also, $\lambda/4$-deep corrugations were introduced in the ground-plane edge to form a magnetic ground plane edge that stops the lateral edge

current and enhances the antenna gain. The corrugations have a length, width, spacing

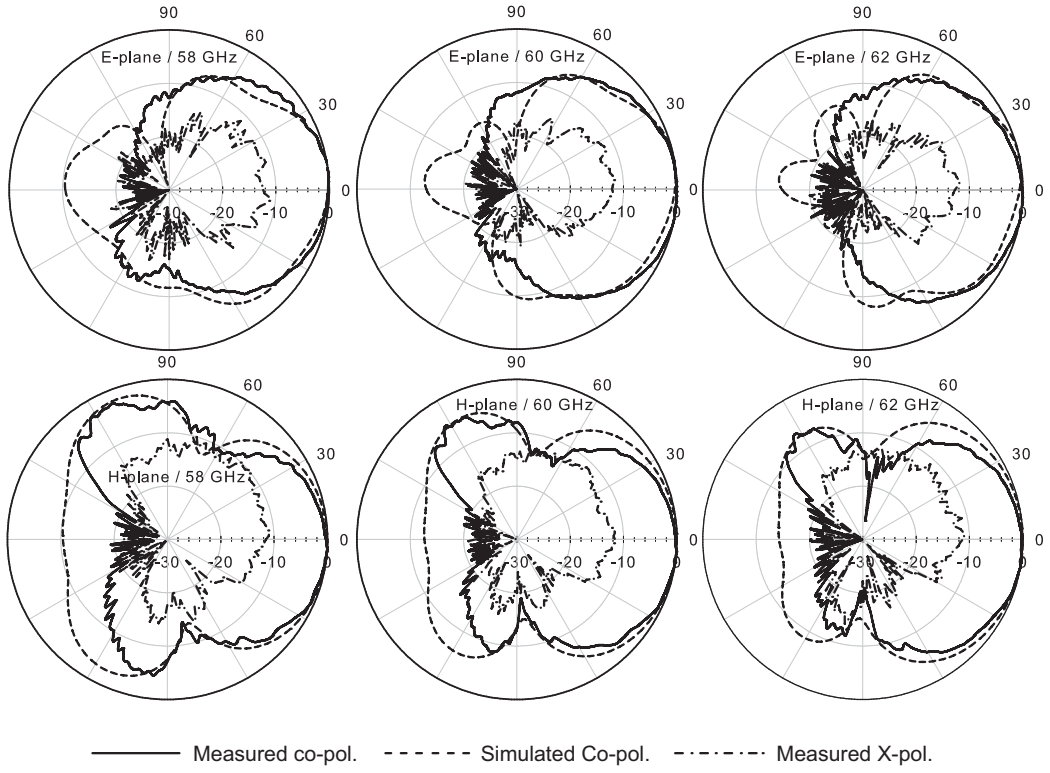

Figure 2.18: Radiation patterns of the 60 GHz 45° angled-dipole antenna.

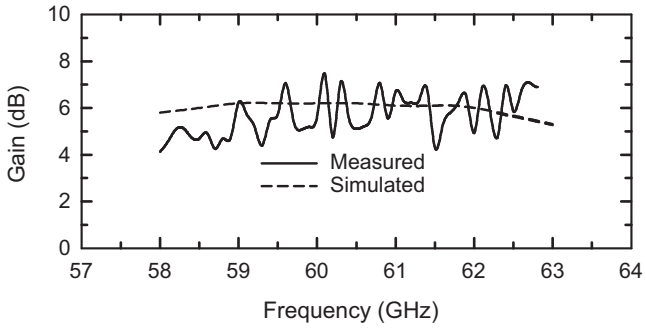

Figure 2.19: Measured and simulated gain of the 60 GHz 45° angled-dipole antenna.

of 1.1, 0.2, and 0.2 mm, respectively, and can be easily obtained using a copper etching process.

2.4.1 Impedance and Radiation Patterns Measurements

The input impedance of the 60 GHz 45° angled-dipole antenna is measured with a 67 GHz network analyzer (Agilent E8361A) using a 2.4 mm Southwest microwave connector (Fig 2.17(a)). Good agreement is obtained between the measured and simulated S_{11}. The 60 GHz 45° angled-dipole has a measured S_{11} < -10 dB from 55.5 to 66.8 GHz (Fig. 2.17(b)). The radiation patterns of the 60 GHz 45° angled-dipole antenna are measured in the receive mode using a 40 - 60 GHz waveguide diode detector (Pacific-Millimeter model UD) and a lock-in amplifier (Stanford Research Systems, SR830). The diode detector is connected to the 2.4 mm connector using a WR-19 coaxial-to-waveguide adapter. The RF signal is amplitude modulated with a 1 kHz sine-wave signal and the rectified 1 kHz is measured using the lock-in amplifier. A thin absorber is used over the connector and the diode detector to reduce its scattering effects. The measured patterns agree well with HFSS simulations as shown in Fig. 2.18.

2.4.2 Gain Measurements

The absolute gain of the 60 GHz 45° angled-dipole antenna is measured with a network analyzer (Agilent PNA network analyzer E8361A) using the gain transfer method. Two identical standard gain (horn) antennas are first connected to the two ports of the network analyzer and S_{21} is measured. The gain of the standard gain horn antennas is calculated from the measured S_{21} using the Friis transmission formula. One horn antenna is then replaced by the 60 GHz 45° angled-dipole antenna and the gain of the 60 GHz 45° angled-dipole antenna is obtained from the difference in the measured S_{21} in both cases. The measured gain of the 60 GHz 45° angled-dipole antenna is shown in Fig. 2.19. The losses of the microstrip line and the 2.4 mm Southwest connectors were measured separately. The measured loss of the microstrip line is ∼0.8 dB/cm while the connector has a loss of ∼0.9 dB at 60 GHz and these were taken out from the measured gain. The antenna impedance mismatch is included in the measured gain. The ripples in the measured gain are mainly due to scattering effects from the connector which was not covered by absorbers during the gain measurements. The measured gain of the angled-dipole antenna at Ref. plane 2 is > 4 dB from 58 to 63 GHz.

2.5 Conclusion

End-fire dipole antennas with applications as single element radiators and for phased-array systems at 24 and 60 GHz are presented. A new technique of using $\lambda/4$-length corrugations to stop the ground plane edge currents and form a magnetic ground plane edge is introduced. The antenna gain, front-to-back ratio and H-plane patterns are significantly enhanced with the use of a corrugated (magnetic) ground plane edge. The antennas result in relatively wideband operation (10-20%), low cross-polarization levels, and very high measured radiation efficiency ($> 93\%$). These planar antennas can be scaled to 77 GHz or 94 GHz for automotive radars and high data-rate communication systems.

Chapter 2 is mostly a reprint of the material as it appears in IEEE Transactions on Antennas and Propagation, 2008. Ramadan A. Alhalabi; Gabriel M. Rebeiz. The dissertation author was the primary author of this material.

Chapter 3

High-Gain Millimeter-Wave Planar Yagi-Uda Antennas

Planar Yagi-Uda antennas can be designed to achieve high gain and relatively low cross-polarization at mm-wave frequencies. The antenna can be fed either by microstrip line or using a coplanar stripline (CPS). The CPS feed is compatible with differential RFIC input/output ports and can be used to feed a dipole directly without any baluns [44].

Previously, Kaneda et al. presented a microstrip-fed Quasi-Yagi antenna at X-band with a gain of 3 - 5 dB and a cross-pol. level of $<$ -15 dB [10]. Grajek et al. showed a Yagi-Uda antenna with a directivity of 9.3 dB at 24 GHz [11]. These antennas utilize planar microstrip-to-coplanar stripline (CPS) transition which is based on a half-wave delay line to achieve the 180° phase shift for the balanced dipole feed, and the frequency dependence of the balun limits the antenna performance versus frequency. A Yagi-Uda antenna with one director, a truncated ground plane acting as a reflector and with a simplified feeding structure is presented by Zheng [12] where the balun between the microstrip feed and the balanced dipole feed is built using the top and bottom-sides of the substrate. Lee and Chung presented a 38 GHz microstrip-fed Yagi-Uda antenna which uses 6 directors and the microstrip ground plane as a reflector to achieve a gain of 9.5 dB [13]. DeJean and Tentzeris presented a high gain microstrip Yagi array with high front to back ratio [45]. Woo et al. presented a microstrip-fed Yagi-Uda antenna with a new microstrip-to-CPS transition [46]. This new transition performs the required field and impedance match between the microstrip line and the CPS feed line using via

holes. Using one director and one reflector, this antenna showed a gain of 5.2 - 5.8 dB with a bandwidth of 29.1% from 30 to 40 GHz. H. K. Kan et al. showed a CPW-fed Quasi-Yagi antenna with a 44% 10 dB impedance matching bandwidth at X-band [47]. Recently, Hsu et. al. showed a 60 GHz CPW-fed on-chip Yagi-Uda antenna with a gain of -10 dB [48].

This chapter presents a seven-element microstrip-fed Yagi-Uda antenna with high gain (> 10 dB), wide bandwidth (22-26 GHz) and low cross-polarization levels (-18 dB). The antenna utilizes five directors, and the truncated ground plane acts as a reflector to maximize the antenna gain. Two-element arrays with a center-to-center spacing of 8.75 mm ($0.7\lambda_0$ at 24 GHz) are also presented. The chapter also presents fully-differential mm-wave Yagi-Uda antenna using a CPS feed. This antenna showed very low cross-polarization (-25 dB) and excellent patterns over the 22-26 GHz range. The application areas are in planar antennas having medium to high gain for short-range mm-wave links, both as single units or as a switched-beam system.

3.1 Microstrip-fed Yagi-Uda Antenna

3.1.1 Antenna Design

The microstrip-fed Yagi-Uda antenna is built on a Rogers RT/Duroid 5880 substrate (ϵ_r=2.2) with a thickness of 15 mils (0.381 mm) and utilizes five directors (Fig. 3.1). The directors are printed on the top side of the substrate with a director-to-director spacing d = 2.4 mm. The initial dimensions of the antenna were obtained from tables for maximum directivity in air [49] and then scaled to compensate for the duroid substrate ($\epsilon_{eff} = 1.41$) [11]. The microstrip truncated ground plane is located at d_r = 2.7 mm from the driving dipole and acts as a reflector. The antenna is designed to have an input impedance of 50 Ω and is connected to a microstrip line with W_s=1.2 mm (Z_o = 50 Ω). The balun between the microstrip feed and the balanced dipole feed is built using the top and bottom-sides of the Teflon substrate. The driving dipole is fed by a parallel-plate transmission line of width W_f = 0.4 mm and impedance Z_f = 130 Ω, and this transmission line becomes a microstrip feed line of length L_1 = 1.5 mm and impedance Z_1 = 93 Ω followed by another microstrip section of length L_2 = 2.6 mm and impedance Z_2 = 56 Ω to arrive to the 50 Ω microstrip feed. The driver dipole is built on both sides of the substrate and allows a wideband balun feed from the single-ended

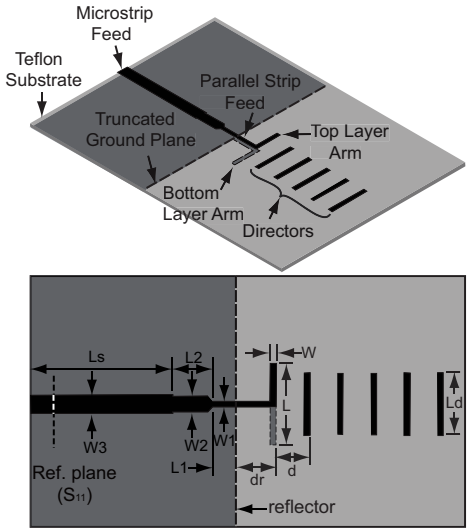

Figure 3.1: Microstrip-fed Yagi-Uda antenna geometry: L=5.4, L_d=4.1, L_1=1.5, L_2=2.6, L_s=20, W=0.4, W_1=0.4, W_2=1.0, W_3=1.2, d=2.4, d_r=2.7 and ground plane width = 29 (all dimensions are in mm).

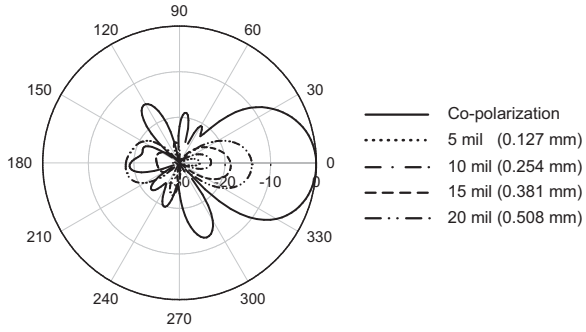

Figure 3.2: Simulated co- and cross-polarization of the microstrip-fed Yagi-Uda antenna at 24 GHz for different substrate thickness.

Table 3.1: Simulated cross-polarization level vs. substrate thickness for the microstrip-fed Yagi-Uda antenna.

Substrate Thickness (mil/mm)	X-pol Level (dB)
5 / 0.127	-25.6
10 / 0.254	-23.0
15 / 0.381	-18.8
20 / 0.508	-14.1

microstrip line to the differential dipole. However, it also results in an increase in the cross-polarization level as shown in 3.2 and Table 3.1. The cross-polarization simulations

were done using HFSS and the antenna dimensions were modified so that the driving dipole of the Yagi-Uda antenna resonates at the same frequency for each case. It is clear that a substrate thickness of 15 mils or less should be chosen for low cross-polarization levels.

3.1.2 Impedance and Pattern Measurements

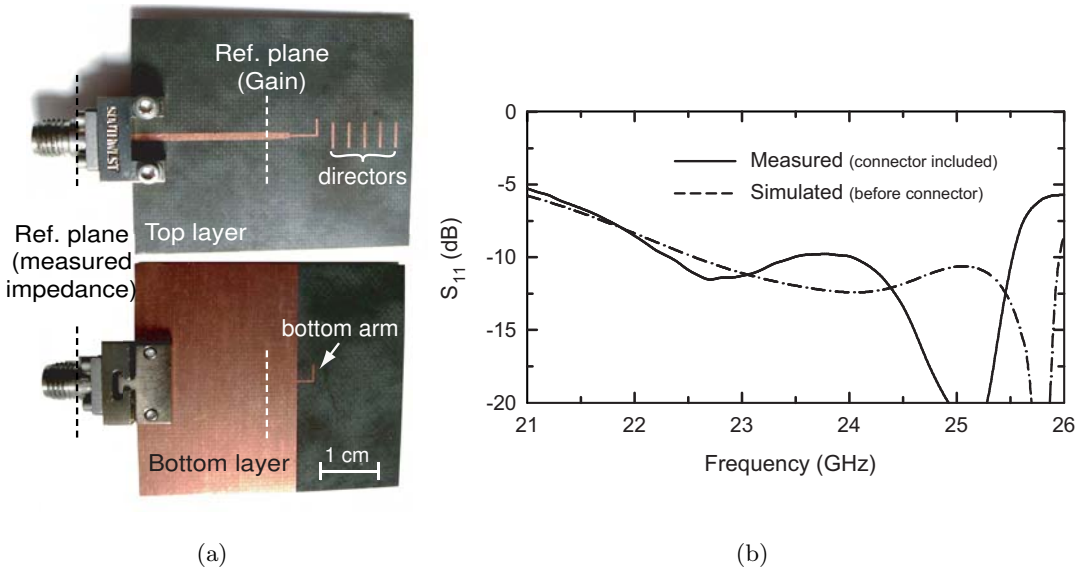

Figure 3.3: (a) Fabricated microstrip-fed Yagi-Uda antenna, ground plane width is 29 mm and microstip line length is 20 mm, (b) measured and simulated S_{11}.

The input impedance of the microstrip-fed Yagi-Uda antenna is measured using a microstrip to coaxial line transition (Fig. 3.3(a)), and shows a good agreement with HFSS simulations with measured S_{11} < -9 dB (simulated S_{11} <-10 dB) from 22.1 to 25.5 GHz (Fig. 3.3(b)). The microstrip to coaxial transition was not included in the simulations. We believe that the slight difference between the measured and simulated S_{11} is due to the effect of this transition.

The radiation patterns were measured in the receive mode using a zero-bias Schottky diode detector (Krytar model 303B) and a lock-in amplifier (Stanford Research Systems, SR830 DSP Lock-in Amplifier). The diode detector was connected to the microstrip line using a high performance Southwest microwave 2.92 mm connector (Fig. 3.3(a)). The RF signal is amplitude modulated with a 1 kHz sine-wave signal and the rectified 1 kHz is measured using the lock-in amplifier. The measured patterns agree well with HFSS simulations and show a front to back ratio of $\sim$ 20 dB and cross-polarization

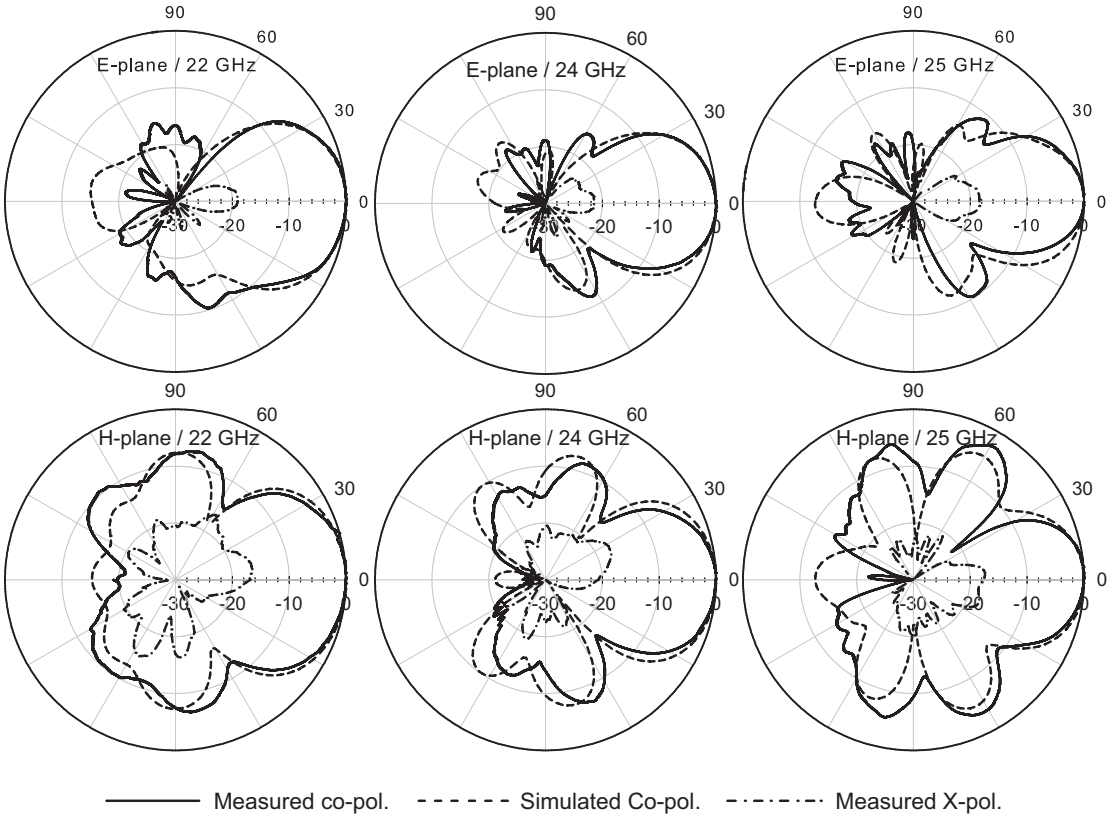

Figure 3.4: Radiation patterns for the microstrip-fed Yagi-Uda antenna.

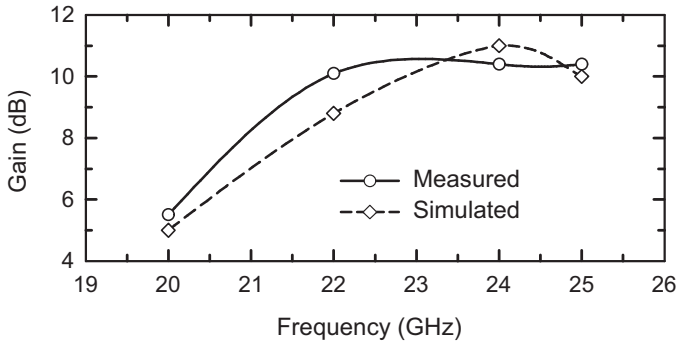

Figure 3.5: Measured and simulated gain of the microstrip-fed Yagi-Uda antenna.

level of $\sim$ -20 dB at 24 GHz (Fig. 3.4). The patterns are quite symmetric at 24 GHz with an E and H-plane 3-dB beamwidths of 44° and 50° , respectively.

3.1.3 Gain Measurements

The absolute gain of the microstrip-fed Yagi-Uda antenna is measured using a standard gain horn antenna. A 2.92 mm Southwest microwave connector is used to minimize the reflection at the connector. The received power is measured using a calibrated Agilent Power Meter (E4417), and the same power meter is used to measure the transmit power. The Yagi-Uda antenna gain is then obtained using the Friis transmission formula. The loss of the microstrip line between the antenna and the Southwest connector is 0.44 dB and is taken out from the gain measurements. The measurements show a gain of $>$ 10 dB from 22-25 GHz and 10.4 dB at 24 GHz (Fig. 3.5). HFSS reported a gain of 10.9 dB with directivity of 11.2 dB at 24 GHz and the difference is mostly due to the impedance mismatch loss. This results in a measured radiation efficiency of $\sim$ 90% within +/-0.5 dB measurement error. The Yagi-Uda antenna gain drops to $\sim$ 1 dB at 26 GHz due to non-optimal phasing of the director elements. This design is therefore optimal for 21-25 GHz applications with a gain $>$ 8 dB, and results in a bandwidth of 17.5%.

3.1.4 Two-Element Array of Microstrip-fed Yagi-Uda Antennas

Two-element arrays of Yagi-Uda antennas with a center to center spacing of 8.75 mm ($0.7\lambda_0$ at 24 GHz) were also built and measured. The first design utilizes a Wilkinson power combiner to combine the signals (Fig 3.6(a)), while the second design uses a matched T-junction (Fig. 3.6(b)) The mutual coupling between two Yagi-Uda antennas, with a center to center spacing of 8.75 mm ($0.7\lambda_0$ at 24 GHz), is measured using the layout shown in Fig. 3.7(a). The measurement agrees with HFSS simulations and shows a mutual coupling of $<$ -16 dB from 20 to 26 GHz (Fig. 3.7(b)). The measured radiation patterns of the two-element arrays show good agreement with simulations as shown in Fig. 3.8(a). The measured 24 GHz E-plane patterns has a 3-dB beamwidth of 30°, while the measured H-plane pattern is similar to the single element pattern and has a 3-dB beamwidth of 46° . The two-element array has nearly the same E-plane pattern as a Yagi-Uda antenna with 10 directors. The measured S_{11} of the two-element arrays is < -8 dB from 22.0 to 26.0 GHz as shown in Fig. 3.8(b). The two-element array gain

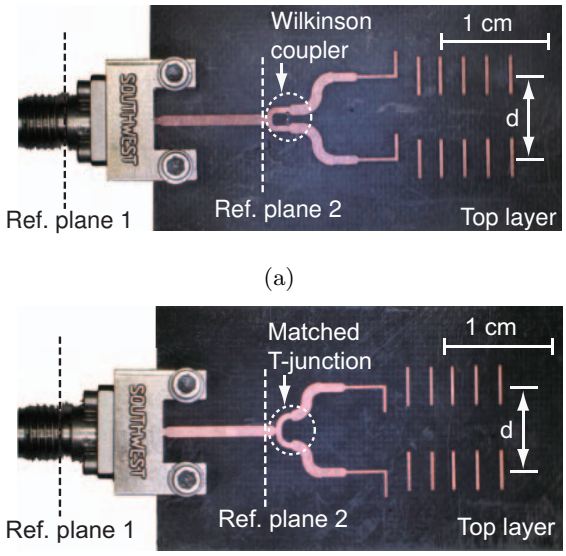

Figure 3.6: Fabricated 2-element arrays of microstrip-fed Yagi-Uda antennas, d = 8.75 mm: with (a) Wilkinson coupler, (b) matched T-junction.

at ref. plane 2 in Fig. 3.6 is measured at 20, 22, 24 and 25 GHz, where the loss between ref. planes 1 and 2 was estimated to be 0.4 dB. The measured gain is $>$ 10 dB from 20 to 25 GHz with a peak value of 12.5 dB and agrees well with simulations (Fig. 3.9)

3.2 Differentially-fed Yagi-Uda Antennas with Folded Dipole Feed

3.2.1 Layout and Input Impedance

Fig. 3.10 shows the layout of the CPS-fed Yagi-Uda antenna with standard and folded dipoles as driving elements. The antenna is built on a 15 mils-thick (0.381 mm) Rogers RT/Duroid 5880 substrate (ϵ_r=2.2). The CPS-feed, driving dipole and five directors are all built on the top side of the substrate whereas the reflector is built on the bottom side of the substrate. The CPS-fed Yagi-Uda antenna can be connected directly to a fully differential RFIC chip (Fig. 3.10). The initial dimensions of the antenna were obtained from tables for maximum directivity in air [49], and then scaled to compensate for the Teflon substrate. The effective dielectric constant is ϵ_{eff} = 1.41 and is calculated using the ratio of the dipole quasi-static capacitance in the presence of the substrate (ϵ_r=2.2) and in air (ϵ_r=1) [11]. The entire design is then optimized using Ansoft-HFSS.

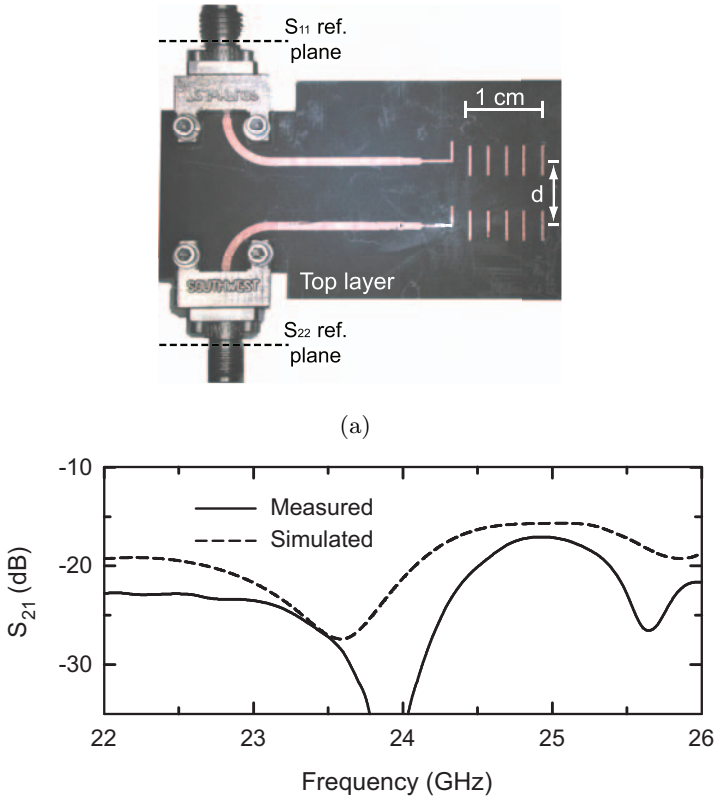

Figure 3.7: ((a) Fabricated two microstrip-fed Yagi-Uda antennas, d = 8.75 mm ($0.7\lambda_0$ at 24 GHz), (b) measured and simulated S_{21}.

Fig. 3.11 presents the HFSS simulated input impedance at Ref. plane 1 of the 7-element Yagi-Uda antenna with a standard dipole and a folded dipole as the driving elements. The simulated input impedance of the CPS-fed Yagi-Uda antenna with a standard dipole at Ref. plane 1 is $\sim$ 18 Ω at 24 GHz and is matched to 18 Ω over a narrow bandwidth (23.6 to 24.3 GHz). However, the CPS-fed Yagi-Uda antenna with a folded dipole shows a simulated input impedance of $\sim$ 153 Ω at 24 GHz and can be matched to 150 Ω with S_{11} < -10 dB from 21.5 to 25.0 GHz (Fig. 3.11(b)). This is compatible with CPS lines on $\epsilon_r = 2.2$ since their characteristic impedance is 100-200 Ω for most dimensions. For these reasons, the folded dipole design was selected for mm-wave implementation.

3.2.2 Measured Radiation Patterns

The radiation patterns of the folded dipole Yagi-Uda antenna are measured in the receive mode using a planar low barrier Silicon Schottky diode detector (Metelics

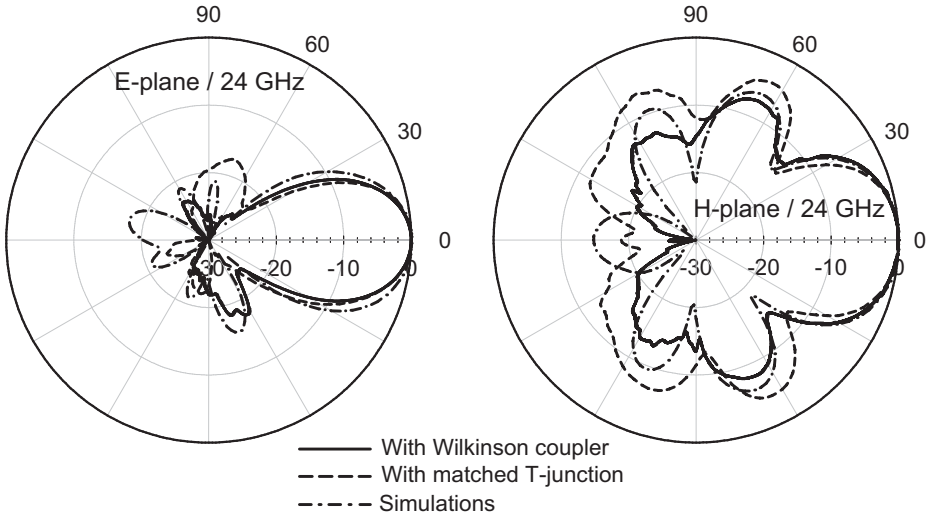

(a)

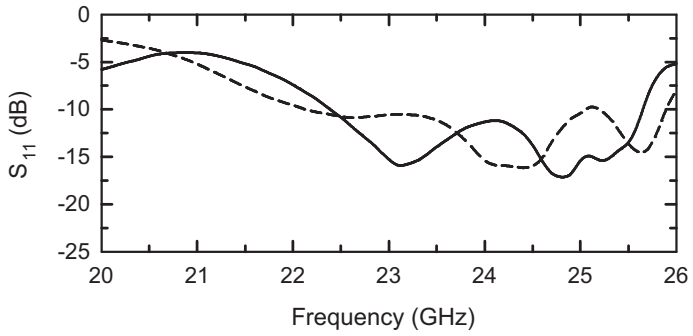

(b)

Figure 3.8: (a) Radiation patterns of the two-element arrays, (b) measured S_{11}.

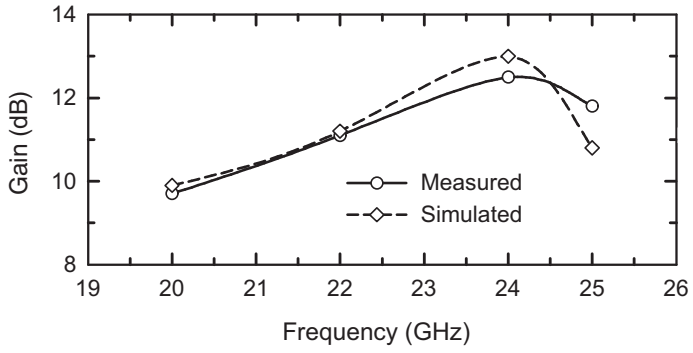

Figure 3.9: Measured and simulated gain of the two element array of the microstrip-fed Yagi-Uda antennas (with Wilkinson coupler) at Ref. plane 2.

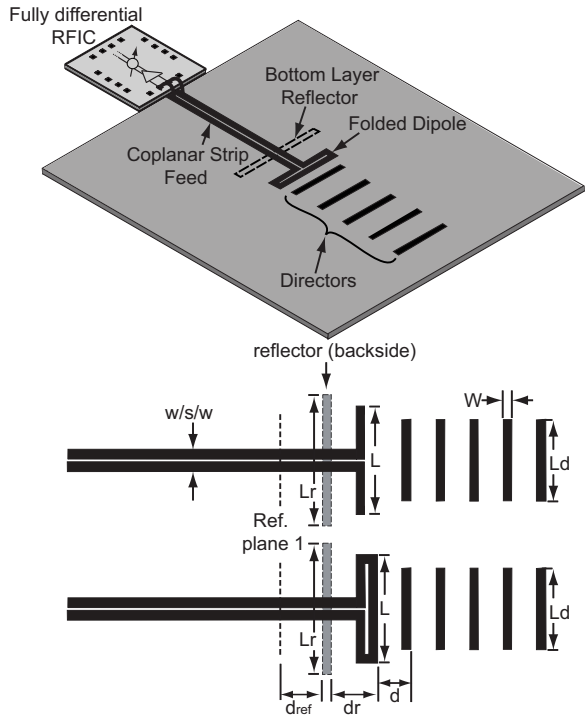

Figure 3.10: CPS-fed Yagi-Uda antenna geometry with regular and with folded dipole feed: L_r = 5.8, L = 4.9, L_d = 3.6, d_{ref} = 4, d_r = 2.1, d = 1.2, W = 0.4, w = 0.4, s = 0.15 (all dimensions are in mm). The CPS line impedance is ∼150 Ω.

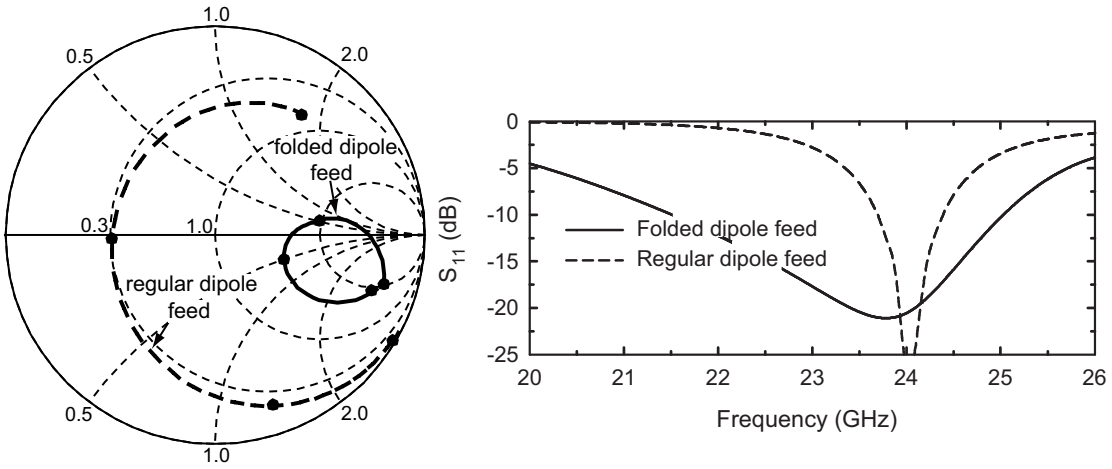

(a) (b)

Figure 3.11: HFSS simulated input impedance of the 7-element CPS-fed Yagi-Uda antenna: (a) on Smith chart for standard and folded dipole driver from 20 to 26 GHz (2 GHz step), (b) S_{11} for the CPS-fed Yagi-Uda antenna with regular dipole (referenced to to 18 Ω) and with folded dipole (referenced to 150 Ω).

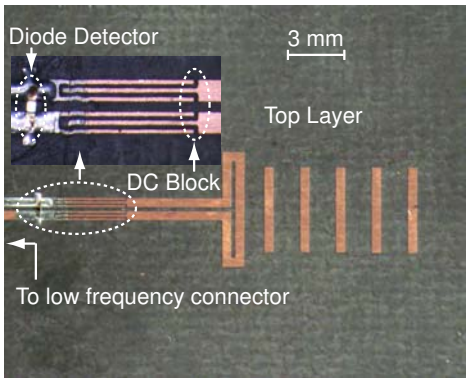

Figure 3.12: Fabricated CPS-fed folded dipole Yagi-Uda antenna with planar schottky diode detector for radiation patterns measurements.

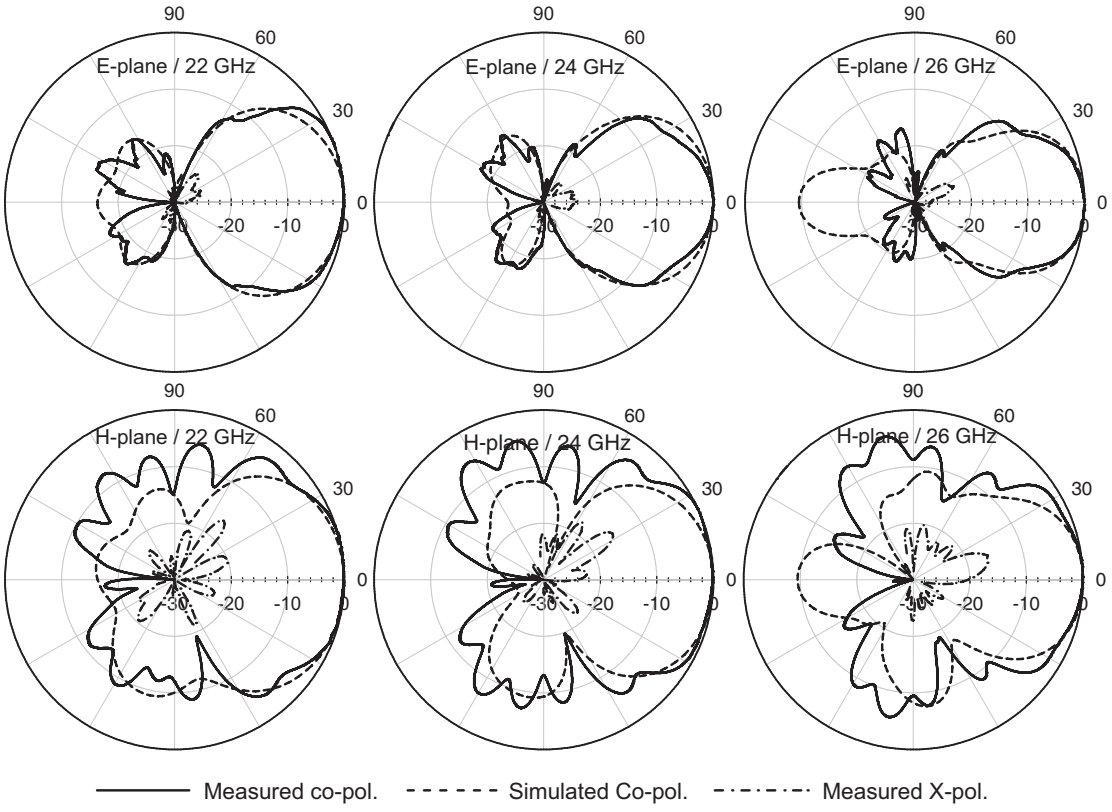

Figure 3.13: Radiation patterns for the CPS-fed Yagi-Uda antenna.

MSS-30-148) and a lock-in amplifier (Stanford Research Systems, SR830 DSP Lock-in Amplifier). The RF signal is amplitude modulated with a 1 kHz sine-wave signal and the rectified 1 kHz is measured using the lock-in amplifier. The diode detector was mounted across the CPS line as shown in Fig. 3.12. The folded dipole introduces a DC-short on the diode detector terminals in the CPS line, and therefore, two Dc-block edge coupled transmission lines are used in the CPS line(only one is needed, but two are used for symmetry). The measured patterns are shown in Fig. 3.13 and show good agreement with HFSS simulations. The measured 24 GHz E- and H-plane 3-dB beam-widths are 42° and 70°, respectively. The CPS-fed Yagi-Uda antenna results in very low cross-polarization level in the E-plane (< -22 dB at 22-26 GHz). The ripples in the H-plane patterns are mostly due to RF leakage on the CPS line and the low frequency coaxial connector at the back of the antenna.

3.2.3 Gain Measurements

In order to measure the gain of the CPS-fed Yagi-Uda antenna, a planar 180° rat-race hybrid coupler is used to feed the differential antenna using a microstrip connector (Fig. 3.14(a)). Fig. 3.14(b) shows excellent agreement between the measured and simulated S_{11} with some minor differences due to the effect of the coaxial to microstrip transition (the Southwest 2.92mm connector is not included in the simulation). The simulated HFSS E-plane radiation patterns at 24 GHz with different distances between the ground plane edge and the antenna reflector are shown in Fig.3.15. It is clear that the ground plane edge has very little effect on the radiation pattern. The absolute gain of the CPS-fed Yagi-Uda antenna is measured with a network analyzer (Agilent PNA network analyzer E8361A) using the gain transfer method. Two identical standard gain (horn) antennas (Dorado GH-42-20) are first connected to the two ports of the network analyzer and S_{21} is measured. The gain of the standard gain horn antennas is then calculated from the measured S_{21} using the Friis transmission formula. The measured gain of the horn antenna is 19.4 +/- 0.7 dB from 20 to 28 GHz and is consistent with the nominal value from the manufacturer.

One horn antenna is then replaced by the CPS-fed Yagi-Uda antenna (with the rat-race coupler) shown in Fig. 3.14(a) and the gain of the CPS-fed Yagi-Uda antenna is then obtained from the difference in the measured S_{21} in both cases. The measured gain of the CPS-fed Yagi-Uda antenna at Ref. plane 2 in Fig. 3.14(a) is shown in Fig. 3.16.

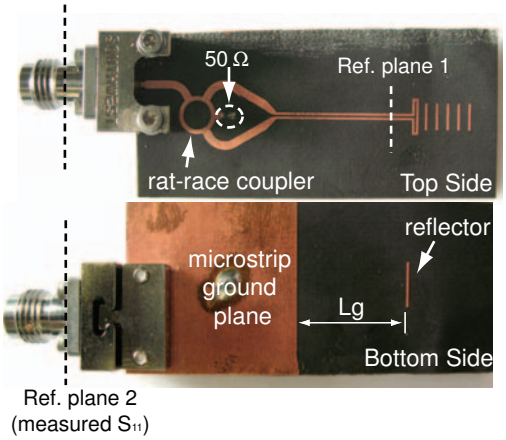

(a)

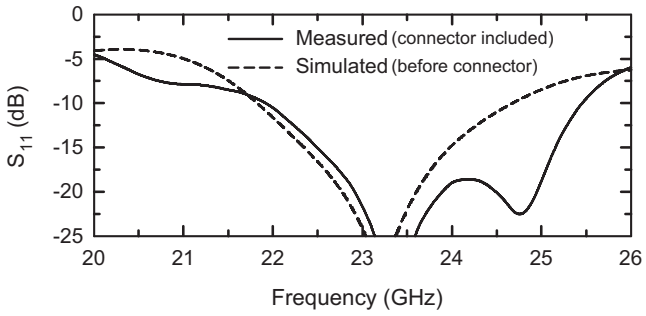

(b)

Figure 3.14: (a) Fabricated CPS-fed Yagi-Uda antenna with rat-race coupler, $L_g = 14$ mm, (b) measured and simulated S_{11} (referenced to 50 Ω).

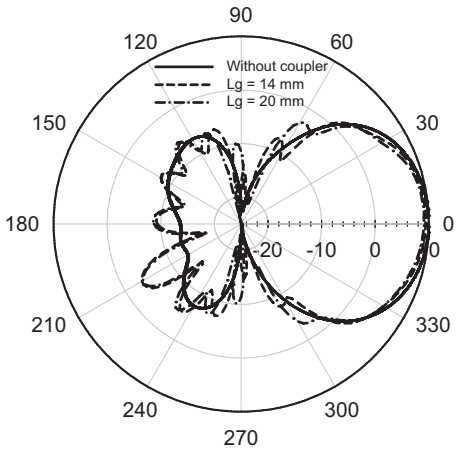

Figure 3.15: HFSS simulated E-plane radiation patterns at 24 GHz of the CPS-fed Yagi-Uda with rate race coupler for different distances between the ground plane edge and the antenna reflector (L_g).

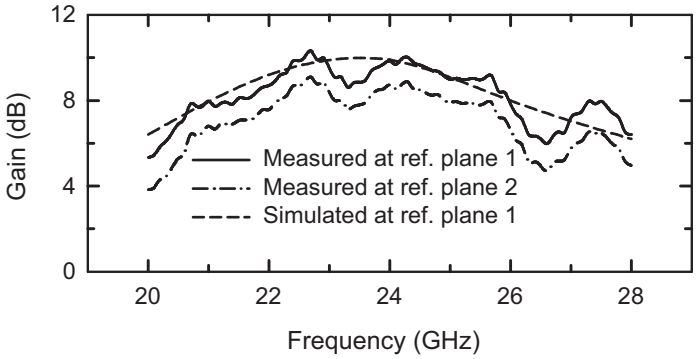

Figure 3.16: Measured and simulated gain of the CPS-fed Yagi-Uda antenna. The gain measurements at Ref. plane 1 are de-embedded from the Ref. plane 2 measurements and the rat-race coupler/CPS transition loss.

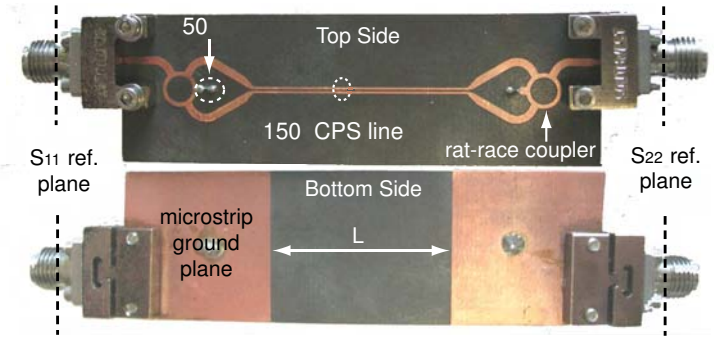

(a)

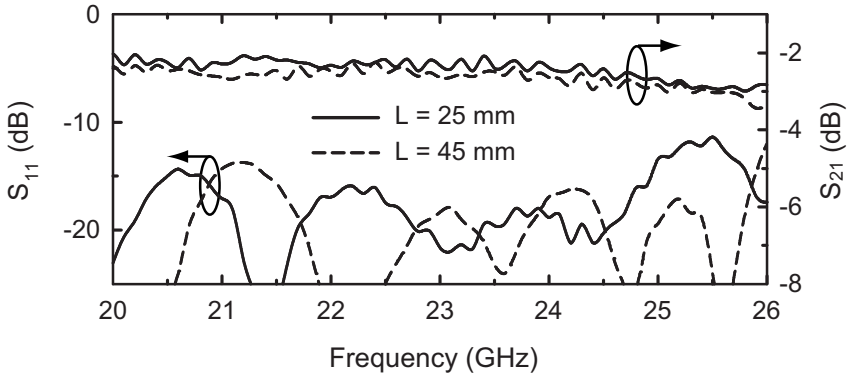

(b)

Figure 3.17: (a) Fabricated back-to-back rat-race coupler/CPS transition, (b) measured S_{11} and S_{21} for two different CPS lengths.

The antenna impedance mismatch loss is included in the measured gain. The loss of the 2.4 mm connector, the 180° hybrid coupler and the CPS line between Ref. planes 1 and 2 in Fig. 3.14(a) was then measured separately. Two back-to-back designs with different lengths of CPS line are built and the measured S_{11} and S_{21} of these back-to-back designs are shown (Fig. 3.17(b)). The measured S_{21} of the back-to-back design with 25 mm of CPS line is $\sim$ -2.4 dB at 24 GHz. This results in a total loss of $\sim$ 1.2 dB between Ref. planes 1 and 2 (Ansoft-HFSS predicted 0.8 dB loss). The measured S_{21} of the back-to-back design with 45 mm CPS line is $\sim$ -2.6 dB at 24 GHz, which means that the CPS line has a loss of $\sim$ 0.1 dB/cm (HFSS predicted a loss of 0.07 dB/cm). The measured gain agrees very well with simulated gain, but with some ripples due to the scattering effects from the measurement setup. The measured gain is $>$ 8 dB from 21.5 to 25.9 GHz with a measured peak gain of 9.8 dB at 24 GHz. HFSS reports a directivity of 10.3 dB with a gain of 9.9 dB at 24 GHz, and this corresponds to a radiation efficiency $>$ 90%, which is collaborated by our experiment (within measurement error).

3.2.4 Conclusion

This chapter presented millimeter-wave Yagi-Uda antennas with applications as single element radiators or for switched-beam systems with medium gain (9-13 dB). It is seen that the differential design results in much lower cross-polarization levels than the single ended design and can be matched to a coplanar-stripline impedance of 150 Ω. The planar Yagi-Uda antenna can be arrayed for additional gain (+ 3dB) and with low mutual coupling between the elements. Both single-ended and differential designs result in relatively wideband operation (22-26 GHz), low cross-polarization levels, and high radiation efficiency. These antennas can be scaled to 60 GHz, 77 GHz or 94 GHz for automotive radars and high data-rate communication systems. The chapter presents for the first time a fully differential CPS-fed Yagi-Uda antenna which uses a folded dipole feed to increase the antenna impedance and enhance its impedance matching bandwidth. This antenna is ideally suited for differential RFIC connections.

Chapter 3 is mostly a reprint of the material as it appears in IEEE Transactions on Antennas and Propagation, 2009 and 2010. Ramadan A. Alhalabi; Gabriel M. Rebeiz. The dissertation author was the primary author of this material.

Chapter 4

Self-Shielded Yagi-Uda Antennas for 60 GHz Communications

4.1 Introduction

The 60 GHz frequency band presents many attractive properties for wireless communication systems such as wide bandwidth (5-7 GHz) and high atmospheric absorption which makes it ideal for Gbps short distance communication systems. In the past 2-3 years, the 60 GHz has seen a lot of activity with CMOS and SiGe transceiver chips [50–55]. It is therefore important to develop planar high-gain antennas for these systems which offer high efficiency and are insensitive to their surroundings.

Several antennas and antenna arrays have been demonstrated in the past few years: A 60 GHz aperture-coupled microstrip antenna integrated on LTCC multilayer technology and with 7.6 dB gain is presented in [56]. A 60 GHz uniplanar-compact electromagnetic band-gap structure on LTCC is presented in [57] and used with aperture-coupled microstrip antenna to improve its gain and reduce mutual coupling. Also, an 8x8 array of patch antennas on a Teflon substrate with ∼20 dB gain and 3 GHz bandwidth was presented in [58], and high gain active microstrip antenna arrays on alumina substrates were demonstrated in [59]. Kim et al. presented a 60 GHz CPW-fed micro-machined post-supported microstrip patch antenna which is compatible with silicon processing [60]. A 60 GHz dipole antenna integrated on 0.13 μm silicon-on-insulator with a gain of 4.5 dB and 8 % impedance bandwidth is presented in [61]. The antennas in [56–61] are all of the broadside type and do not easily lead to a switched-beam

system. On the other hand, endfire antennas such as endfire dipoles [62], Yagi-Uda antennas [63–65] or endfire horn antennas [22] can result in high gain and are compatible with a 2- or 4-element switched-beam array.

This chapter presents a microstrip-fed 60 GHz 7-element endfire Yagi-Uda antenna. The antenna is built on a Teflon substrate and its performance is characterized first in free space and then in the presence of two metal sheets placed above and below the antenna and with different spacings. The antenna is also characterized inside a metal box (top, bottom and two side-walls) with different heights. The metal shields isolate the Yagi-Uda antenna from its surroundings and allow its insertion in complicated platforms with batteries and dense printed circuit boards (PCBs) available in laptops and mobile phones. A four-element switched-beam Yagi-Uda array is also presented with top and bottom ground planes. This array allows for 180° angular coverage and with excellent performance.

4.2 Single Element in Free Space

4.2.1 Geometry

Fig. 4.1 presents the geometry of the 7-element microstrip-fed Yagi-Uda antenna. The antenna is built on a Rogers RT/Duroid 5880 substrate ($\epsilon_r = 2.2$) with a thickness of 10 mils (0.254 mm). The antenna was first designed at 24 GHz on a 15 mils (0.381 mm) Teflon substrate [64] and is scaled here to 60 GHz. The Yagi-Uda antenna utilizes 5 directors printed on the top side of the substrate with a spacing of 1.0 mm. The microstrip truncated ground plane is located at $d_r = 1.1$ mm from the driving dipole and acts as a reflector. The driving dipole and the balun between the microstrip feed and the dipole is built using the top and bottom-sides of the Teflon substrate. The antenna was optimized using Ansoft-HFSS including a short magnetic ground-plane edge (Fig. 4.1).

4.2.2 Input Impedance and Radiation Patterns

The input impedance of the Yagi-Uda antenna is measured with a 67 GHz network analyzer (Agilent E8361A) using a 2.4 mm Southwest microwave connector (Fig. 4.2(a)). The 2.4 mm connector introduces some mismatch to the feeding microstrip line, and the mismatch effects were taken out using the time domain gating. The 7-element

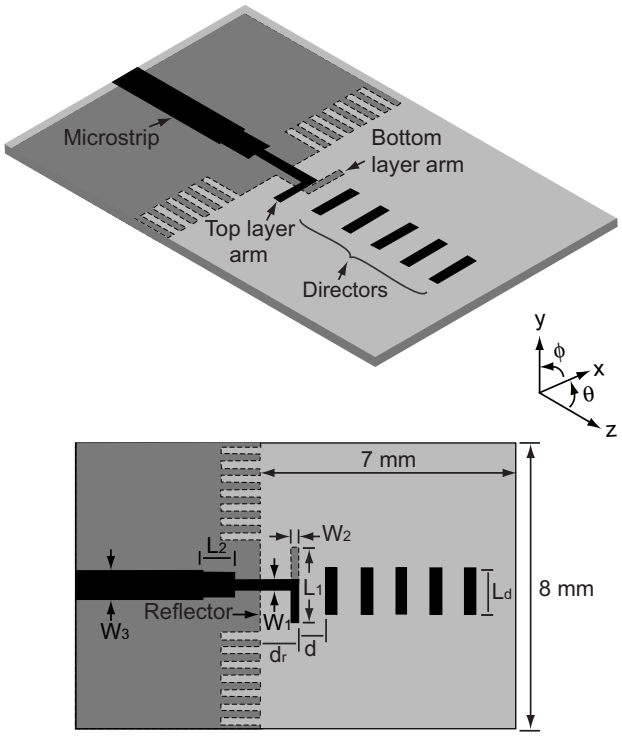

Figure 4.1: 60 GHz microstrip-fed Yagi-Uda antenna geometry: d = 1.1, d_r = 1.1, L_1 = 2.1, L_2 = 0.9, L_d = 1.3, W_1 = 0.3, W_2 = 0.2, W_3 = 0.8 (all dimensions are in mm).

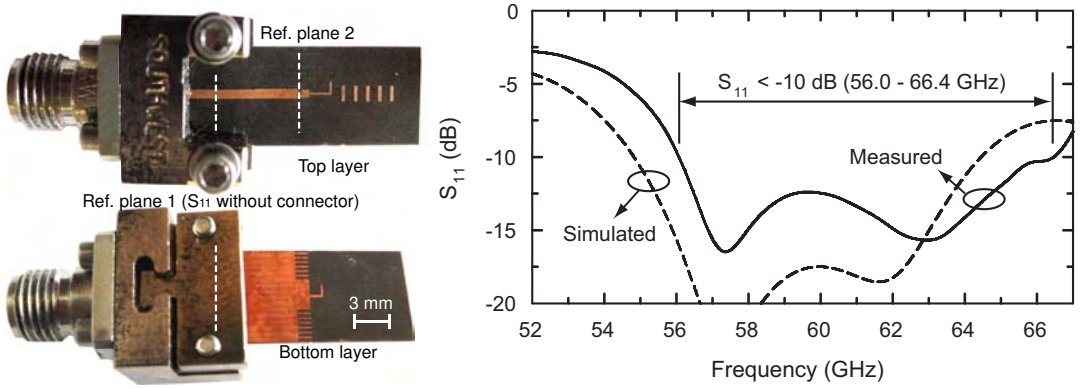

(a) (b)

Figure 4.2: (a) Fabricated 60 GHz Yagi-Uda antenna, (b) measured and simulated S_{11}. Time domain gating is used to remove the connector effects.

Yagi-Uda antenna results in a measured S_{11} < -10 dB from 56.0 - 66.4 GHz and agrees well with simulations (Fig. 4.2(b)). The radiation patterns of the Yag-Uda antenna are measured in the receive mode using a 40-60 GHz diode detector and a lock-in amplifier (Stanford Research Systems, SR830). The RF signal is amplitude modulated with a 1 kHz sine-wave signal and the rectified signal is measured using the lock-in amplifier. A thin absorber is used over the connector and the diode detector to reduce its scattering effects. The measured patterns agree well with HFSS simulations as shown in Fig. 4.3. The cross-polarization is mainly due to the vertical fields between the dipole arms placed on both sides of the substrate [62], [64], and is < -14 dB at most frequencies. The antenna has a measured 3-dB beamwidth of 54° and 58° at 60 GHz in the E- and H-plane respectively; and a simulated directivity of 11.0 dB at 60 GHz.

4.2.3 Gain

The absolute gain of the Yagi-Uda antenna is measured using a network analyzer (Agilent PNA network analyzer E8361A) and the gain transfer method. Two identical standard gain (horn) antennas are first connected to the two ports of the network analyzer and characterized. One horn antenna is then replaced by the antenna under test and its gain is obtained from the difference in the measured S_{21} for both cases. The measured gain of the Yagi-Uda antenna is shown in Fig. 4.4. The losses of the microstrip line (∼0.8 dB/cm) and the 2.4 mm connector (∼0.9 dB) at 60 GHz were measured separately and taken out, and this places the reference plane at plane 2 (Fig. 4.2(a)). The antenna impedance mismatch loss is included in the measured gain. The ripples in the measured gain are due to scattering effects from the connector which was not covered by absorbers during the gain measurements. The measured gain of the Yagi-Uda antenna is > 9.5 dB from 58 - 63 GHz (10.8 dB at 60 GHz) and agrees well with simulations. The antenna efficiency, defined as the measured gain over the simulated directivity, is 95% at 60 GHz. This is reasonable since the gain is referred to Ref. plane 2 (see Fig. 4.2(a)) and does not include any microstrip line loss.

4.3 Single Element with Self Shielding

The high-gain Yagi-Uda antenna will be embedded inside a portable device such as a laptop or a mobile phone where it will be surrounded by unknown metal layers and other electronic components. As a result, it is important to design an antenna which is

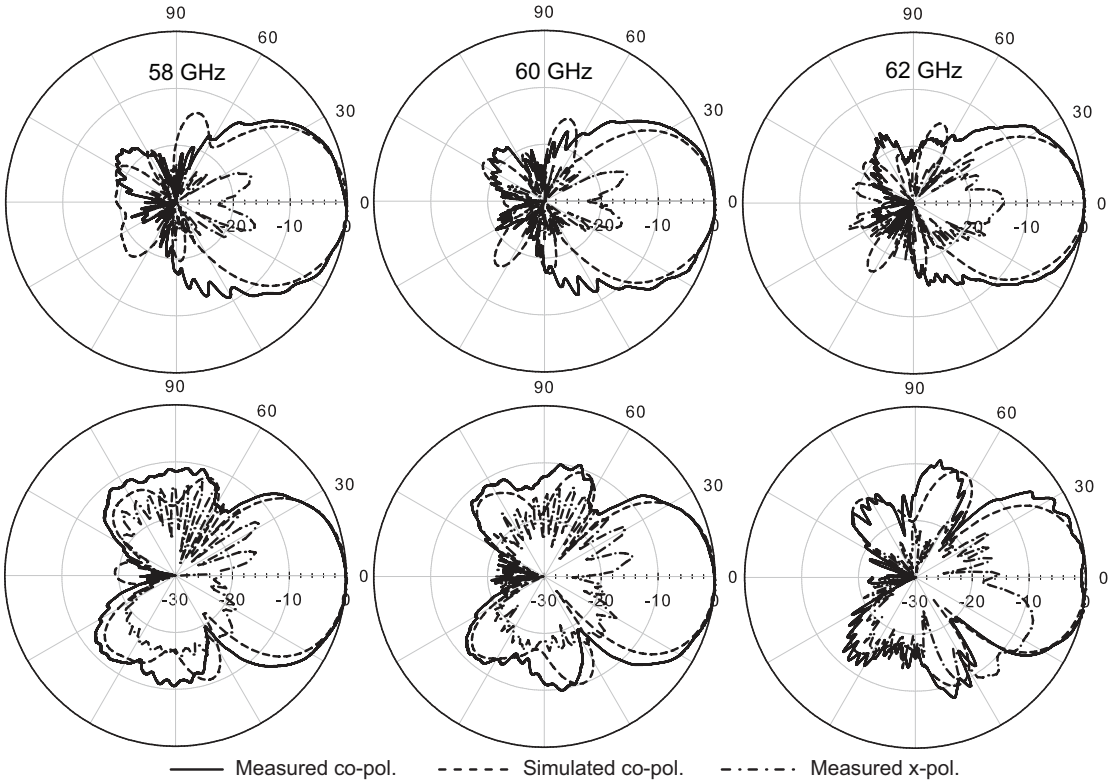

Figure 4.3: Radiation patterns for the microstrip-fed Yagi-Uda antenna: E-plane (top), H-plane (bottom).

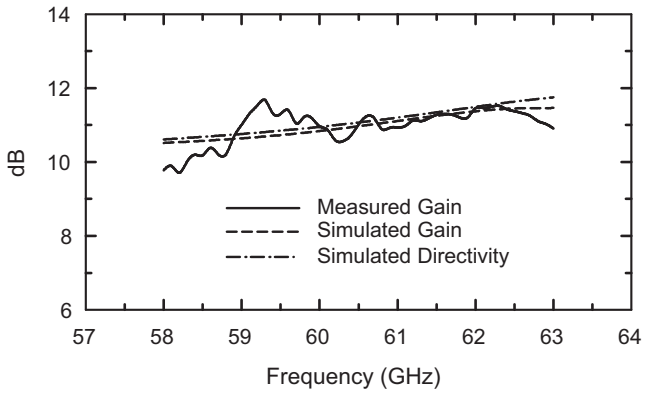

Figure 4.4: Measured and simulated gain of the 60 GHz Yagi-Uda antenna.

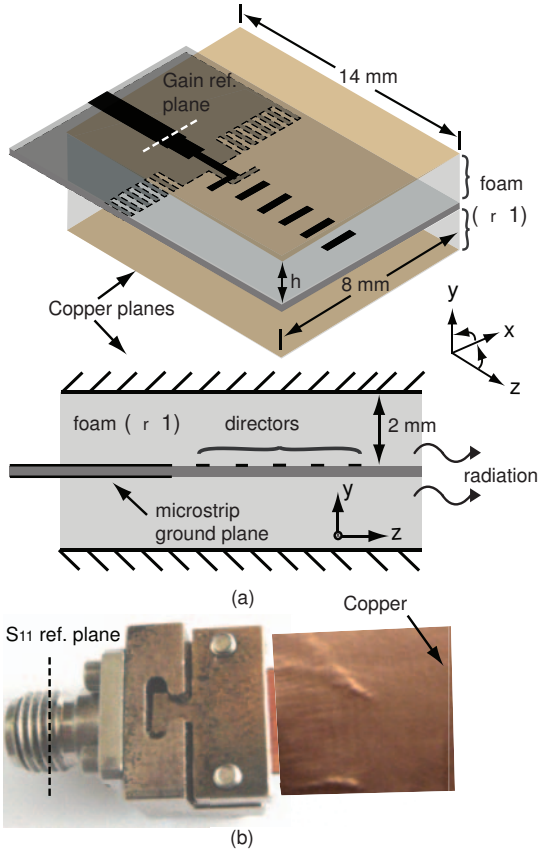

Figure 4.5: 60 GHz Yagi-Uda antenna sandwiched between two foam pieces with thickness of (h) mm and with copper sheets on the top and bottom sides. Fig. 5(a) cross-section is to scale with h= 2 mm.

self-shielded and is not affected by its surroundings. One way to achieve this is to use two metal shielding planes above and below the Yagi-Uda antenna. These metal planes are not connected to the microstrip ground plane and are separated using thin foam pieces by a distance h from the Teflon substrate (Fig. 4.5). The Yagi-Uda antenna operation is based on the mutual coupling between the antenna elements (driving dipole, reflector and directors), and it is necessary that the metal ground planes do not disturb the mutual coupling between the antenna elements. Fig. 4.6 presents the HFSS simulated magnitude and phase of the mutual impedance (Z_{21}) between two elements with a length L_d =1.3 mm and center-to-center spacing of 1 mm (see Fig. 4.1). It can be seen that the phase variations are $< 20°$ at 56-63 GHz for h 2 mm. However, for h $\leq$ 1 mm, the coupling between the two elements changes considerably, and the Z_{21} phase at h = 1 mm is $> 20°$. As a result, the metal shielding planes should be at least 2 mm far

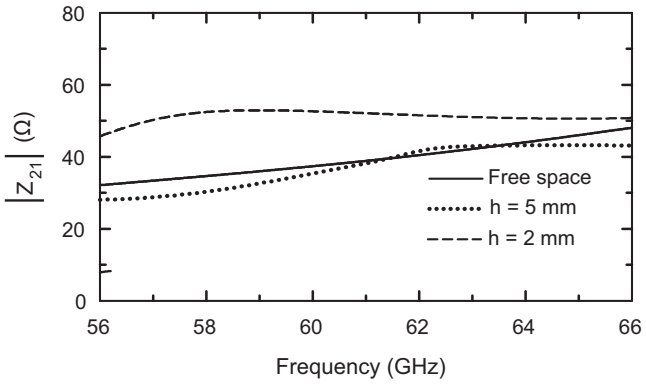

(a)

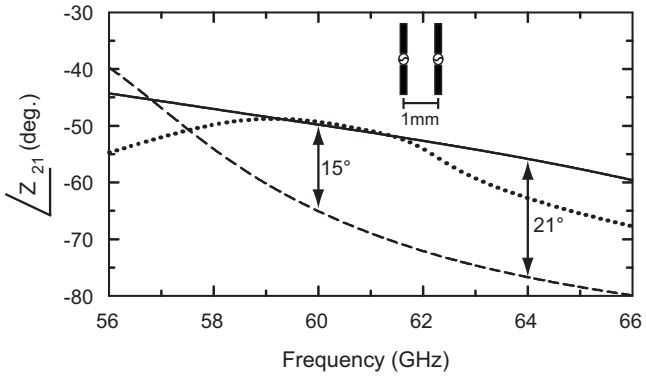

(b)

Figure 4.6: HFSS simulated mutual impedance (Z_{21}) in free space and with top and bottom metal planes with different h, L_d = 1.3 mm, center-to-center spacing = 1 mm: (a) magnitude, (b) phase.

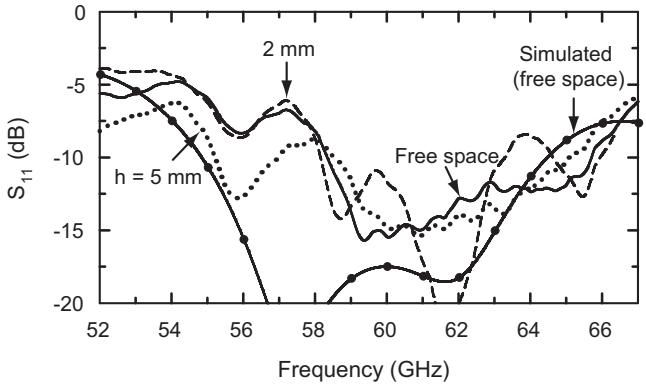

Figure 4.7: Measured S_{11} of the 60 GHz Yagi-Uda antenna for different spacing from the copper sheets (h) (measurements include connector effects).

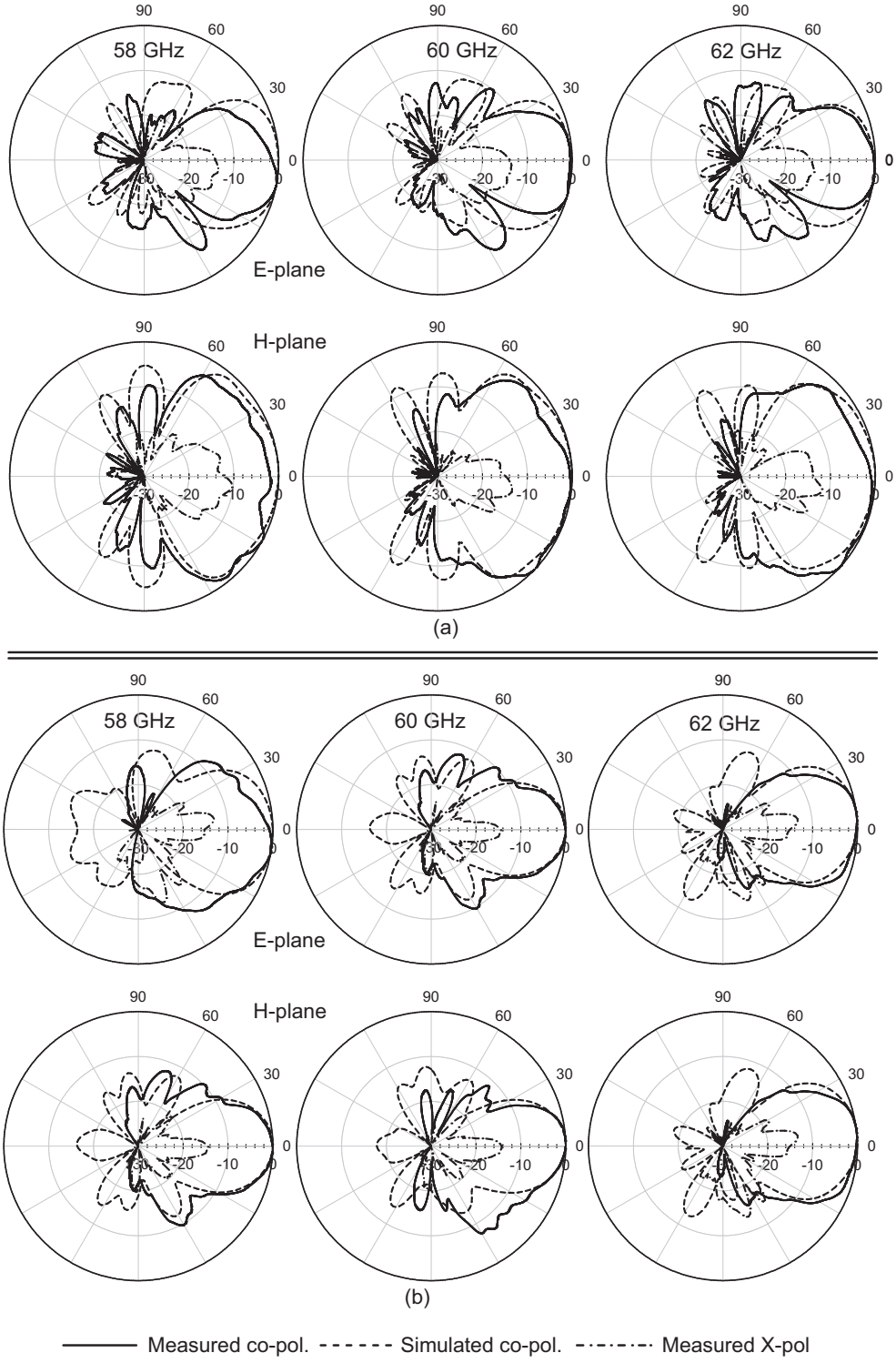

Figure 4.8: Measured and simulated radiation patterns with top and bottom metal planes for: (a) h = 2 mm and (b) h = 5 mm.

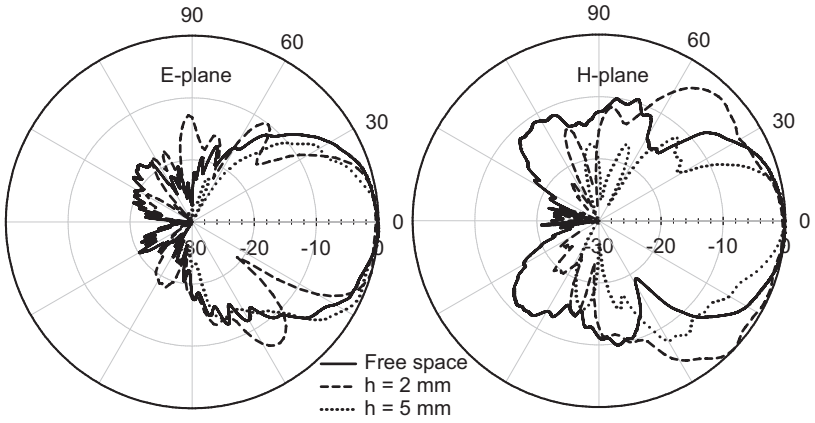

Figure 4.9: Measured E-plane (left) and H-plane (right) radiation patterns at 60 GHz in free space and with top and bottom copper shielding planes for h = 2 and 5 mm.

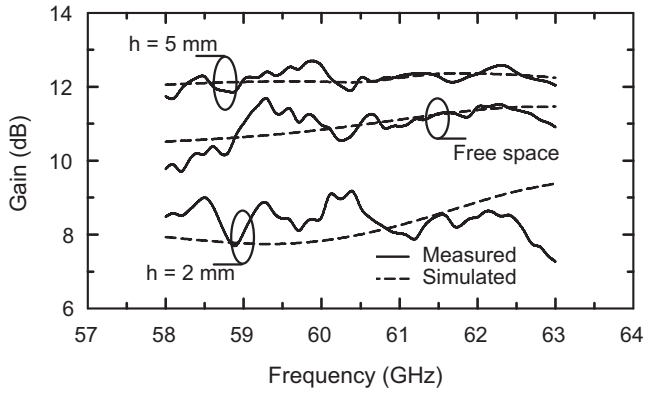

(a)

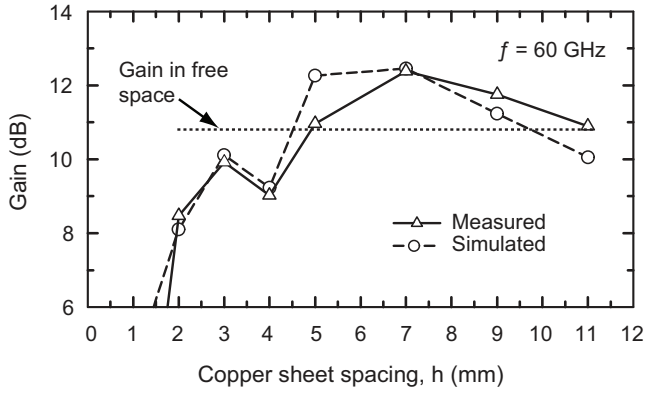

(b)

Figure 4.10: Measured: (a) gain vs. frequency for different h, (b) gain vs. h at 60 GHz of the Yagi-Uda antenna with top and bottom copper sheets.

from the Yagi-Uda antenna; otherwise one has to redesign the antenna for a specific ground-shielding height. The measured S_{11} of the Yagi-Uda antenna embedded between two copper planes is shown in Fig. 4.7 for different h spacings. The measurements show that copper planes have negligible effect on the measured S_{11} as long as h > 2 mm. Measurements were also done on h = 1 mm and resulted in a poor match ($S_{11} \cong$ -4 dB). The measured and simulated radiation patterns for h = 2 mm and 5 mm are presented in Fig. 4.8 and agree well with simulations. The cross-polarization remains low in the principal planes (< -12 dB) and is slightly higher than the free space antenna due to a slight coupling to the shielding planes generating a small vertical electric-field component. The Yagi-Uda antenna excites currents on the shielding planes with certain magnitude and phase depending on the distance from the antenna (h). The currents on the top and bottom planes radiate, and the H-plane pattern is a result of the interaction between the current on the Yagi-Uda antenna elements and the currents on the shielding planes. For h = 2 mm, there is a significant amount of RF current on the top and bottom planes which are not in phase with the current on the Yagi-Uda, and the resulting H-

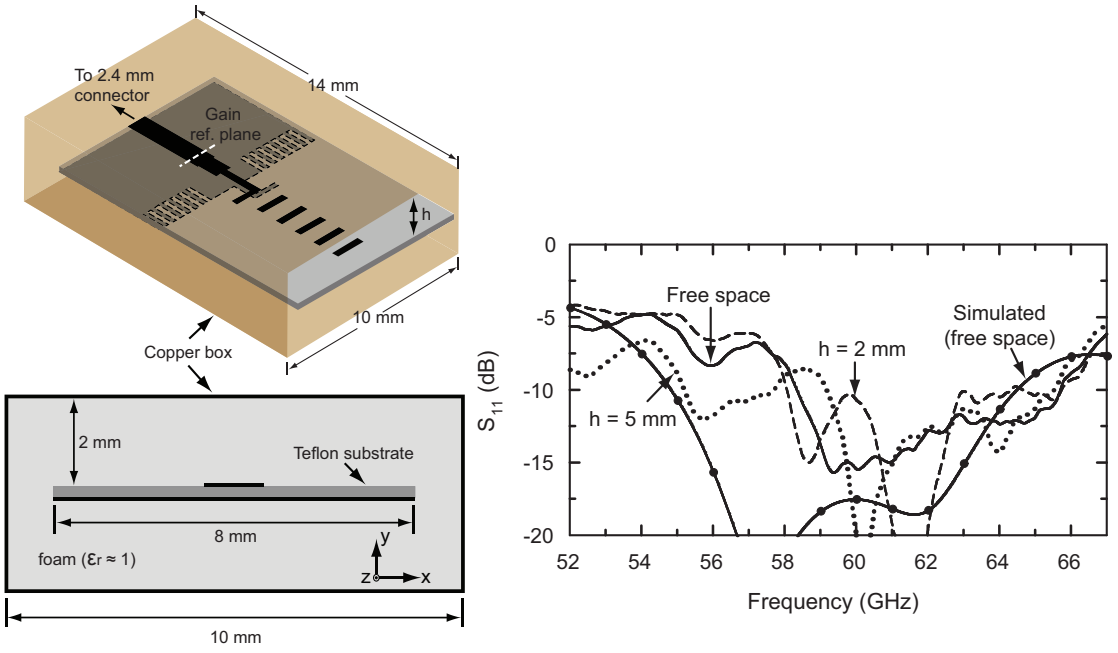

(a) (b)

Figure 4.11: (a) Geometry of the 60 GHz Yagi-Uda antenna sandwiched between two pieces of foam with copper planes on top, bottom and on the sides (b) measured S_{11} for different h values. The measurements include the 2.4 mm Southwest connector. Fig. 4.11(a) front-view is to scale with h = 2 mm.

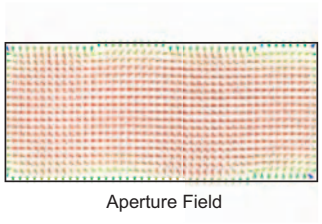

Aperture Field

Waveguide Mode	Power Coupled
TE01	56 %
TM31	12 %
TM21	05 %
TE11	04 %
TE10	03 %

h = 2 mm

(a)

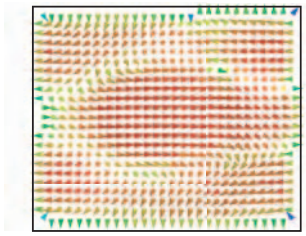

Aperture Field

Waveguide Mode	Power Coupled
TE03	27 %
TE01	24 %
TE21	12 %
TE13	06 %
TM21	05 %
TM13	02 %
TM32	02 %
TM11	02 %

h = 4 mm

(b)

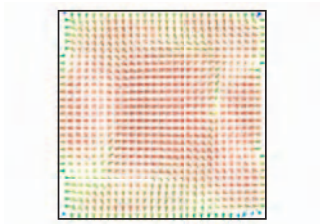

Aperture Field

Waveguide Mode	Power Coupled
TE01	45 %
TE21	17 %
TM23	14 %
TM21	06 %
TE21	02 %

h = 5 mm

(c)

Figure 4.12: HFSS simulated waveguide modes and aperture fields at 60 GHz for: (a) h = 2 mm, (b) h = 4 mm, (c) h = 5 mm.

plane pattern is much wider than the free space case. The E-plane pattern remains approximately the same since the currents on the top and bottom planes affect mostly the H-plane patterns. For h = 5 mm, the excited currents on the top and bottom planes are in phase with the current on the Yagi-Uda antenna, and result in a narrower H-plane pattern and higher antenna gain than the free space case. The measured radiation patterns at 60 GHz in free space and with top and bottom metal planes are compared in Fig. 4.9 for h = 2 mm and 5 mm. The measured gain of the Yagi-Uda antenna vs. frequency for h = 2 mm, 5 mm and in free space are shown in Fig. 4.10(a). Fig. 4.10(b) presents the measured and simulated gain at 60 GHz vs. h, and shows a gain $>$ 10 dB for h $\geq$ 5 mm (λ_0 at 60 GHz). For h $<$ 2 mm, the antenna gain and impedance match are greatly affected due to the change in the mutual coupling parameters between the

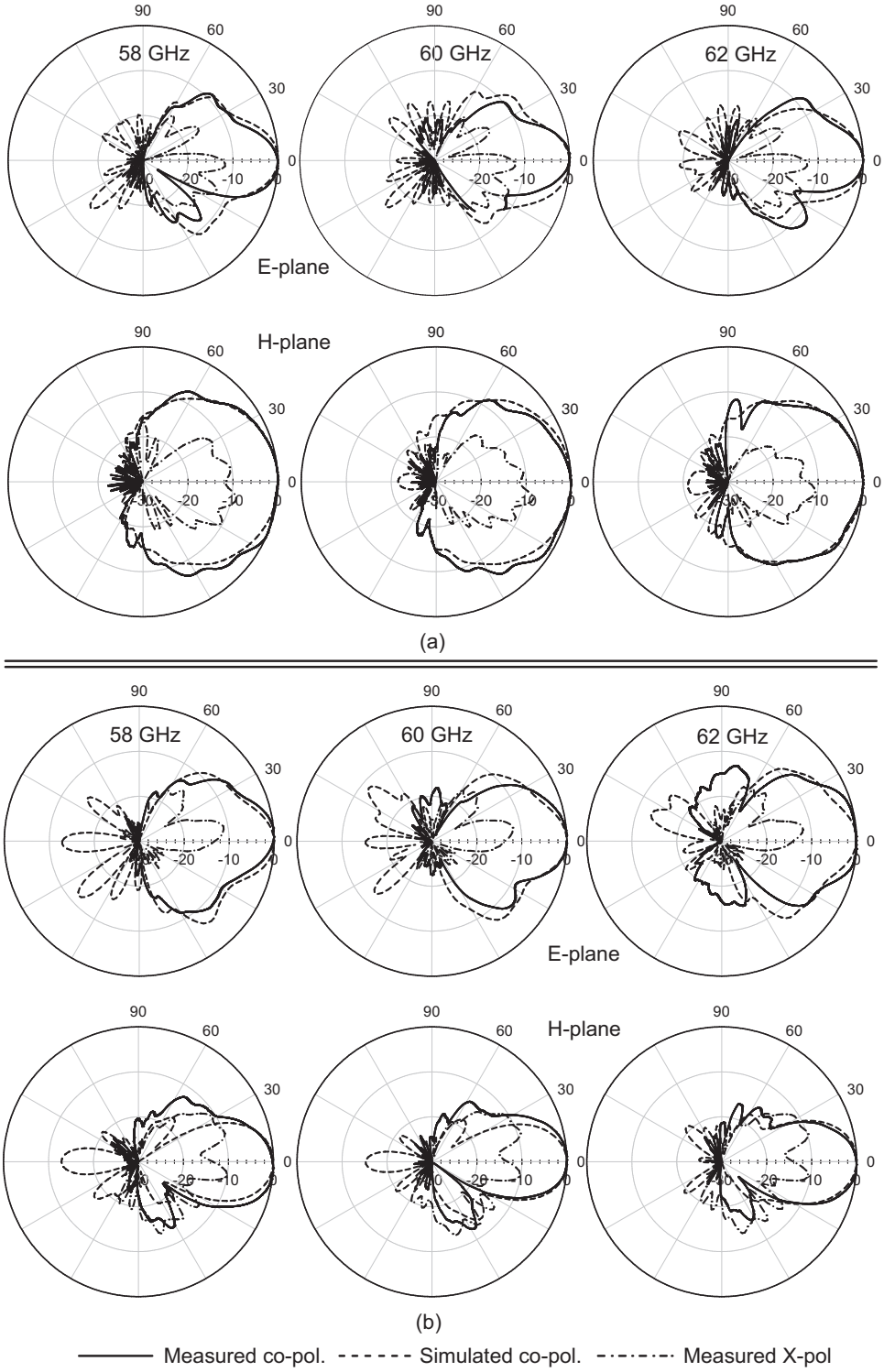

Figure 4.13: Measured and simulated radiation patterns with metal box for: (a) h = 2 mm and (b) h = 5 mm.

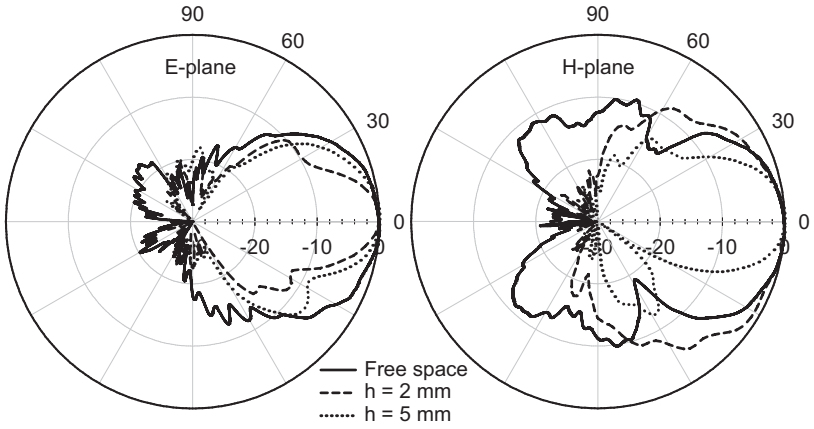

Figure 4.14: Measured E-plane (left) and H-plane (right) radiation patterns at 60 GHz in free space and with box shielding for h = 2 and 5 mm.

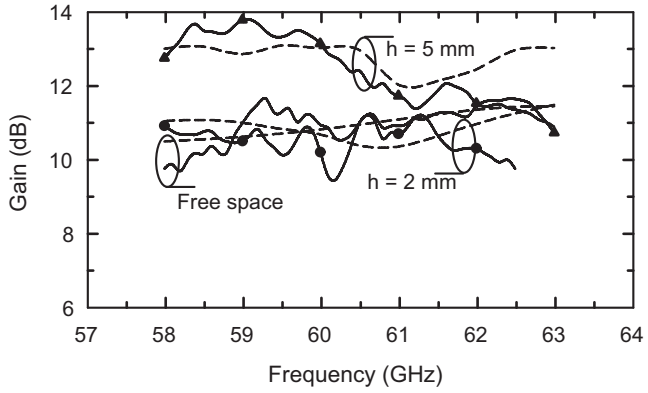

(a)

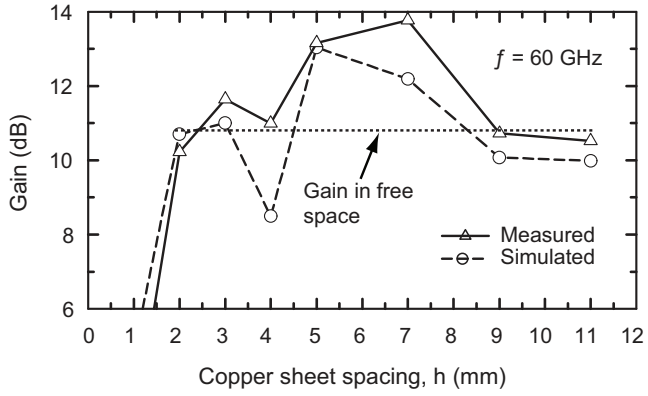

(b)

Figure 4.15: Measured: (a) gain vs. frequency for different h, (b) gain vs. h at 60 GHz of the Yagi-Uda antenna with box shield.

director elements. The design results in an increase in antenna gain (over the free space design) at h = 5-10 mm due to a sharpening of the H-plane. The antenna can also be shielded from the sides by adding copper walls on each side as shown in Fig 4.11(a). The side-walls are kept 1 mm away from the Teflon substrate and do not touch the Teflon substrate or the microstrip ground plane. The total box width is 10 mm, which is $2\lambda_0$ at 60 GHz and therefore can sustain several waveguide modes (TE_{10}, TE_{11}, TE_{20}, TM_{11}, etc.). Also, the box height is at least 4.25 mm (h = 2 mm) and 10.25 mm (h= 5 mm) with a partially grounded substrate, and can sustain orthogonal waveguide modes. In this case, the radiation patterns can be determined by the aperture field distribution, and HFSS analysis for the first 20 waveguide modes indicates that most of the power couples into the TE_{01} mode for h = 2 mm and 5 mm (Fig. 4.12). However, at h = 4 mm, the power is coupled into the TE_{03}, TE_{01} and TE_{21} modes which result in tapering in both the E and H-planes, and thus wider radiation patterns and a lower gain. The measured S_{11} of the Yagi-Uda antenna with shielding box is presented in Fig. 4.11(b)

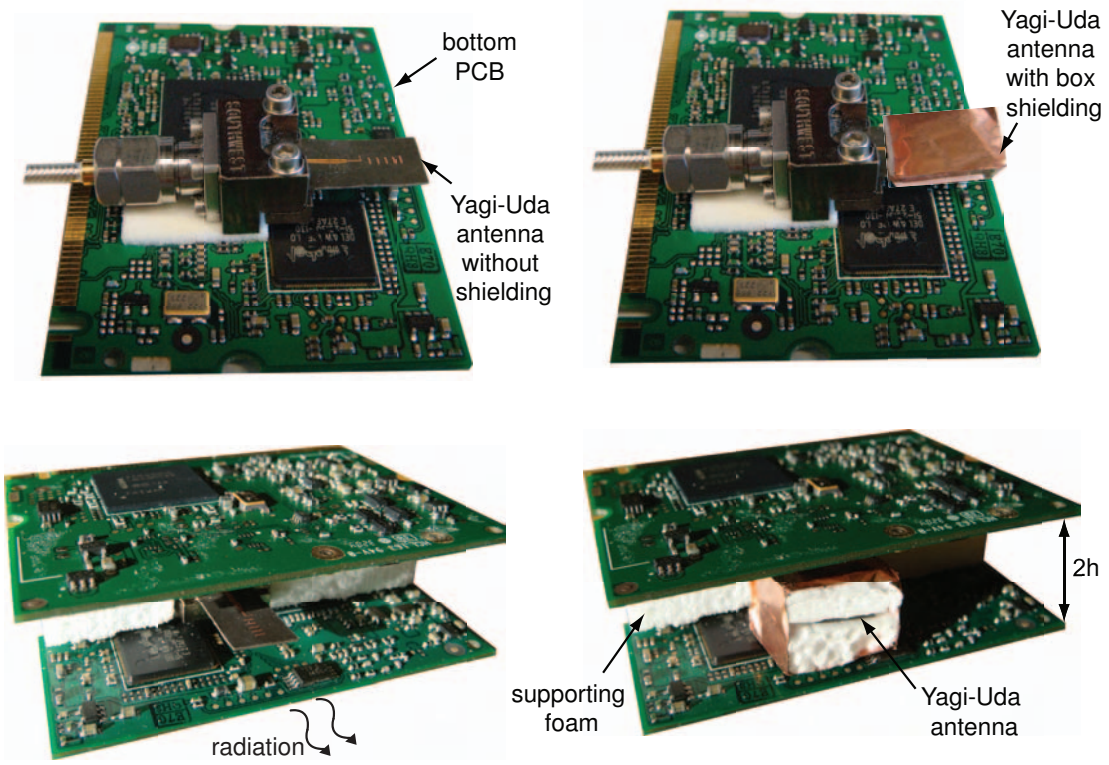

Figure 4.16: Yagi-Uda antenna on a PCB setup: without metal shield (left), with shielded box (right). The PCB size is 6 cm x 4 cm. In the top picture, one PCB is removed for clarity.

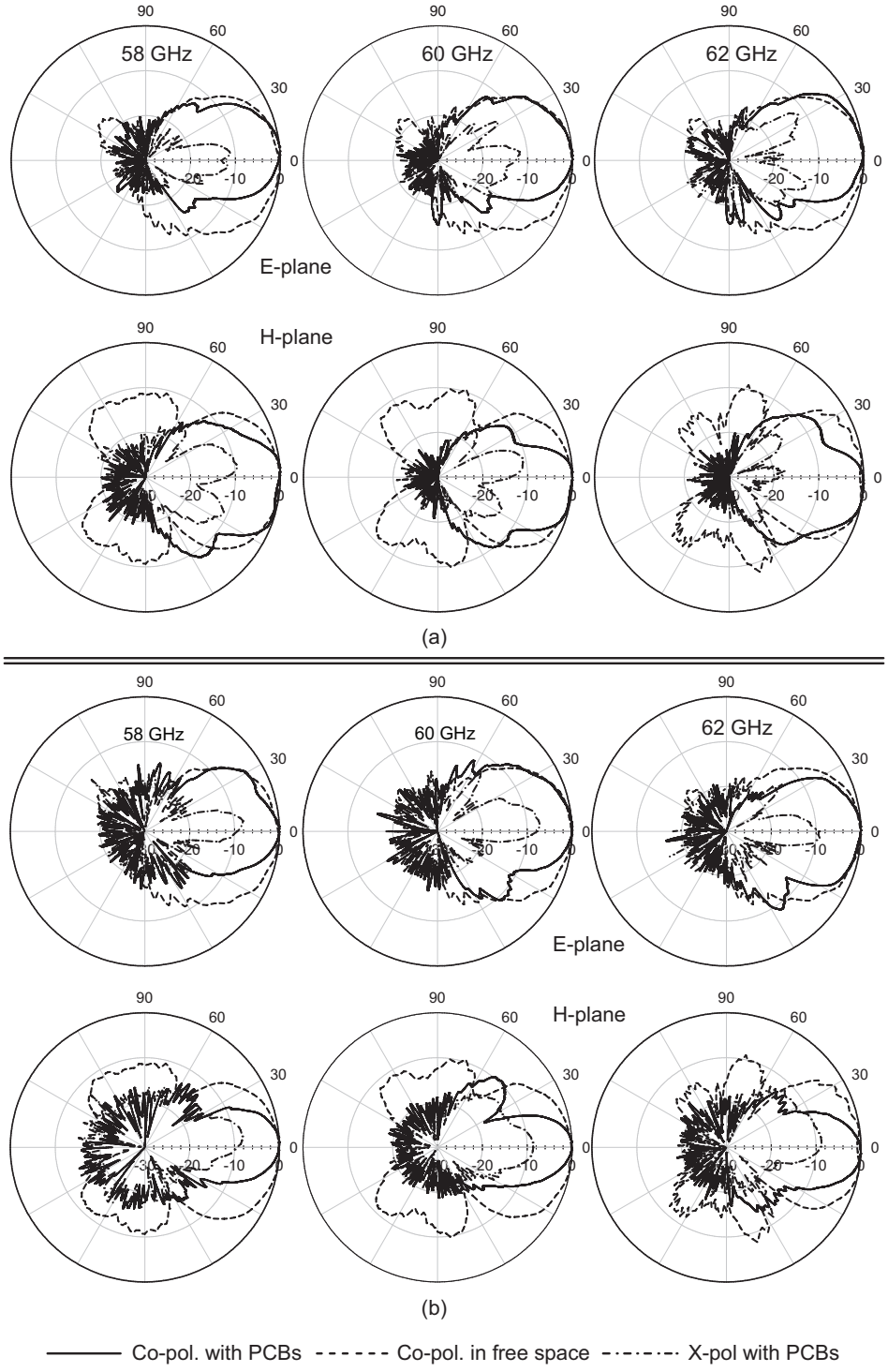

Figure 4.17: Measured radiation patterns of the 60 GHz Yagi-Uda antenna with two PCBs on top and bottom of the antenna: (a) without metal shield, (b) with box shielding.

for different h values, and the S_{11} response is not affected for h $\geq$ 2 mm. The measured radiation patterns are shown in Fig. 4.13 and agree well with simulations. The 60 GHz pattern vs. h are compared with the free space antenna in Fig. 4.14. Note that for the box with h = 2 mm, the aperture field distribution results in wider H-plane pattern and narrower E-plane patterns. As a result, the antenna gain for h = 2 mm is very similar to the free space gain as shown in Fig. 4.15(a). Also, the gain for h = 5 mm is considerably higher at 56-60 GHz than the free space case due to a sharpening in both the E- and H-plane patterns (Fig. 4.15(a)). The measured gain vs. h shows gain enhancement over free space for h = 5 - 10 mm, a dip at h = 4 mm (explained above) and a sharp drop in gain for h < 2 mm due to distortion in mutual coupling (Fig. 4.15(b)). The measurements agree well with simulations. The radiation patterns were also measured with two PCB boards, covered with metal and different electronic components, on top and bottom of the Yagi-Uda antenna and with a spacing of $\sim$ 5 mm (Fig. 4.16). The measured radiation patterns are compared to the free space pattern measurements for

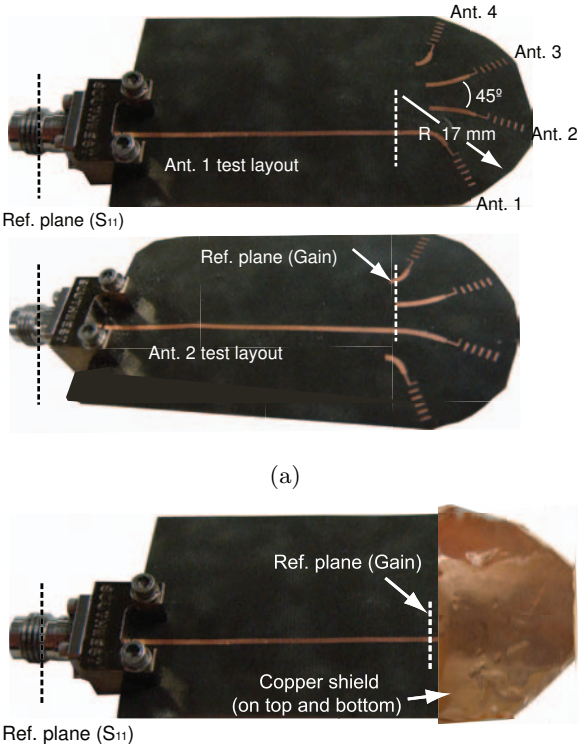

Figure 4.18: Fabricated 4-element switched-beam array of the 60 GHz Yagi-Uda antennas: (a) frees space case, (b) with top and bottom shielding planes.

two cases: not-shielded Yagi-Uda and shielded-box Yagi-Uda (Fig. 4.17). The E-plane patterns are very similar to the free space patterns and the H-plane patterns are narrower than the H-plane patterns in free space and agrees with previous measurements with top and bottom copper planes. This shows that the PCBs can act as top and bottom metal planes and that highly directive Yagi-Uda antennas can be integrated in complex laptop and mobile phones.

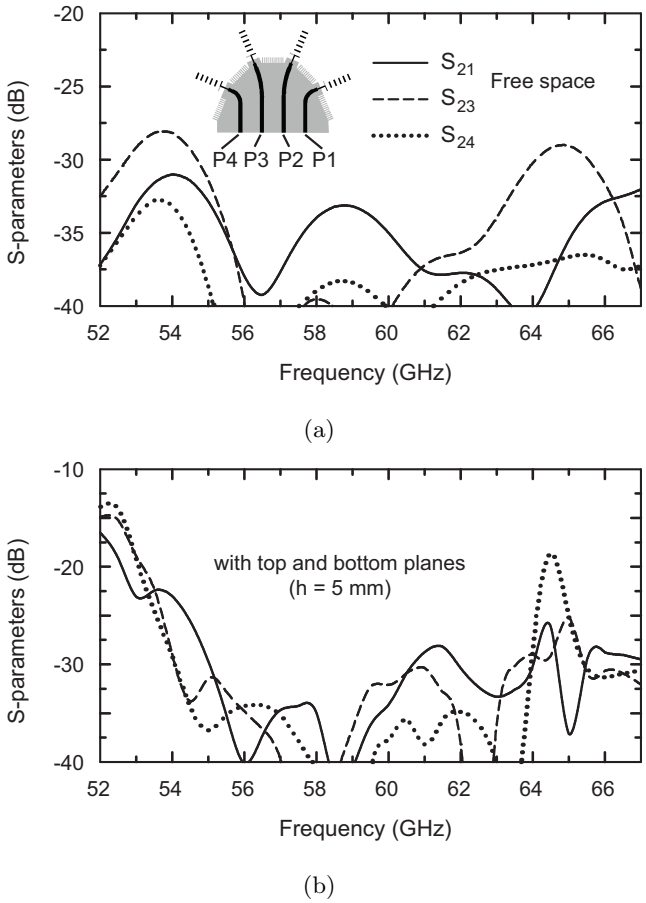

Figure 4.19: Simulated mutual coupling coefficients (Smn): (a) in free space, (b) with top and bottom metal planes for h = 5 mm.

4.4 4-Element Array

The single element Yagi-Uda antenna has a measured 3-dB beamwidth of 54° in the E-plane as shown in Fig. 4.3. Therefore, four Yagi-Uda antennas with an angular spacing of 45° can be used to cover a 180° radiation angle with a peak gain > 10

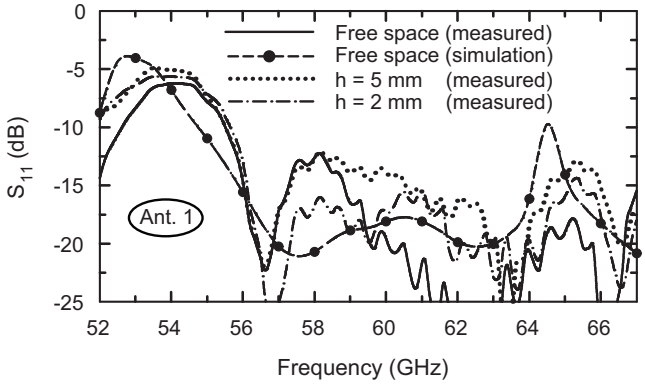

(a)

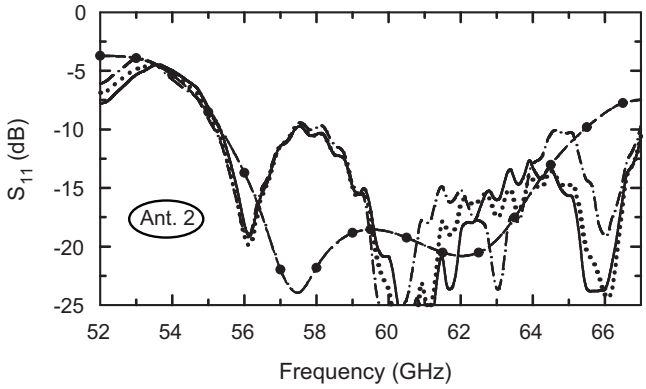

(b)

Figure 4.20: Measured S_{11} of : (a) Ant. 1 , (b) Ant. 2. Simulations shown for free space case only for Ant.1 and Ant. 2.

dB and with $<$ 3 dB gain variation over the whole coverage angle. A single-pole four-through (SP4T) switch can be used to switch between the four beams [66] or independent transceivers can be placed at each beam for increased data rates. Two fabricated 4-element Yagi-Uda arrays are shown in Fig. 4.18(a) with the microstrip feed line connected either to Ant. 1 or to Ant. 2. In effect, four different arrays were built to measure each element in the array, but only two are shown. In each case, the other three antenna feeds are left unloaded since it is virtually impossible to use commercial lumped-element resistive loads at 60 GHz (even 0201 resistors are not 50 Ω at 60 GHz). The open ends of the microstrip lines were covered by absorbers during the measurements to reduce their radiation effects on the antenna-under-test. Fig. 4.19 presents the simulated mutual coupling coefficients (S_{21}, S_{23} and S_{24}) in free space and with top and bottom copper planes (h = 5 mm) between the array elements. The mutual coupling is $<$ -25 dB at

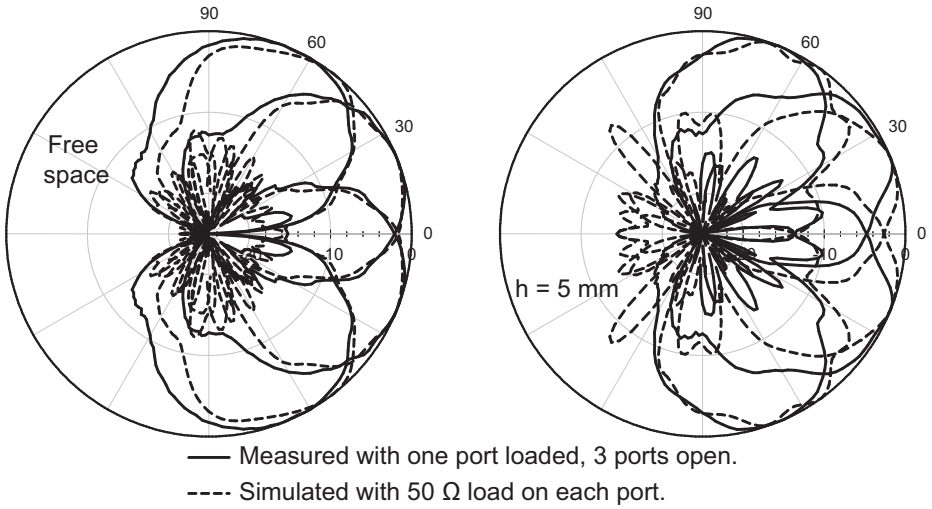

Figure 4.21: Measured and simulated E-plane patterns of the 4-element switched array at 60 GHz: in free space (left) and with top and bottom metal planes (right) for h = 5 mm.

52 - 67 GHz in free space and remains < -25 dB at 54 - 64 GHz with top and bottom metal planes (Fig. 4.19(a)). The measured S_{11} of Ant. 1 and Ant. 2 are presented in Fig. 4.20 in free space and with top and bottom copper sheets over the entire array (h = 2 and 5 mm). In this case, there was a semi-circular opening at the array edge as shown in Fig. 4.18(b). It is seen that the top and bottom ground planes have no effect on the measured impedance. Fig. 4.21 presents the measured and simulated E-plane patterns of the 4-elements in free space and with top and bottom copper planes at h = 5 mm. The measured patterns agree well with simulations, but show a dip of 5 dB at h = 5 mm instead of 3 dB due to the coupling from the unloaded antennas (no absorbers were used under the metal plans to cover the open ended feeds of the antennas). Simulations with three unloaded antennas for h = 5 mm agree well with measurements. It is clear that we can cover the +/- 180° range with < 3 dB amplitude variation. The absolute gain of Ant. 1 and Ant. 2 is also measured in free space and next to copper sheets on top and bottom of the array for h = 5 mm (Fig. 21). As expected from the single-element antenna measurements, the gain of the Yagi-Uda antenna is enhanced by the copper sheets for h = 5 mm due to the narrower H-plane patterns. The measured gain of Ant. 2 is lower than simulated gain and this is due to the coupling of adjacent unloaded antennas.

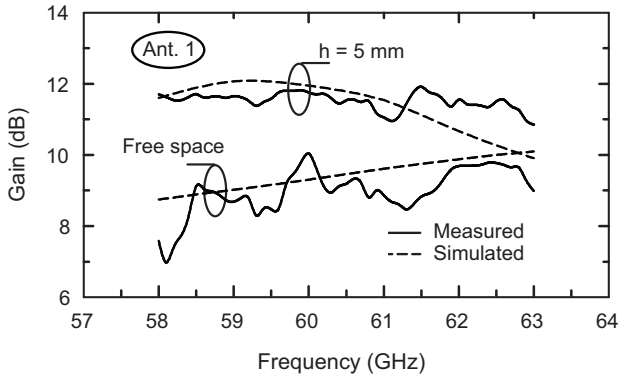

(a)

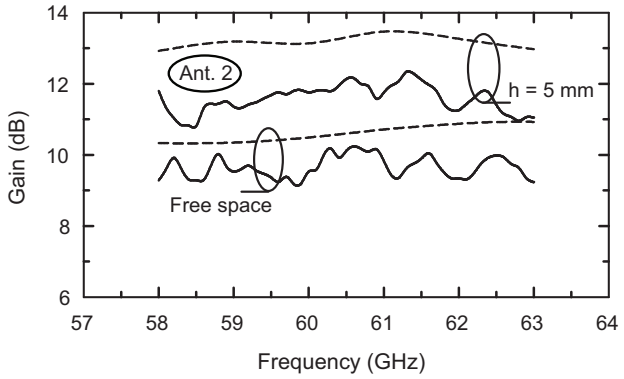

(b)

Figure 4.22: Measured and simulated gain of the switched array in free space and with copper sheets above and below (h = 5 mm): (a) Ant. 1, (b) Ant. 2. Simulations are done with matched ports at all antennas.

4.5 Conclusion

This chapter presented for the first time a comprehensive analysis and experimental characterization of 60 GHz Yagi-Uda antennas with shielding metal-planes. It is seen that the Yagi-Uda antenna performance can be enhanced with well designed shielding structures (metal-planes or boxes), and results in a gain improvement of 2 - 4 dB over the free-space case (gain = 12 - 14 dB at 60 GHz). The Yagi-Uda antenna was also characterized in a practical environment with printed circuit boards, and showed no degradation in performance.

Chapter 4 is mostly a reprint of the material that is submitted for publications in IEEE Transactions on Antennas and Propagation, 2010 . R. A. Alhalabi; Y. Chiou; G. M. Rebeiz. The dissertation author was the primary author of this material.

Chapter 5

Planar Millimeter-Wave Monopole Antennas

Omni-directional antennas are suitable for base-station applications, and of the most common omni-directional antennas is the monopole antenna. This antenna has been extensively studied for wideband and UWB applications in the 1 - 10 GHz range. A planar monopole fed by a grounded CPW line and with an impedance bandwidth $>$ 50% was presented by Johnson and Rahmat-Samii [67]. A microstrip-fed dual-frequency planar triangular monopole antenna at 1.4 - 2.7 GHz is demonstrated in [68]. A planar triangular monopole antenna for UWB communications with a VSWR $<$ 3 at 4 - 10 GHz was also presented in [69]. A planar inverted cone antenna with VSWR $<$ 2 from 1 to 10 GHz is presented in [70]. A compact UWB aperture antenna with extended band-notched design is presented in [71]. An elliptical disc monopole with a bandwidth from 1.21 GHz to $>$ 13 GHz with a VSWR $<$ 2 is reported in [72]. Abbosh and Bialkowski presented a method for designing UWB planar monopoles of circular and elliptical shape covering frequency band from 3 -1 0 GHz [73]. Alhalabi and Rebeiz presented microstrip fed-endfire angled dipole antennas with a gain of 3 - 5 dB using standard and corrugated (magnetic) ground planes [62].

This chapter presents a microstrip-fed planar mm-wave triangular and straight monopole antennas with ultra wideband impedance matching bandwidth and with almost omni-directional radiation patterns over the whole bandwidth. Also, two other modified planar monopole antennas with reduced cross-polarization levels are presented. The new designs are based on a localized current choke which greatly attenuates the

ground plane edge current and reduces the cross-polarization level. This results in improved patterns and lower cross-polarization but with a smaller impedance bandwidth.

5.1 Ultra-Wideband Monopole Antennas

Fig. 5.1(a) presents the layout of planar triangular ultra wide-band monopole antenna. The antenna is printed on a RT/Duroid 5880 substrate ($\epsilon_r = 2.2$) with a thickness of 15 mils (0.381 mm). The antenna is fed directly by a 50 Ω microstrip line, and the truncated ground plane of the microstrip feed serves as a ground plane for the monopole antenna. The HFSS simulated S_{11} for the planar triangular monopole antenna with three different flare angles is shown in Fig. 5.2. The triangular monopole length (L_2 in Fig. 5.1(a)) is kept the same for all three cases. For this specific case of $L_2 = 2.7$ mm, the flare angle should be $> 90°$ to achieve a wide impedance matching to 50 Ω. However, the monopole length can be modified for each flare angle to achieve approximately the same impedance bandwidth. A flare angle of 120° was chosen for our design with a simulated $S_{11} <$ -10 dB from 20.6 GHz to 33.5 GHz. For wide impedance bandwidth, it is not necessary to have a triangular shaped monopole. A straight monopole can actually achieve the same wide impedance bandwidth. The wide impdance bandwidth is mainly because of the currents flowing on the ground plane. Fig.5.1(b) presents the layout of planar straight monopole antenna. The antenna is also designed on a RT/Duroid 5880 substrate ($\epsilon_r = 2.2$) with a thickness of 15 mils (0.381 mm). The monopole antenna is matched to 50 Ω using a microstrip line, and the truncated ground plane of the microstrip feed serves as a ground plane for the monopole antenna. The input impedance of the ultra wide-band triangular and straight monopoles are measured using the 2.92 mm coaxial connector shown in Fig. 5.3(a), and the measured S_{11} is shown in Fig. 5.4(b). Time domain techniques were used to take the connector effects. These monopole antennas have ultra wideband characteristics with measured $S_{11} <$ -10 dB over a very wide frequency range (20.7 to 37.9 GHz for the triangular monopole and 18 - 42 GHz for the straight monopole). The radiation patterns of the ultra wideband monopole antennas are measured in the receive mode using a zero-bias schottky diode detector (Krytar model 303B) and a lock-in amplifier (Stanford Research Systems, SR830 DSP Lock-in Amplifier). The RF signal is amplitude modulated with a 1 kHz sine-wave signal and the rectified 1 kHz is measured. A thin absorber is used over the coaxial connector and the diode detector to reduce its scattering effects. The measured radiation

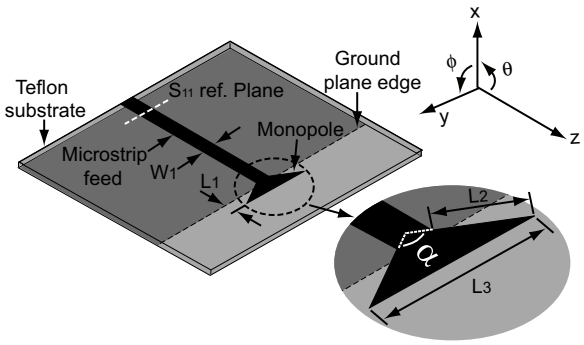

(a)

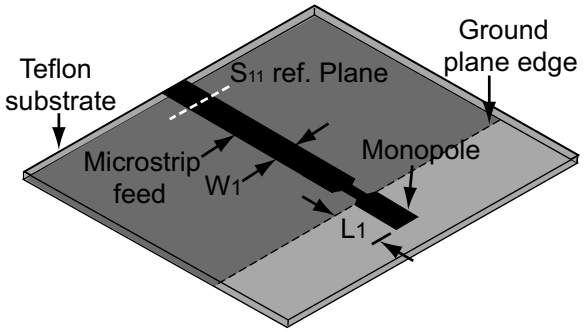

(b)

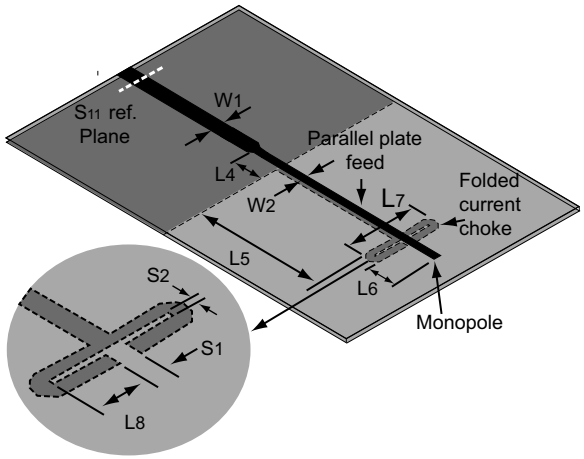

(c)

Figure 5.1: Ultra-wideband monopole antenna geometry: (a) Triangular: $\alpha = 120°$, $L_1 = 1.35$, $L_2 = 2.7$, $L_3 = 5.9$, (b) Straight: $L_4 = 2.4$, $L_5 = 0.9$, (b) modified monopole antenna geometry with local current choke: $L_6 = 3.1$, $L_7 = 8$, $L_8 = 2.7$, $L_9 = 6.5$, $L_{10} = 2.5$, $S_1 = 0.2$, $S_2 = 0.1$, $W_2 = 0.6$, microstrip line width (W_1) = 1.2, ground plane width = 22 (all dimensions are in mm).

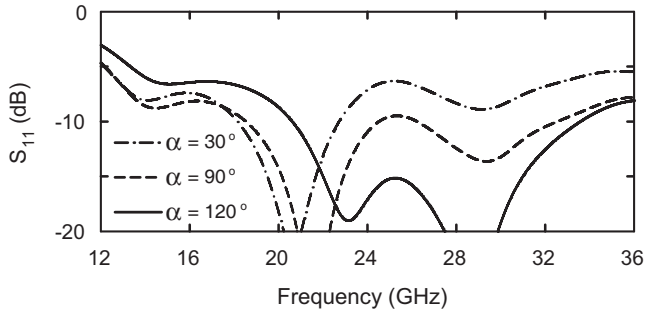

Figure 5.2: Simulated S_{11} of the triangular monopole for three different flare angles.

patterns at different frequencies in the three principal planes (xy, xz and yz planes) of the triangular and straight ultra wide band monopole antennas are shown in Fig. 5.5 and 5.6 respectively. The ultra-wideband monopole antennas have almost omni-directional patterns but with a very high cross-polarization component (E_ϕ) in the xy-plane. Fig. 5.7(b) presents the HFSS simulated surface current on the triangular and straight ultra-wideband monopole antennas at 24 GHz. It is clear that there are two main radiating currents: for the ultra-widwband triangular monopole the two radiating currents are the current along the edges of the triangular monopole and the y-directed current along the edge of the ground plane. The current along the triangular monopole edges has in turn a z-directed component which is responsible for the co-polarization radiation and a y-directed component. This component, along with the ground plane edge current, is the main source for the high cross-polarization radiation. The y-directed current along the front edge of the triangular monopole also contributes to the cross-polarization radiation. For the straight monopole, the currents are the z-directed current along the strip monopole and the y-directed current along the edge of the ground plane. The current along the strip monopole is responsible for the co-polarization radiation (E_θ) while the y-directed component, along the ground plane edge, is the main source for the high cross-polarization radiation (E_ϕ).

In order to reduce the cross-polarization component, the y-directed current along the ground plane edge should be eliminated and one should introduce an alternative path for the monopole ground return current. To do so, a modified design of the ultra wideband monopole antenna is introduced.

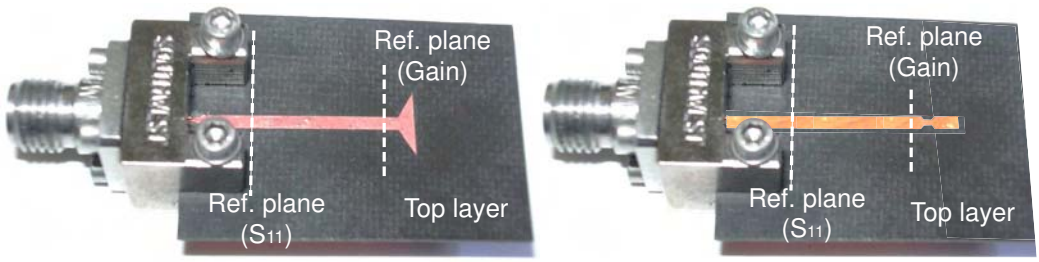

(a)

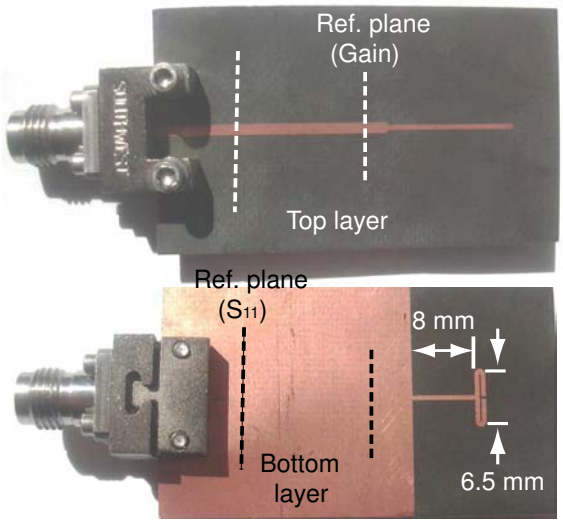

(b)

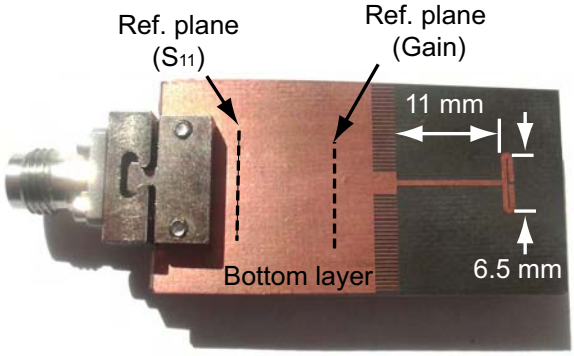

(c)

Figure 5.3: Fabricated planar monopole antennas: (a) Ultra-wideband monopoles (top side), (b) modified design with standard ground plane (top and bottom), (c) modified design with corrugated (magnetic) ground plane (bottom side).

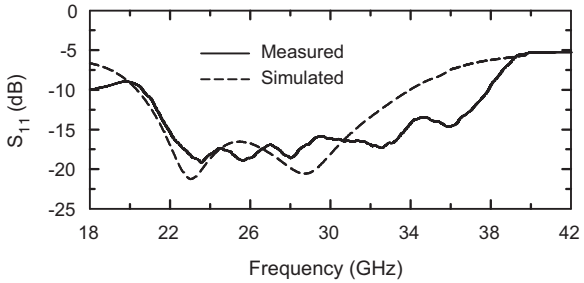

(a)

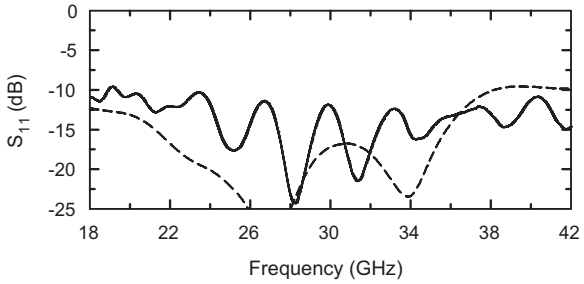

(b)

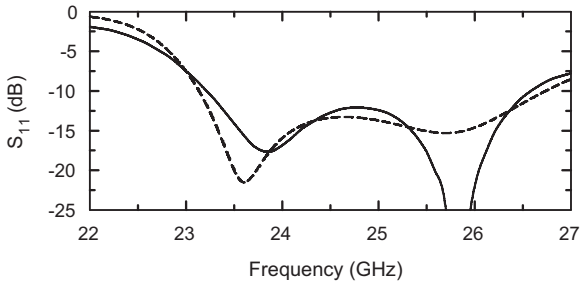

(c)

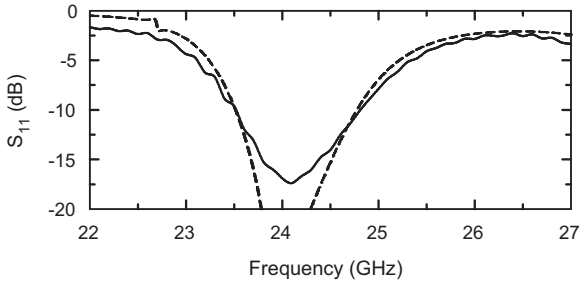

(d)

Figure 5.4: Measured and simulated S_{11} of: (a) triangular monopole antenna, (b) straight monopole, (c) modified design with standard ground plane, (d) modified design with magnetic ground plane.

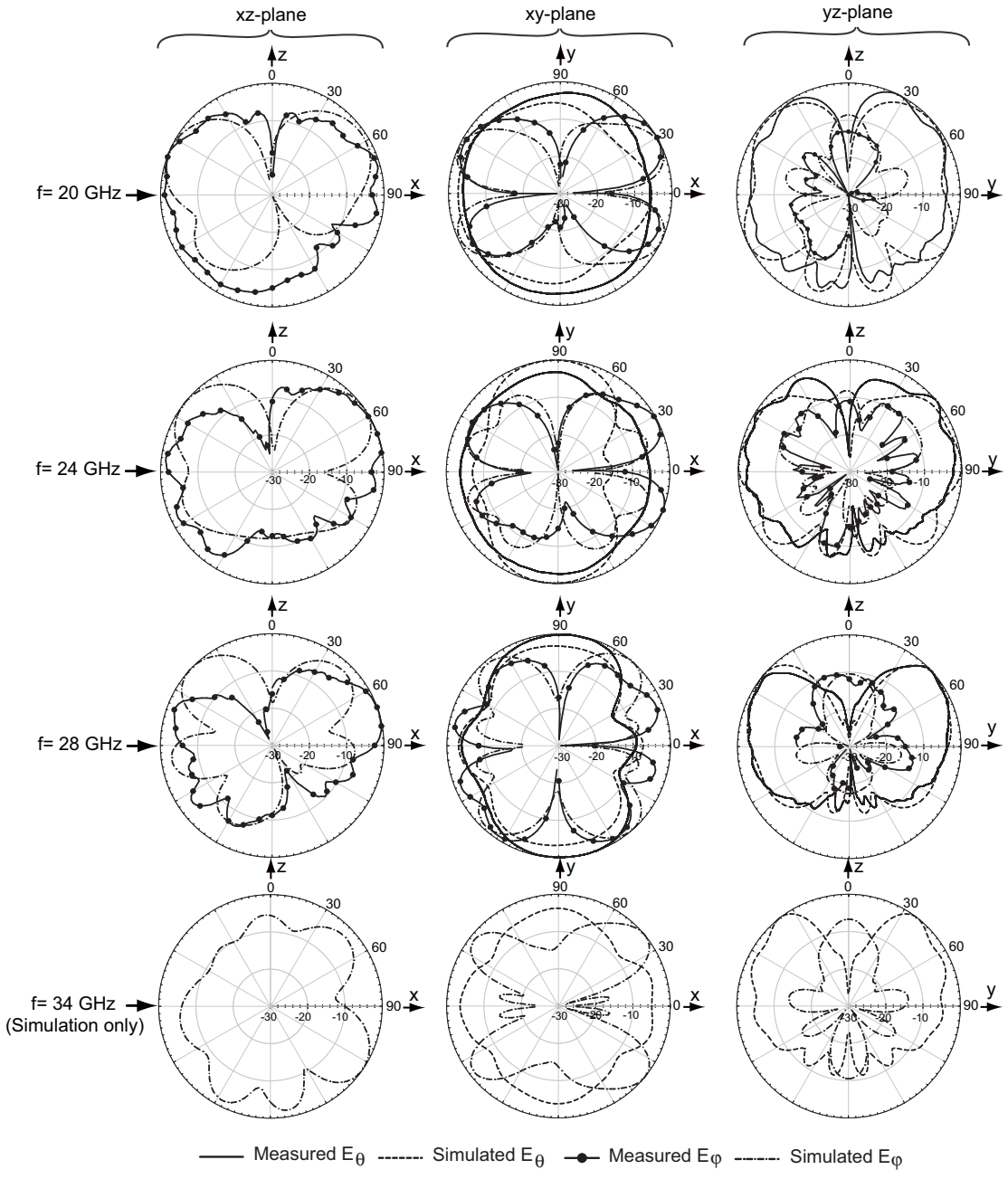

Figure 5.5: Measured and simulated radiation patterns of the ultra-wideband triangular monopole antenna.

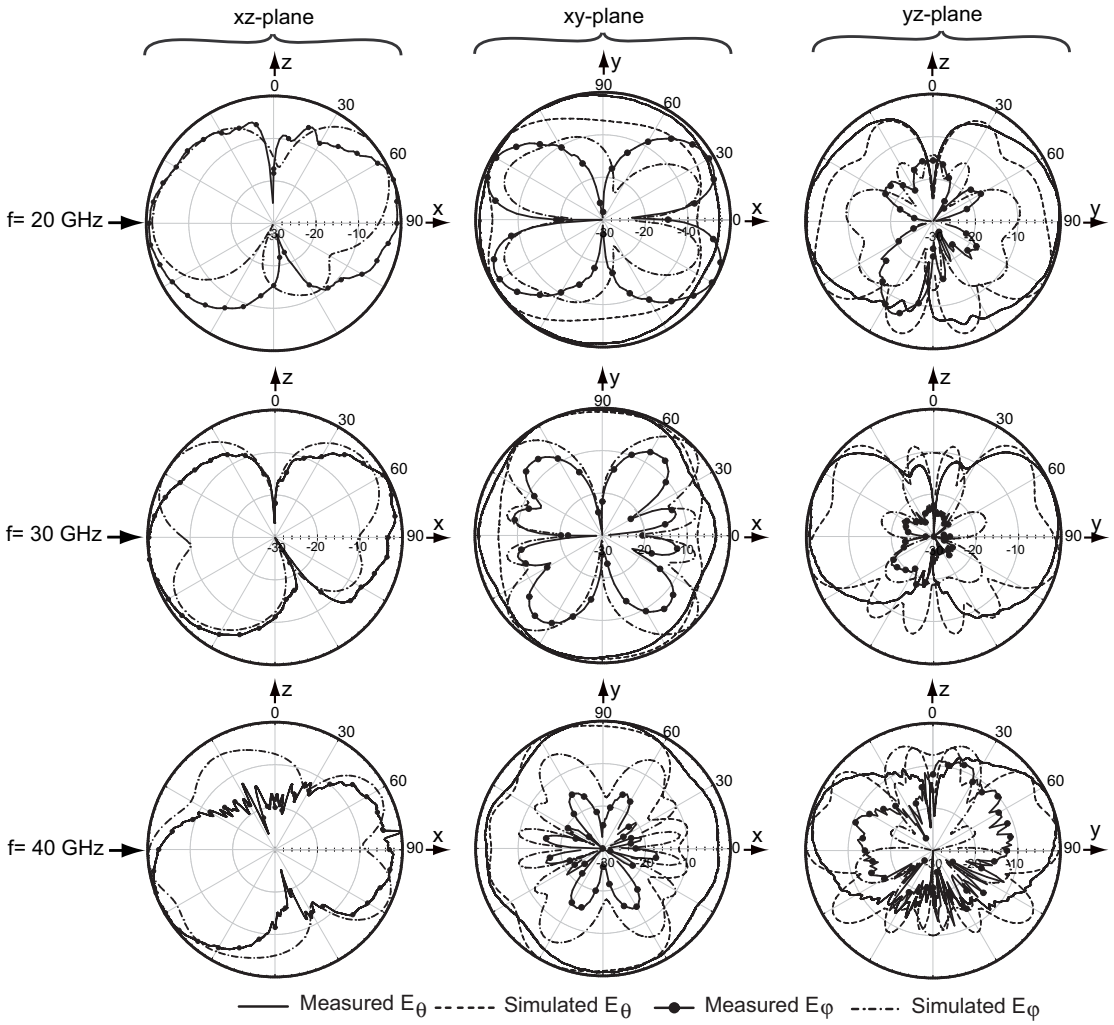

Figure 5.6: Measured and simulated radiation patterns of the ultra-wideband straight monopole antenna.

5.2 Monopole Antennas with Reduced Cross-Polarization Levels

In the new design, the radiating monopole is placed 8 mm away from the microstrip ground plane and a folded section is introduced between the microstrip ground plane edge and the radiating monopole (Fig. 5.1(c)). This folded section serves as a localized ground for the monopole antenna currents and allows a return path for the monopole current, while at the same time; result in low cross-polarization radiation since the currents in the folded section are 180° out of phase with each other. The best cancellation occurs when the currents in the folded section are exactly equal in

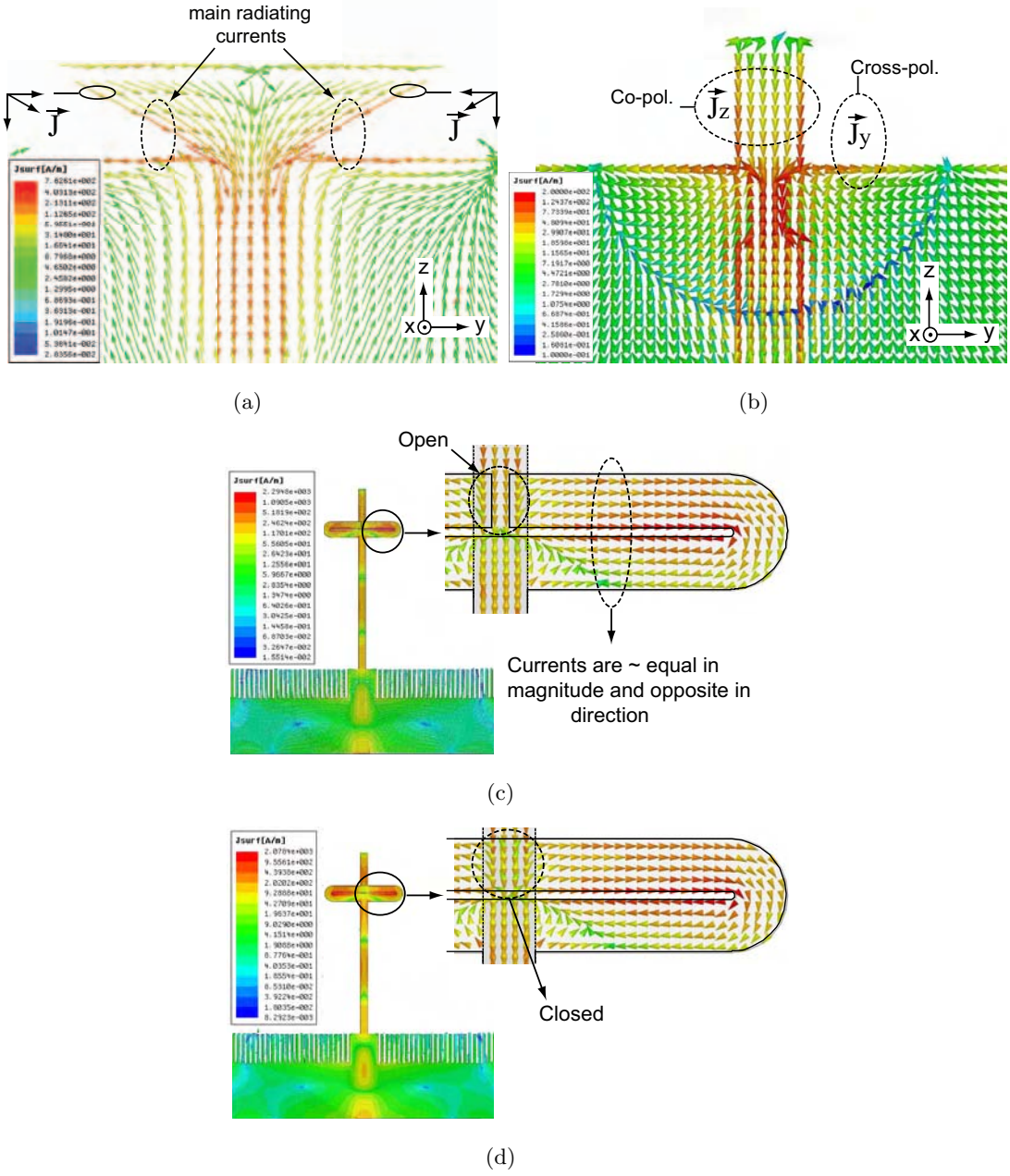

Figure 5.7: HFSS simulated surface current density at 24 GHz on: (a) triangular monopole antenna, (b) straight monopole, (c) modified monopole antenna with magnetic ground plane and with open folded-current choke, (d) with closed folded-current choke.

magnitude. The folded section can be designed with an open circuit or a short circuit in the middle (Fig. 5.7(c) and (5.7(d))), and both result in the same cross-polarization

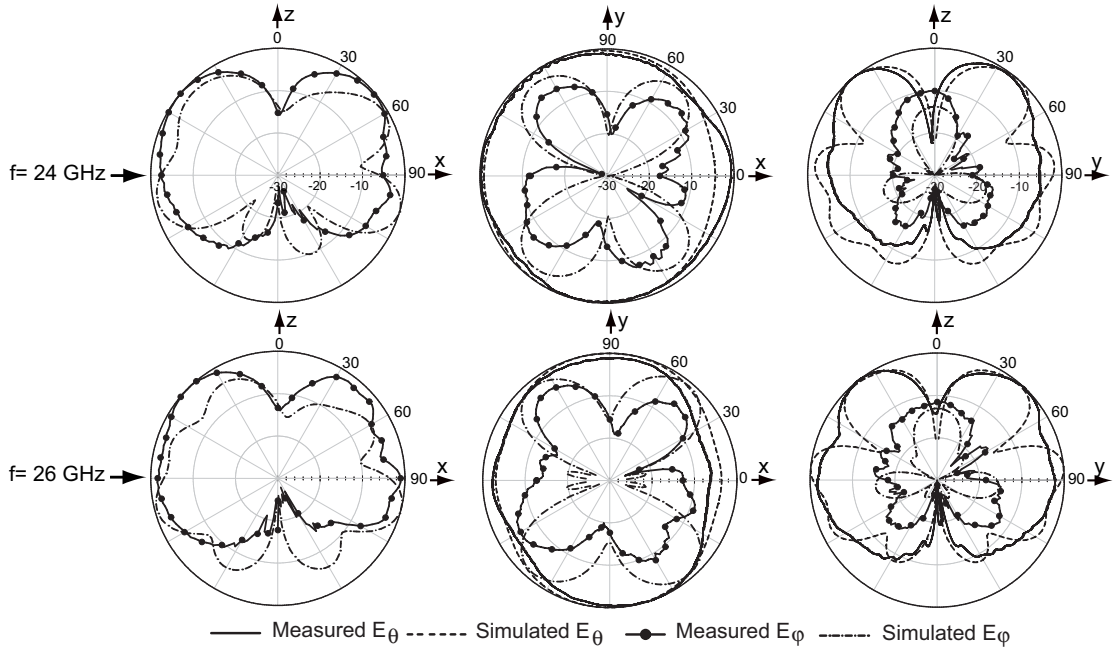

(a)

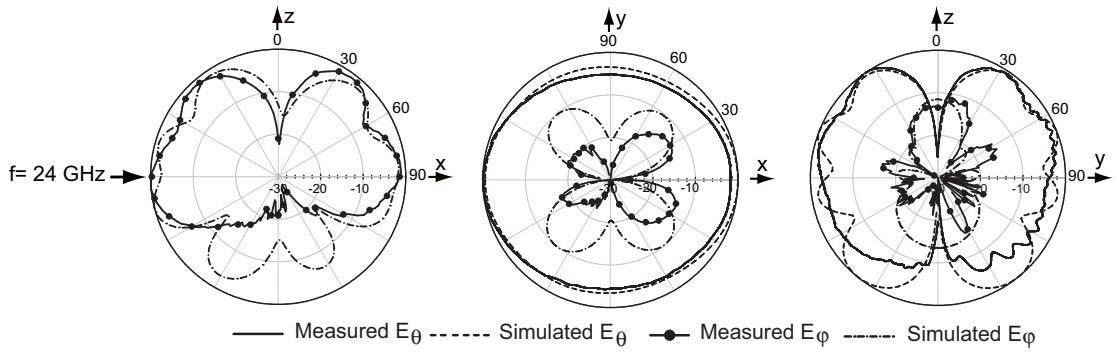

(b)

Figure 5.8: Measured and simulated radiation patterns of the modified monopole antennas: (a) with standard ground plane, (b) with magnetic ground plane.

performance and S_{11} bandwidth. The modified monopole antenna is built on a Rogers RT/Duroid 5880 substrates ($\epsilon_r = 2.2$) with a thickness of 15 mils (0.381 mm) as shown in Fig. 5.3(b). Fig. 5.8(a) presents the measured and simulated patterns at 24 and 26 GHz in the xz, xy and yz planes. Comparing the radiation patterns in the xy plane for this modified design with the ultra wideband monopole (Fig. 5.3(b) and Fig. 5.6), it is clear that the modified design has better radiation patterns with lower cross-polarization levels.

Still, the cross-polarization radiation has a -6 dB level, and this is due to the y-directed current in the truncated ground plane edge. The cross-polarization component (E_ϕ in the xy-plane) can be reduced further by introducing *lambda*/4 corrugations in the ground plane edge (Fig. 5.3(c)). These corrugations form a magnetic ground plane edge and greatly reduce the ground plane edge currents [62]. Fig. 5.8(b) presents the measured and simulated radiation patterns for the

modified monopole design with magnetic ground plane at 24 GHz, and the measured cross-polarization component in the xy-plane is significantly reduced (-13 dB).

The input impedance of both modified monopole designs is measured using the 2.92 mm Southwest microwave connectors (Fig. 5.3) with time domain techniques. The measured S_{11} of the modified monopole antenna with standard ground plane is < -10 dB from 23.1-26.7 GHz (Fig. 5.4(c)), while the modified monopole antenna with magnetic ground plane has a measured S_{11} < -10 dB from 23.5-24.8 GHz (Fig.5.4(d)). The magnetic ground plane results in a reduction in the operating bandwidth to 1 GHz, which makes the antenna not suitable for ultra wideband operation, but can still be used for narrowband systems [62].

5.3 Gain Measurements

The gain of the three planar monopole antennas is measured using the gain transfer method and a mm-wave network analyzer (Agilent PNA network analyzer E8361A). Two identical standard gain horn antennas (Dorado GH-42-20 [41]) are first measured (19.4 +/- 0.7 dB from 20-28 GHz) and the gain is consistent with the manufacturer values. One horn antenna is then replaced by the antenna under test and the gain of the monopole antenna under test is calculated from the difference between the measured S_{21} in both cases. The antenna impedance mismatch is not taken out of the measurement. However, the loss of the microstrip line between the antenna and the Southwest connector is measured independently (0.22 dB/cm) and is taken out from the measurements. This places the reference plane at the microstrip line as shown in Fig. 5.3. Fig. 5.9 presents the measured peak gain in the xy plane of the three monopole antennas. The measured gain of the ultra wideband monopole antenna ranges from -4.0 to +1.5 dB at 22-30 GHz while the modified monopole antenna with standard ground plane has a measured gain of -0.8 to +1.6 dB at 23-26 GHz; and the modified monopole design with magnetic ground plane has a narrower bandwidth with a measured gain of

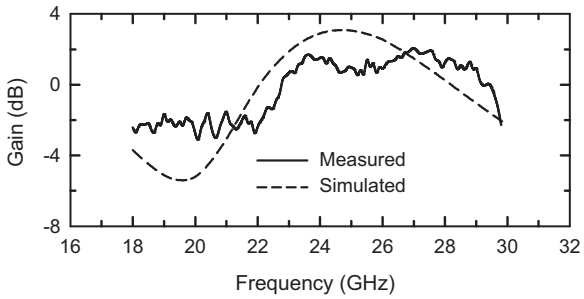

(a)

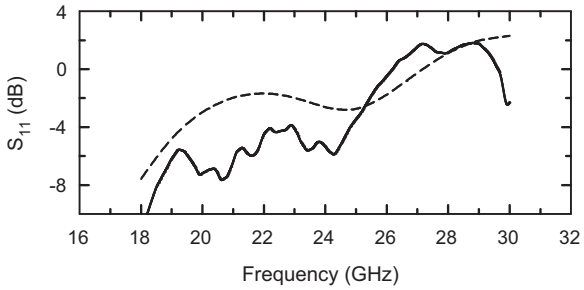

(b)

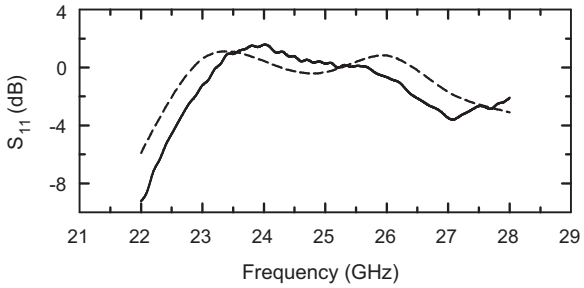

(c)

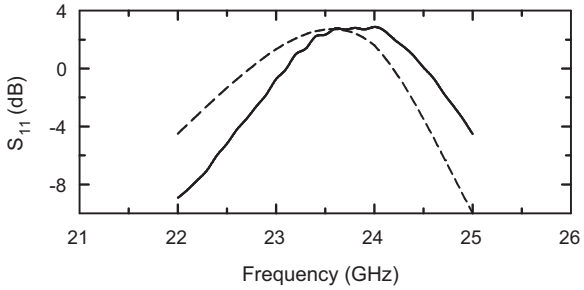

(d)

Figure 5.9: Measured and simulated gain of: (a) Triangular, (b) straight ultra-wideband monopole, (c) monopomodified design with standard ground plane, (d) modified design with magnetic ground plane.

Table 5.1: Measurement results summary.

Antenna	UWB-monopole	Modified monopole / standard G. P.	Modified monopole / magnetic G. P.
S_{11}<-10 dB (GHz)	18-42	23.1-26.7	23.5-24.8
X-pol. level (dB)	~0	-6.0	-13.0
Gain (dB)	-4.0 - +1.5	-0.8 - +1.6	+0.1 - +2.9
Efficiency	> 90%		> 90%

0.1 to 2.9 dB at 23.5-24.5 GHz and still maintaining near omni-directional patterns in the xy plane. The HFSS simulated radiation efficiency (Gain/Directivity) is 93-96% at 24 GHz for the different monopole antennas when referenced to the antenna port (no transmission-line loss). The measured gains are in agreement with simulations (Table 5.1).

5.4 Conclusion

This chapter presented planar monopole antennas for mm-wave base-station applications. Triangular and straight monopole antennas with very wideband (18-42 GHz) and with omni-directional radiation patterns are presented. These ultra-wideband monopoles have high cross-polarization levels. Novel planar monopole antenna utilizing integrated folded current chokes is presented and resulted in a lower cross-polarization level. The cross-polarization level is reduced further by introducing $\lambda/4$-length corrugations in the edge of the ground plane edge.

Chapter 5 is mostly a reprint of the material that is submitted for publications in IEEE Transactions on Antennas and Propagation, 2010 . Ramadan A. Alhalabi; Gabriel M. Rebeiz. The dissertation author was the primary author of this material.

Chapter 6

High-Efficiency On-Chip Electromagnetically-Coupled MM-Wave Silicon Microstrip Antennas

6.1 Introduction

Silicon substrates introduce special challenges for high efficiency millimeter-wave on-chip antennas. First, their low resistivity of 0.1-10 Ω-cm results in high dielectric loss and significantly reduces the antenna efficiency. Second, TE and TM surface waves are easily triggered in 200-500 μm thick silicon substrates and can have serious detrimental effects on the antenna pattern and efficiency [74, 75]. In the past few years, a lot of work has been done on on-chip antennas. A 24 GHz transmitter with on-chip zigzag dipole with a measured gain around -12 dB is presented in [76]. Zhang et al. presented on-chip inverted-F and quasi-Yagi antennas with gains of -19 dB and -12.5 dB at 61 GHz and 65 GHz, respectively [25]. A 60 GHz millimeter-wave on-chip dipole antenna with a gain of -10 dB in a 0.18 μm CMOS process is presented in [26]. Hsu et al. presented a 60 GHz CPW-fed on-chip Yagi-Uda antenna with a measured gain of -10 dB [48]. A 140 GHz receiver with -25 dB gain on-chip antenna is presented in [31]. A triangular loop antenna adjacent to a lossy silicon substrate is presented in [32]; the antenna has a simulated gain of -0.4 dB at 60 GHz and a measured gain of 0.9 dB using

a scaled model at 2 GHz. A Yagi-Uda array of wire-bond antennas with a measured gain of 8 dB at 40 GHz is presented in [34]. This antenna occupies a large space on wafer, and is not suitable for dense integrated circuits. Wu et al. also presented 60 GHz bond-wire antennas with ∼30% efficiency [33]. Hirokawa et al. presented a dipole antenna on a thick resin layer on the back of a silicon chip with a gain of 3.1 dB at 60 GHz [30]. Except for the bondwire and the thick resin layer antenna, all integrated circuit antennas have low gain and low efficiency at mm-wave frequencies. This chapter presents the design and measurement of a high-efficiency electromagnetically-coupled W-band on-chip microstrip antenna. The antenna design eliminates the effects of the silicon substrate by shielding the microstrip antenna using a ground plane made from the silicon metallization layers. However, the thickness of the metal/SiO_2 layers above the silicon substrate is only 10-12 μm in most RF processes (IBM 8HP, 9RF, etc.) and it is hard to build efficient antennas with such a ground spacing. A 125 μm substrate is therefore added on top of the silicon chip so as to have enough ground-plane spacing for efficient radiation.

6.2 Antenna Design

6.2.1 Geometry

Fig. 6.1 presents the layout of the 94 GHz EM-coupled on-chip microstrip antenna. The microstrip antenna is integrated on a quartz substrate placed on top of silicon RFIC with a thickness h = 125 μm and a dielectric constant ϵ_r = 3.8. No via holes are used, and the feed between the silicon RFIC top metal layer (AM layer) and the microstrip antenna is achieved using electromagnetic fringing-field coupling. The ground plane of the microstrip antenna and the electromagnetic feed-probe is fabricated using the MQ layer, and isolates the antenna from the silicon substrate. Also, 40x40 μm metal squares are introduced on the LY layer to satisfy the metal density rules. These metal squares are tied to the silicon substrate and they can have a detrimental effect on the antenna performance if not well modeled.

6.2.2 Radiation Efficiency and Input Impedance vs. h and ϵ_r

It is well known that the radiation efficiency of microstrip antenna increases as ϵ_r decreases since the fields become loosely tied to the ground plane and the fring-

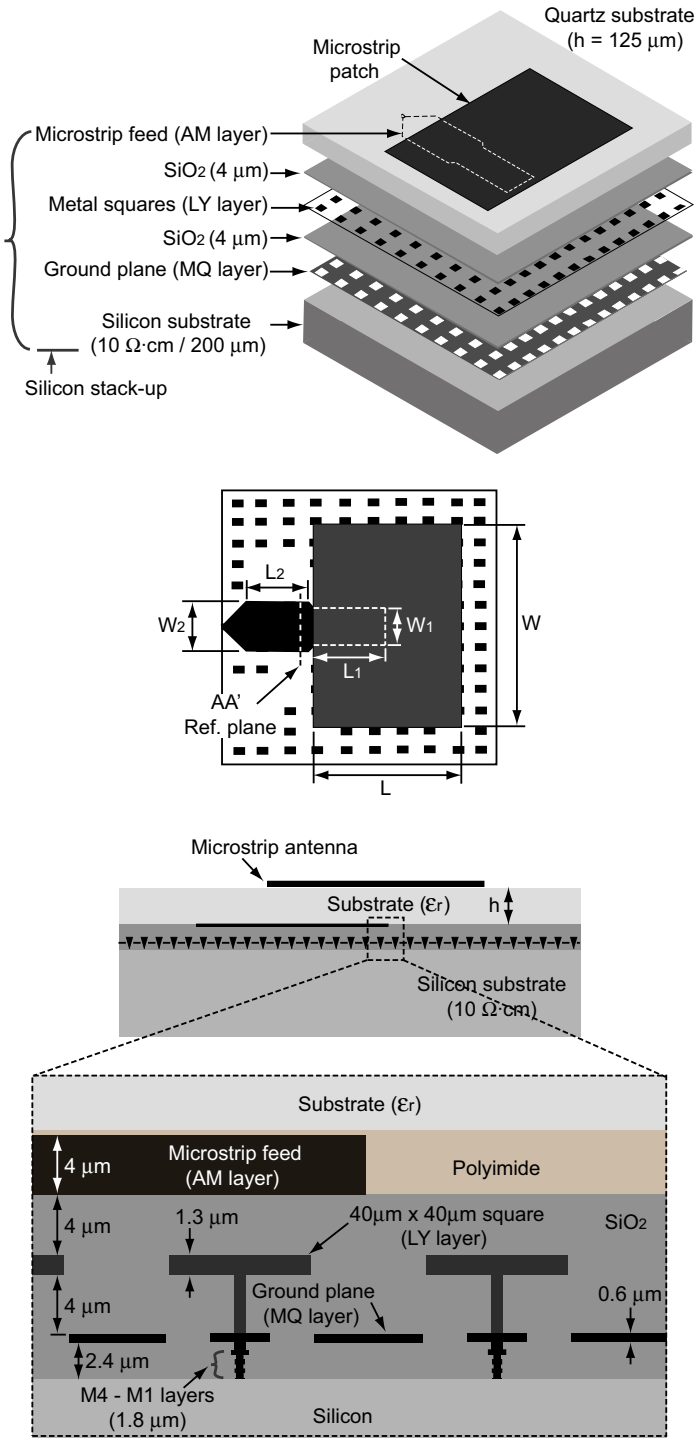

Figure 6.1: On-chip EM-coupled microstrip antenna geometry: L = 690, W = 970, L_1 = 350, W_1 = 180, L_2 = 310, W_2 = 230 (all dimensions are in μm).

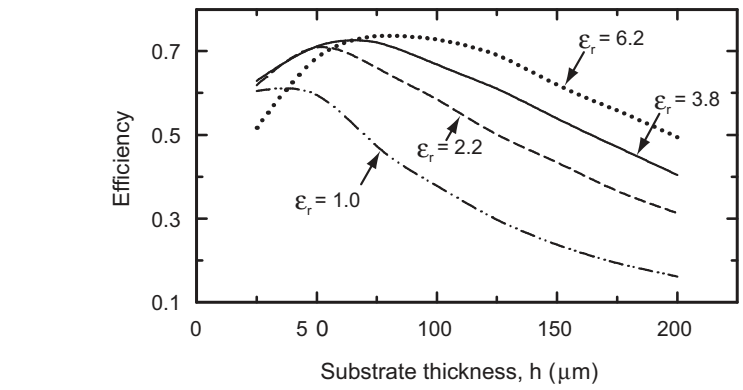

(a)

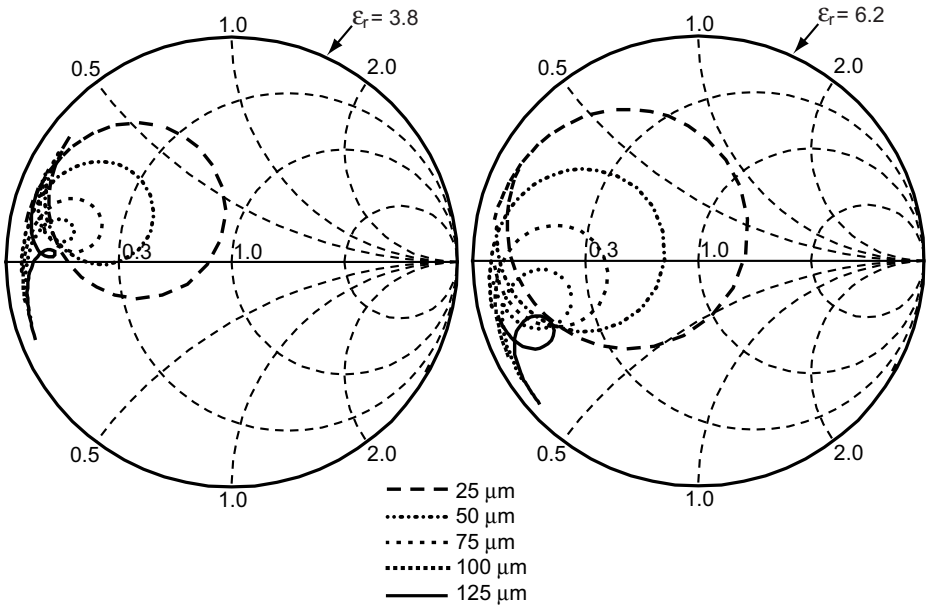

(b)

Figure 6.2: HFSS simulated: (a) radiation efficiency vs. h for different ϵ_r, (b) input impedance referenced to 10 Ω for h = 25-125 μm with ϵ_r = 3.8 and 6.2.

ing fields are increased at the antenna edges. The radiation efficiency of the antenna also increases as h increases until the coupling into the TM_0 substrate mode starts to become significant [77]. However, for electromagnetically-coupled antennas, the amount of coupling from the feed line to the antenna puts another limit on the allowed antenna substrate thickness and on the dielectric constant. The coupling from the microstrip feed to the antenna increases as h decreases and ϵ_r increases. The thickness and the dielectric constant underneath the feed line also affect the coupling from the microstrip line to the antenna. The fringing field coupling is enhanced by reducing the dielectric

constant and increasing the thickness underneath the feed line. However, in silicon chips, the microstrip line is located on SiO_2 layer with a dielectric constant of ~ 4. Also, the dielectric thickness underneath the feed line is very low and depends on the process. In most RF CMOS and SiGe processes, the total thickness between the first thick metal layer and the top metal layer is 6-10 μm [78]. Fig. 6.2(a) presents the HFSS simulated radiation efficiency of the EM-coupled antenna vs. substrate thickness for ϵ_r = 1, 2.2, 3.8 and 6.2. The simulations show that an efficiency of $\sim$ 70% is achievable for h = 50-100 μm with ϵ_r = 2.2 - 6.2, respectively. The antenna dimensions were modified for each case so that the radiation efficiency peaks at 96-98 GHz. For a small h where the coupling is sufficient (h $<$ 50 μm), an increase in ϵ_r reduces the efficiency since it results in a more narrowband antenna. However, for a larger substrate thickness (h $>$ 75-100 μm),increasing the dielectric constant significantly improves the radiation efficiency by enhancing the fringing field coupling. For example, for h = 100 μm, the simulated radiation efficiency increases from 38% to 73% by increasing ϵ_r from 1.0 to 6.2. Fig. 6.2(b) presents the simulated input impedance of the EM-coupled antenna vs. h for ϵ_r = 3.8 and 6.2 (Smith-chart Z_0 = 10 Ω). It is clear that the antenna input impedance is very low (8-1.2 Ω for ϵ_r = 3.8) due to the small separation between the microstrip line and the MQ-layer ground plane ($\sim$9 μm) compared to the separation between the microstrip line and the antenna (25-125 μm). The input impedance increases as h decreases and also for a higher ϵ_r due to the higher fringing-field coupling. The low microstrip antenna impedance at plane AA' (see Fig. 6.1) necessitates a quarter-wave matching network. This is accomplished using a wide microstrip line in the top metal layer. The microstrip antenna impedance at plane AA' is 2-1.2 Ω for h=100-125 μm and ϵ_r=3.8, and the $\lambda/4$ line impedance is 10-8 Ω (W_2 = 150-200 μm, L_2 =310 μm). The $\lambda/4$ line has a simulated loss of 0.66 dB/mm at 94 GHz, and reduces the antenna efficiency from 67-61% to 64-57%.

6.2.3 Radiation Efficiency vs. L_1 and W_1

The antenna radiation efficiency is affected by changing the coupling region length L_1 of the microstrip feed line, and also by changing the width of the microstrip line W_1 underneath the antenna. Fig. 6.3 presents the simulated radiation efficiency for different values of L_1 and W_1. The coupling reaches a maximum value when the feed line open end approaches the middle of the microstrip antenna [79]. The coupling from

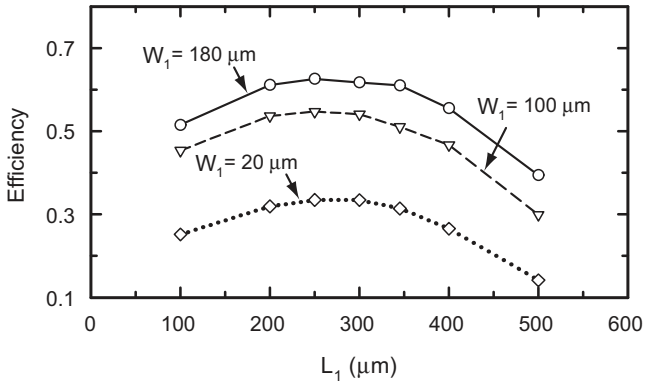

Figure 6.3: HFSS simulated radiation efficiency vs. L_1 and W_1 for h = 125 μm and ϵ_r = 3.8.

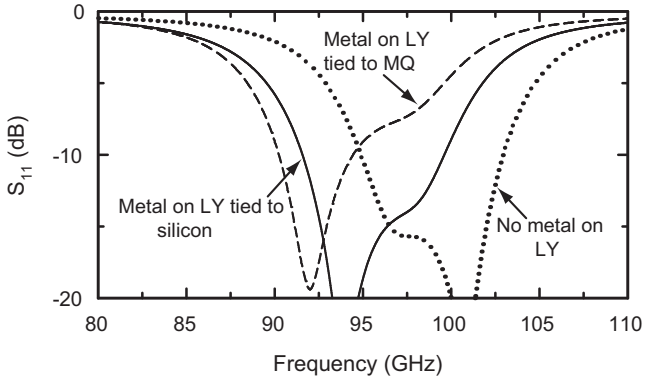

(a)

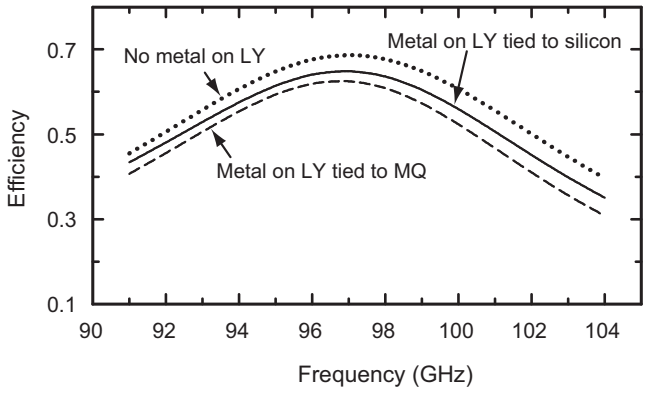

(b)

Figure 6.4: HFSS simulations with and without metals on LY layer: (a) S_{11}, (b) radiation efficiency.

the feed line to the microstrip antenna is also enhanced as the width of the feed line increases due to the increase in the fringing field area.

6.2.4 Effects of LY-layer

Fig. 6.4 presents the simulated S_{11} and radiation efficiency of the antenna with and without metal on the LY layer. This layer is between the MQ layer (ground plane) and the AM layer (microstrip feed line) and has its own metal density rules for RFIC fabrication. As seen in Fig. 6.4(a), the LY metal results in a small shift in the simulated S_{11}. The microstrip feed on the AM layer remained the same for the simulations with and without the LY layer, but it can be modified for each case to get the same S_{11}. The simulated antenna radiation efficiency is slightly reduced with 40x40 μm-squares on the LY layer due to the slight reduction of coupling from the microstrip line to the antenna (Fig. 6.4(b)). The metal squares on the LY layer can be either tied to the ground plane (MQ-layer) or go through 44x44 μm-square openings in the MQ layer and are then tied directly to the silicon substrate. The radiation efficiency is slightly lower if the LY squares are tied to the MQ layer ground plane since in this case, the ground plane is effectively closer to the feed line. Also, since the metal density rules on the MQ layer do not allow a continuous ground plane metal sheet, the case with openings in the MQ layer and with LY metal layer tied to the silicon substrate was chosen for our design.

6.2.5 Mutual Coupling Between Adjacent Antennas

Fig. 6.5 shows the simulated E- and H-plane coupling coefficient (S_{21}) between two antennas with center-to-center spacing of d = 1.6 mm ($0.5\lambda_0$ at 95 GHz). The simulated H-plane coupling is slightly higher since the antenna edges are closer in the H-plane configuration for the same center to center spacing. In both cases the simulated S_{21} is $<$ -20 dB over the antenna bandwidth which makes these antennas ideal for on-chip phased arrays or power combining.

6.3 Measurements

6.3.1 Input Impedance and Radiation Patterns

The 94 GHz EM-coupled on-chip microstrip patch antenna fabricated using the IBM 8HP process is shown in Fig. 6.6(a). A 125 μm-thick quartz substrate is

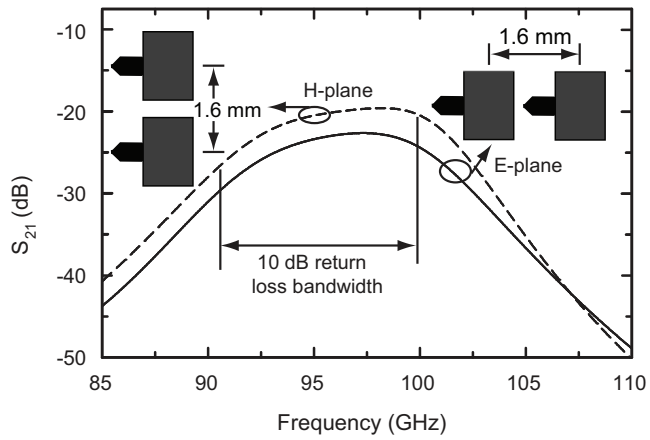

Figure 6.5: HFSS simulated coupling coefficient (S_{21}) in the E- and H-plane for d = 1.6 mm ($0.5\lambda_0$ at 95 GHz).

attached to the silicon chip using a small amount of epoxy placed at the corners. The input impedance of the antenna is measured using a CPW probe located 1.1 mm from the antenna (Fig 6.6(a)), and the measured S_{11} agrees well with simulations with a measured -10 dB bandwidth of 91.7-98.5 GHz. (Fig. 6.6(b)). We have found that the resonant frequency can shift to 86 GHz if there is residual epoxy between the quartz substrate and the silicon die. Therefore, it is essential to mount the quartz microstrip antenna with care on the silicon wafer. The H-plane radiation patterns are measured in the receive mode using a waveguide mm-wave diode detector. The diode detector was connected to the antenna feed using a W-band GSG probe. A special circular arm set-up is used above the on-chip antenna and allows for a radial scan in the H-plane (Fig. 6.7). The transmit antenna is a W-band horn with a gain of 23 dB placed at R $\simeq$ 28 cm from the on-chip antenna (well into the far field). Fig. 6.8 presents the measured and simulated radiation patterns at 90-100 GHz and with good agreement. Due to the metal-chuck and CPW probe positioner, one can notice some standing waves in the measured patterns. Also, due to the GSG probe, we could not obtain reliable E-plane measurements.

6.3.2 Gain

The absolute gain of the W-band on-chip antenna is measured using the set-up shown in Fig. 6.7 and with a calibrated Agilent Power Meter (E4417). The gain is obtained using the Friis transmission formula. The loss of the 1.1 mm on-chip microstrip line and the CPW waveguide probe are normalized out of the measurement (a

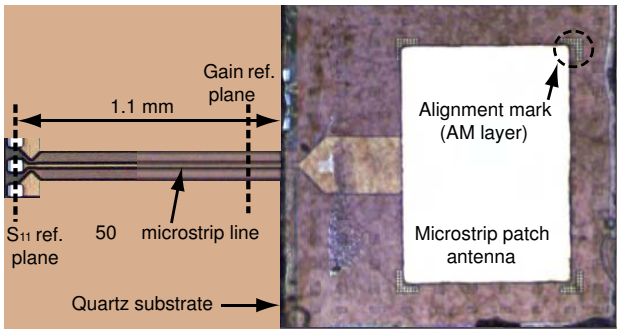

(a)

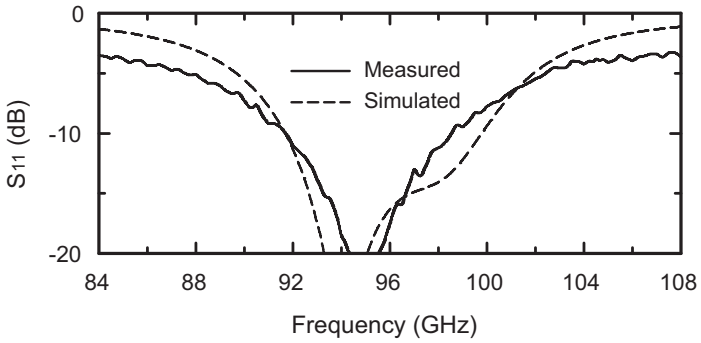

(b)

Figure 6.6: (a) Fabricated on-chip EM-coupled microstrip antenna, (b) measured and simulated S_{11}.

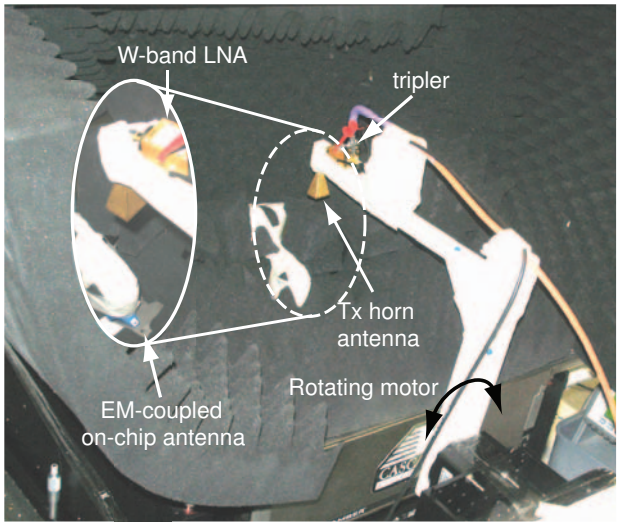

Figure 6.7: Set-up for radiation patterns and gain measurements.

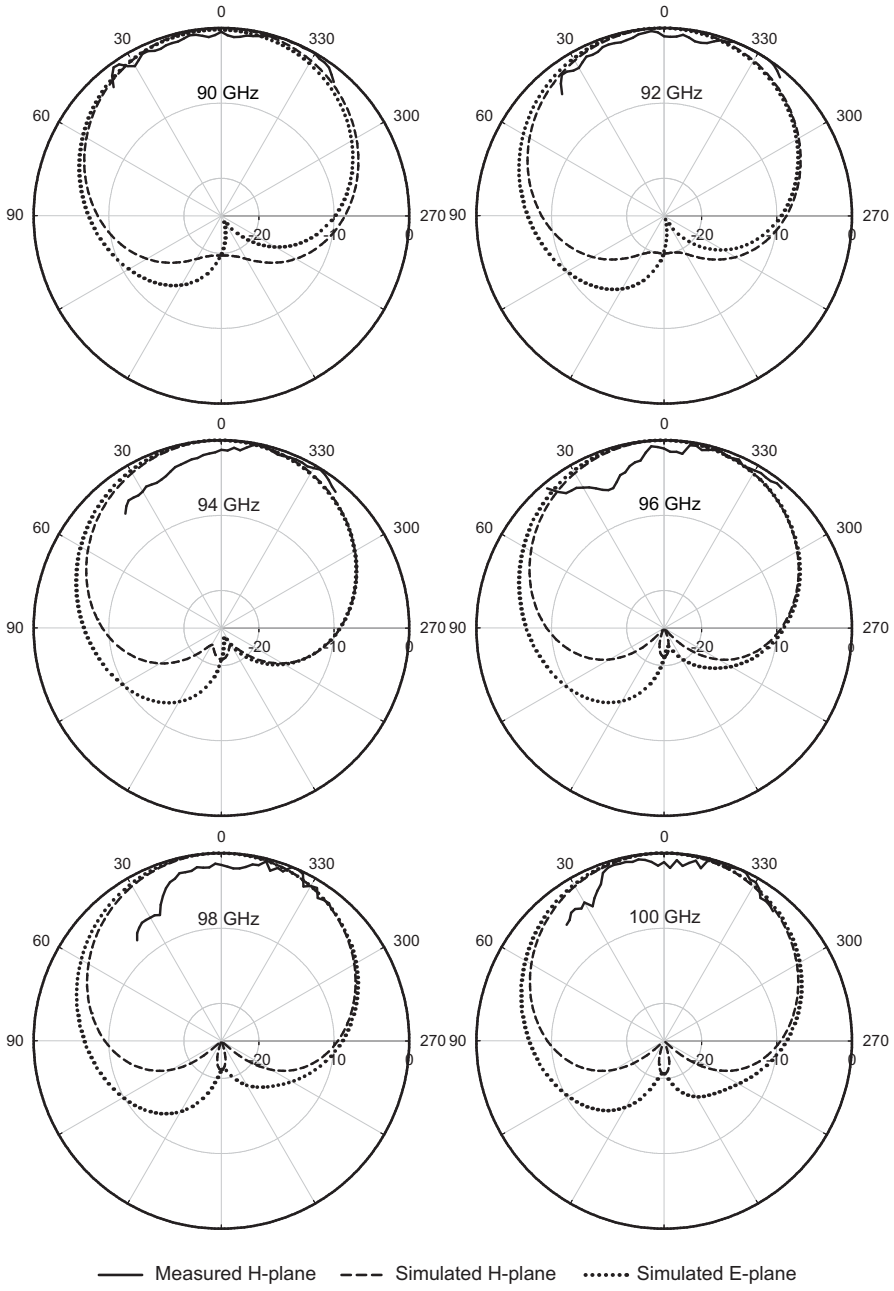

Figure 6.8: Measured and simulated radiation patterns of the 94 GHz EM-coupled on-chip microstrip antenna.

back-to-back probe-microstrip-probe was measured independently). Fig. 6.9 presents the measured peak gain of the on-chip antenna at 91-100 GHz and agrees well with simulations. Note that the on-chip antenna has an efficiency of 50-57% (3.0-2.4 dB loss) at 94-98 GHz, which is excellent for W-band frequencies. This is to our knowledge, the

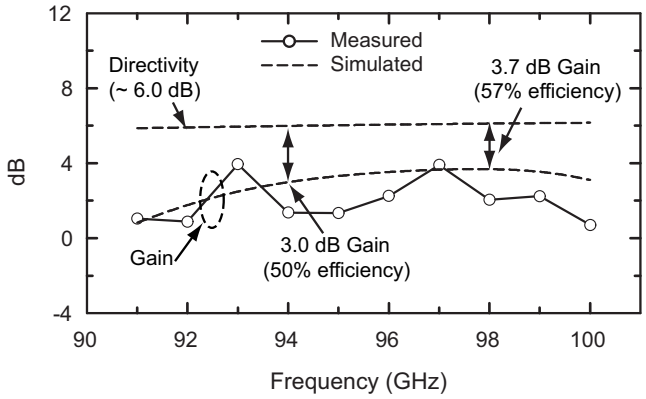

Figure 6.9: Measured and simulated gain of the EM-coupled on-chip microstrip antenna.

highest efficiency on-chip silicon antenna to-date.

6.4 Conclusion

This chapter presented the first on-chip high-efficiency mm-wave microstrip antenna to-date. The design is compatible with a variety of other antennas such as a differentially fed microstrip antenna, a slot-ring antenna, a double-slot antenna, all placed on the dielectric substrate. Also, the substrate need not be quartz, but can be Teflon, LTCC (ceramic), or even a high resistivity silicon wafer. The design can also be scaled to different frequencies such as 60 GHz or 140 GHz.

Chapter 6 is mostly a reprint of the material that is submitted for publications in IEEE Transactions on Antennas and Propagation, 2010 . Ramadan A. Alhalabi; Gabriel M. Rebeiz. The dissertation author was the primary author of this material.

Chapter 7

Conclusion and Future Work

7.1 Conclusion

The thesis presented different planar antenna prototypes suitable for different applications at mm-wave frequencies. A millimeter-wave end-fire dipole antennas at 24 and 60 GHz with applications as single element radiators and for phased-array systems was presented in chapter 2. The antenna gain, front-to-back ratio and H-plane patterns can be significantly enhanced with the use of a corrugated (magnetic) ground plane. Both antennas result in relatively wideband operation (10-20%), low cross-polarization levels, and very high measured radiation efficiency at 24 GHz ($> 93\%$). These planar antennas can be scaled to 77 GHz or 94 GHz for automotive radars and high data-rate communication systems.

Chapter 3 presented a microstrip-fed and differentially-fed millimeter-wave Yagi-Uda antennas at 24 GHz with applications as single element radiator or for switched-beam systems with medium gain (8-13 dB). The planar Yagi-Uda antennas can be arrayed for additional gain (+ 3 dB) and with low mutual coupling between the elements. The antennas result in relatively wideband operation (22-26 GHz), low cross-polarization levels, and high radiation efficiency, and can be scaled to 60 GHz, 77 GHz or 94 GHz for automotive radars and high data-rate communication systems.

Chapter 4 presented a comprehensive analysis and experimental characterization of 60 GHz Yagi-Uda antennas with shielding metal-planes. That the Yagi-Uda antenna performance is found to be enhanced with well designed shielding structures (metal-planes or boxes), and results in a gain improvement of 2 - 4 dB over the free-

space case (gain = 12 - 14 dB at 60 GHz). The Yagi-Uda antenna was also characterized in a practical environment with printed circuit boards, and showed no degradation in performance, which means it can be embedded inside complex platforms such as laptops with excellent performance.

Chapter 5 presented planar monopole antennas for mm-wave base-station applications. The monopole antenna is very wideband (18-42 GHz) with omni-directional radiation patterns but with a high cross-polarization level. The cross-polarization level can be reduced using $\lambda/4$-length folded sections and a magnetic ground plane, but at the expense of bandwidth. These designs can be extended to 60 GHz applications on the same Teflon substrate.

Chapter 6 presented the first on-chip high-efficiency mm-wave microstrip antenna to-date. The design is compatible with a variety of other antennas such as a differentially fed microstrip antenna, a slot-ring antenna, a double-slot antenna, all placed on the dielectric substrate. Also, the substrate need not be quartz, but can be Teflon, LTCC (ceramic), or even a high resistivity silicon wafer. The design can also be scaled to different frequencies such as 60 GHz or 140 GHz.

7.2 Future Work

Chapter 6 presented an electromagnetically coupled microstrip patch antenna on Silicon RFIC with highest on-chip antenna to date. The antenna has a measured S_{11} $<$ -10 dB at 91.7 - 92.5 GHz ($\sim$ 7% bandwidth). This work can still be extended and more antenna prototypes can be investigated and designed to achieve higher efficiencies and wider bandwidths. Possible antenna prototypes are slot-ring antennas, double-slot antennas or integrated horn antennas. The antenna presented in chapter 6 is also a microstrip-fed antenna compatible with single-ended RFIC. Differential versions of the antenna can be investigated for fully-differential RFIC's.

Appendix A

24 GHz Double-Dipole Antennas

The double-dipole antenna presented in Fig. A.1(a) consists of two dipoles with different lengths to achieve wide impedance matching bandwidth and stable unidirectional endfire radiation patterns [80]. The antenna is fabricated on a Teflon substrate (RT/duroid 5880) witha thickness of 15 mils (0.381 mm) and a dielectric constant ϵ_r = 2.2 A.1(b). The input impedance of the antenna is measured using GSG CPW probes and with microstrip-to-CPW transition. Standard TRL calibrations is used to take the effects of the microstrip-to-CPW transition. The double-dipole antenna has a measured S_{11} < -10 dB at 20 - 32 GHz (Fig. A.2). The measured S_{11} agrees well with Ansoft-HFSS simulations.

The measured and simulated E- and H-plane radiation patterns of the double-dipole antennas at 20, 24 and 28 GHz are presented in Fig. A.3. The gain of the double-dipole antenna is measured using absolute power measurement method and calculated from the Friis transmition formula. The antenna has a gain of $\sim$ 5 dB at 20 to 26 GHz (Fig. A.4).

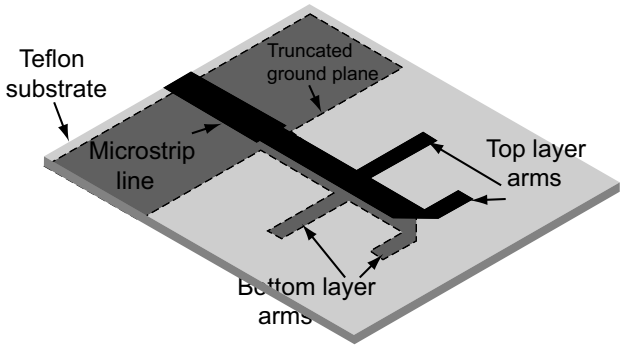

(a)

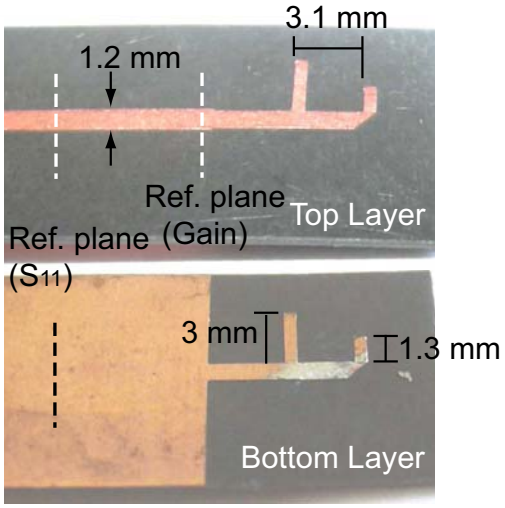

(b)

Figure A.1: 24 GHz double-dipole antenna: (a) geometry, (b) fabricated prototype.

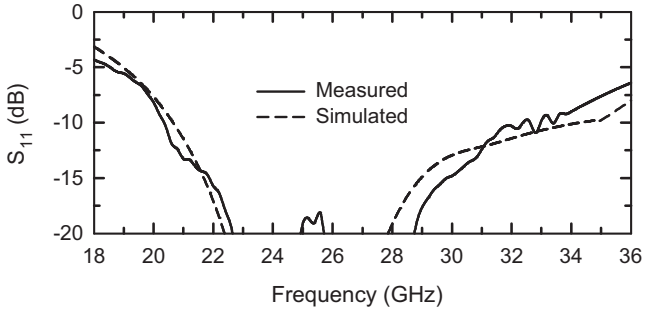

Figure A.2: Measured and simulated S_{11} of the double-dipole antenna.

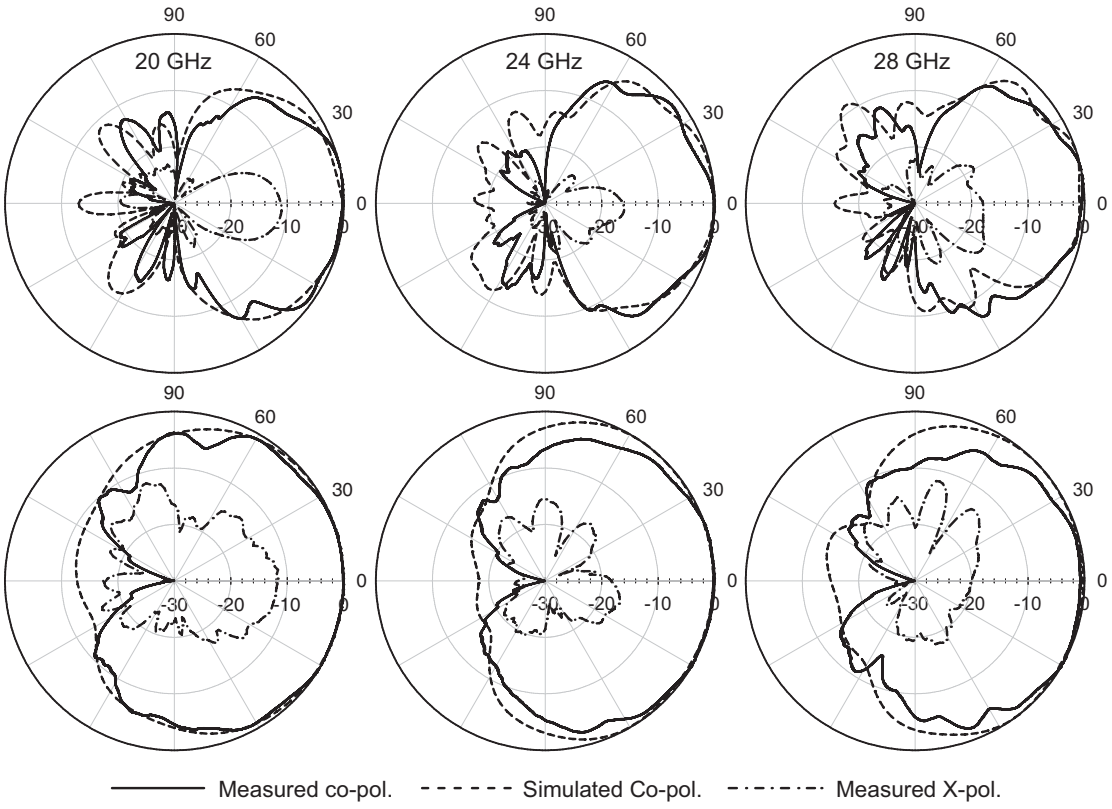

Figure A.3: E-plane (top) and H-plane (bottom) radiation patterns of the double-dipole antenna.

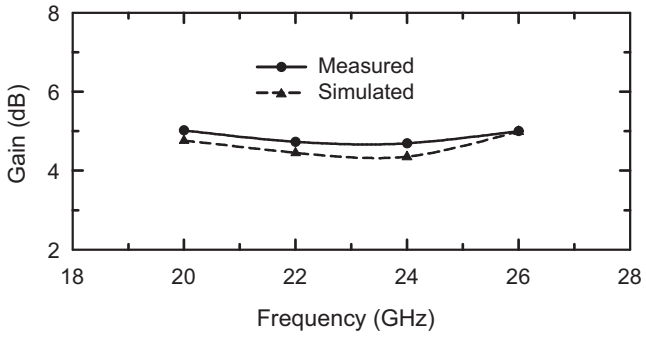

Figure A.4: Measured and simulated gain of the double-dipole antenna.

Appendix B

40 - 70 GHz Fermi Tapered Slot Antennas With Edge Corrugations

A 60 GHz fermi tapered slot antenna is presented in Fig. B.1(a). The antenna taper follows the relation [5]:

$$f(x) = \frac{0.5a}{1 + e^{-bx+c}} \tag{B.1}$$

The antenna is fabricated on a RT/duroid 5880 substrate with a 10 mils thickness and with $\epsilon_r = 2.2$. The antenna aperture (a) = 3.5 mm ($0.7\lambda_\circ$ at 60 GHz) and the antenna length is 20 mm ($4\lambda_\circ$ at 60 GHz). Edge corrugations are introduced in the ground plane edges to cotrol the current flow on the ground plane and have better radiation patterns with lower sidelobes.

The antenna is fed by a microstrip line using a microstrip-to-slot line transition. The antenna input impedance is measured with 2.4 mm connectors using a 67 GHz network analyzer. The measured S_{11} agrees well with HFSS simulations and is < -9 dB at 41 - > 67 GHz as shown in Fig. B.1(b). The impedance matching is limited by the microstrip-to-slot line transition.

The measured radiation patterns of the antenna at 56, 60 and 64 GHz are presented in Fig. B.2 and shows good agreement with simulations. The cross-polarization is mainly due to the bend in the microstrip feed line. The measured and simulated gain of the antenna are presented in Fig. B.3. The antenna has a gain > 10 dB at 45 - 63 GHz.

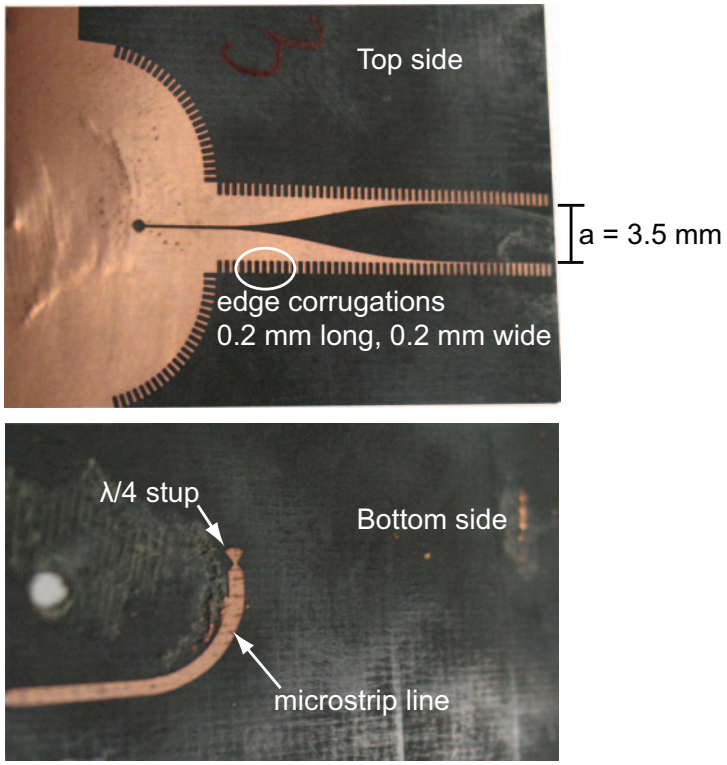

(a)

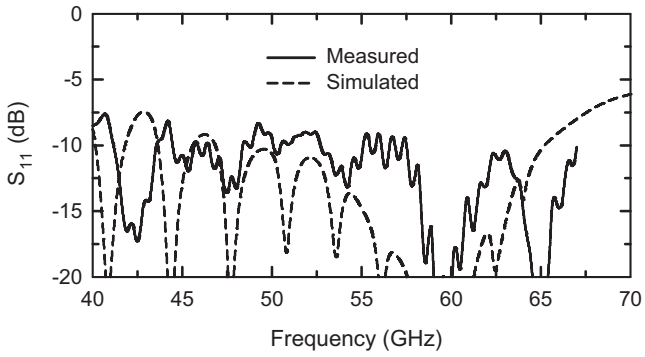

(b)

Figure B.1: 40 - 70 GHz Fermi tapered slot antenna (FTSA) with edge corrugations: (a) fabricated prototype, (b) measured and simulated S_{11}.

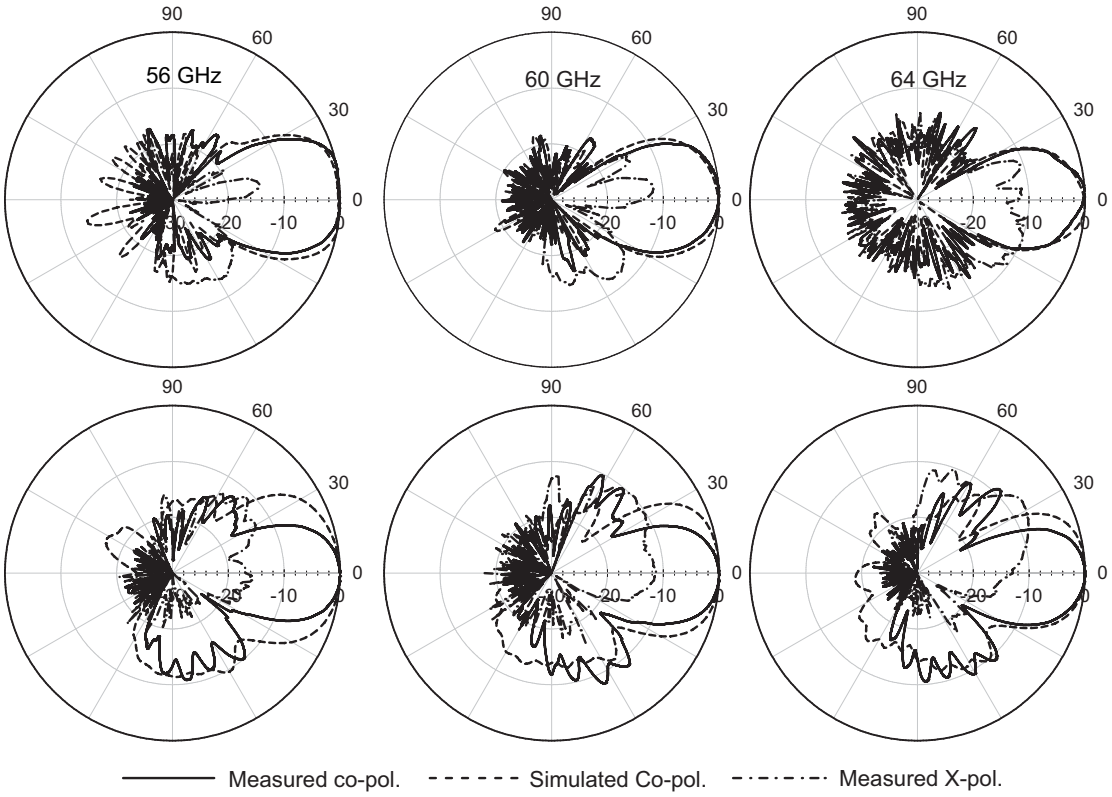

Figure B.2: E-plane (top) and H-plane (bottom) radiation patterns of the 40 - 70 GHz FTSA antenna.

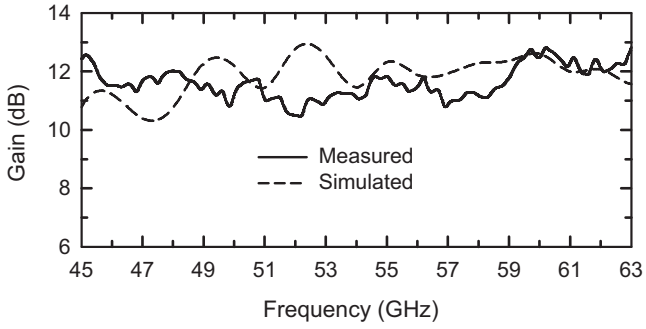

Figure B.3: Measured and simulated gain of the 40 - 70 GHz FTSA antenna.

Appendix C

Microstrip Line Loss at 24 GHz and 60 GHz

C.1 Introduction

Microstrip line is one of the most popular transmission lines used in planar circuits. It consists of two conductors printed on both sides of a thin supporting dielectric substrate (Fig. C.1). The top conductor is the signal trace while the bottom conductor is the microstrip ground plane. It can be easily fabricated using photolitheography and metal etching techniques. Due to the air/dielectric interface, microstrip lines can't

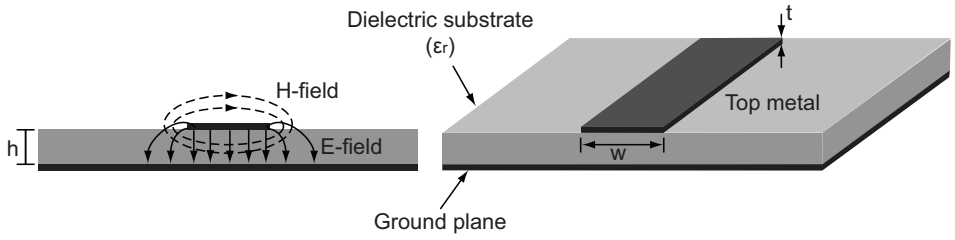

Figure C.1: Microstrip line configuration: front view and field distribution (left), 3-D geometry (right).

support pure TEM modes. However, because the longitudinal components of the E- and H-field are small, the microstrip line mode of operation is quasi-TEM mode. The upper frequency of operation is limited by the coupling into the TM_0 substrate mode which has a zero cut-off frequency. According to [81], the amount of coupling into the TM_0

mode becomes significant and can't be neglected for frequencies higher than:

$$f_c = \frac{ctan^{-1}(\varepsilon_r)}{\sqrt{2}\pi h\sqrt{\varepsilon_r - 1}} \tag{C.1}$$

C.2 Microstrip Line Loss

There are four mechanisms of loss in microstrip line: conduction losses, dielectric losses, radiation losses and surface wave losses.

C.2.1 Conduction Loss

The conduction loss in microstrip line is given by [81]:

$$\alpha_c = 0.072\frac{\sqrt{f}}{wZ_0}\lambda_g \tag{C.2}$$

and a more accurate curve fitted equation that takes the srface roughness into consideration is given by [81]:

$$\alpha_c^{'} = \alpha_c\left(1 + \frac{2}{\pi}tan^{-1}\left[1.4\left(\frac{\Delta}{\delta_s}\right)^2\right]\right) \tag{C.3}$$

where Δ is the rms surface roughness, δ_s is the skin depth, R_s is surface resistance and σ is the metal conductivity.

C.2.2 Dielectric Loss

Most dielectric materials have a very small loss tangent ($tan\delta \ll 1$). As a result, the dielectic loss is much smaller than conduction loss except for lossy substrates such as Silicon or Gallium Arsenide substrates. The dielectric loss in microstrip lines can be calculated from [81]:

$$\alpha_D = 27.3\frac{\varepsilon_r\left(\varepsilon_{eff} - 1\right)tan\delta}{\sqrt{\varepsilon_{eff}}\left(\varepsilon_r - 1\right)\lambda_0} \tag{C.4}$$

Radiation and surface wave losses can be minimized by reducing discontinuities and choosing thin substrates for building the microstrip lines. More details can be found in [81].

C.3 Measurements

A 50 Ω microstrip line on 15 mils (0.381 mm) Teflon substrate (RT/duroid 5880) with $\epsilon_r = 2.2$ has a trace width of $\sim$ 1.2 mm. The losses of the 50 Ω microstrip line

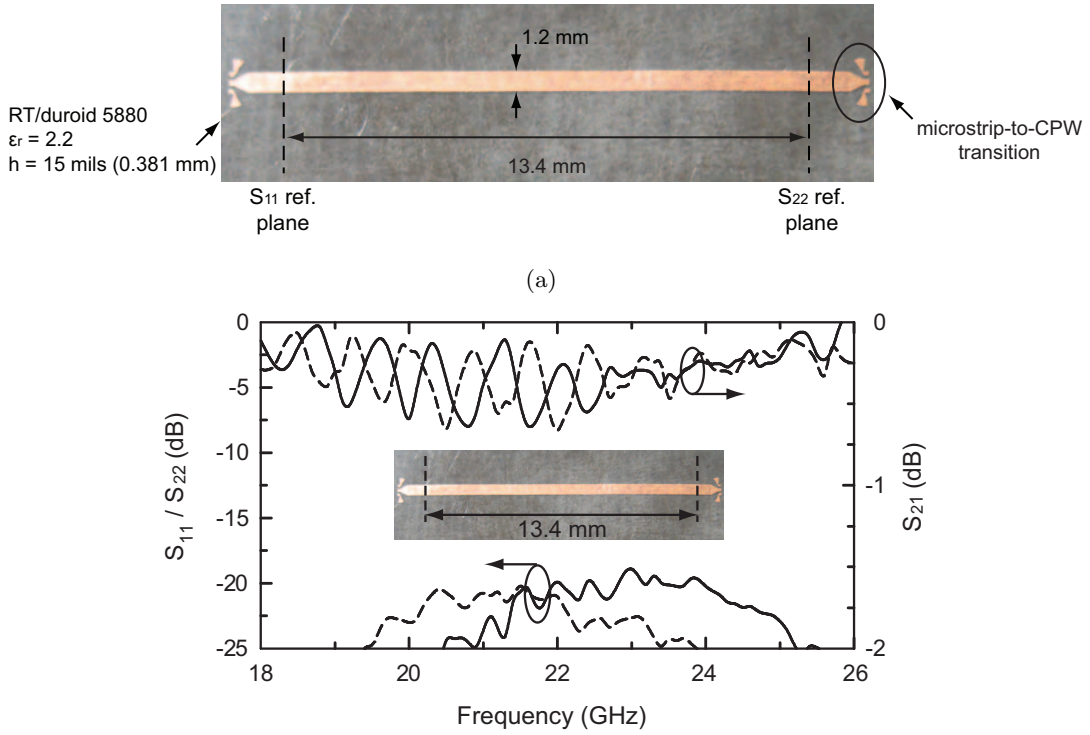

Figure C.2: (a) 50 Ω microstrip line with two microstrip-to-CPW transitions, (b) measured S-parameters.

were measured using the circuit shown in Fig. C.2(a). The S-parameters are measured with GSG probes using microstrip-to-CPW transition. Standard TRL calibrations were used to take out the effects of the microstrip-to-CPW transitions and move the reference planes to S_{11} and S_{22} ref. planes (Fig. C.2(a)). The total loss between S_{11} and S_{22} ref. planes of a 13.4 mm long 50 Ω microstrip line is calculated from the measured S-parameters using:

$$Loss = 10 * log\left(|S_{11}|^2 + |S_{21}|^2\right) \tag{C.5}$$

and the measured line loss is ∼ 0.22 dB/cm at 24 GHz.

On 10 mils (0.254 mm) Teflon substrate (RT/duroid 5880) with $\epsilon_r = 2.2$, the 50 Ω microstrip line has a trace width of ∼ 0.8 mm. The losses of a 50 Ω microstrip line were measured using the circuit in Fig. C.3(a). The measured S-parameters for two different microstrip line lengths (L = 17 mm and 33 mm) are presented in Fig. C.3(b). The total

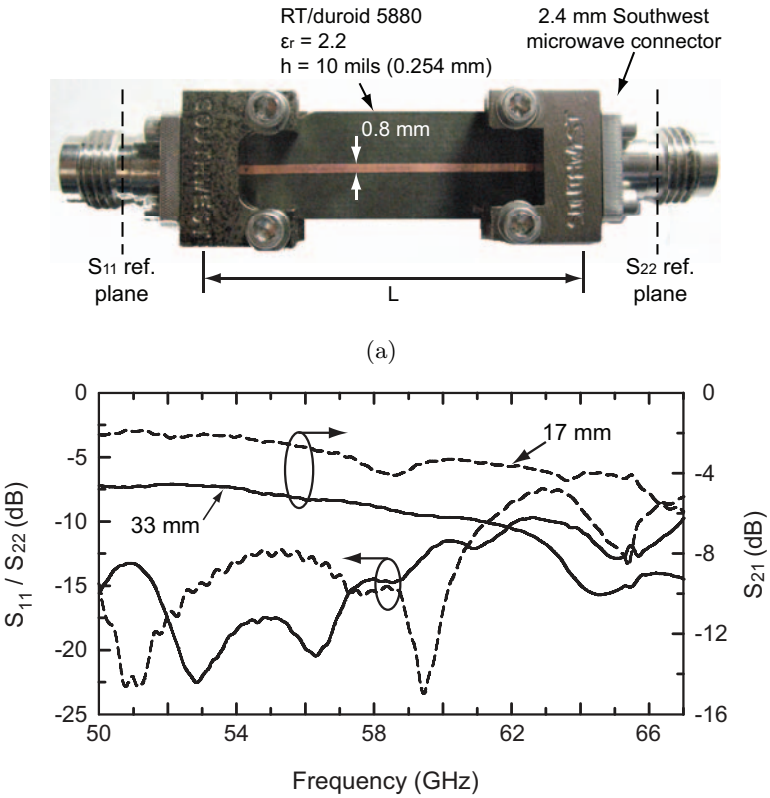

Figure C.3: (a) 50 Ω microstrip line with two microstrip to coaxial transitions (2.4 mm connectors), (b) measured S-parameters for two different lengths of microstrip line.

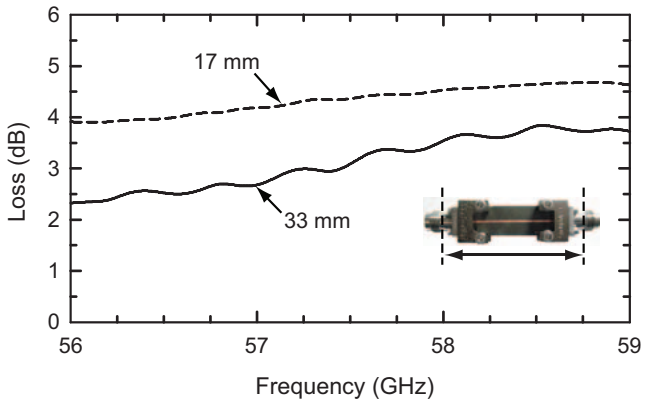

Figure C.4: Measured total loss between S_{11} and S_{22} ref. planes for L = 17 mm and L = 33 mm.

loss between S_{11} and S_{22} ref. planes is then calculated for both cases using equation C.5 and the calculated loss is presented in Fig. C.4 at 56 - 59 GHz. By subtracting the total

loss between S_{11} and S_{22} ref. planes for L = 17 mm from the total loss for L = 33 mm and then divide the result by 1.6, we get the loss of the microstrip line in dB/cm. The measured loss of a 50 Ω microstrip (W = 0.8 mm) on 10 mils (0.254 mm) RT/duroid 5880 (ϵ_r = 2.2) substrate, has an average value of 0.76 dB/cm at 56 - 59 GHz which agrees well with HFSS predicted line loss of 0.6 dB/cm. By subtracting the microstrip line loss from the total measured loss between S_{11} and S_{22} ref. planes, we get the losses of the two 2.4 mm microwave connectors. The 2.4 mm connector has a loss of $\sim$ 0.9 dB at 60 GHz.

Appendix D

Radiation Patterns and Absolute Gain Measurement Setups

D.1 Radiation Patterns Measurement Setup

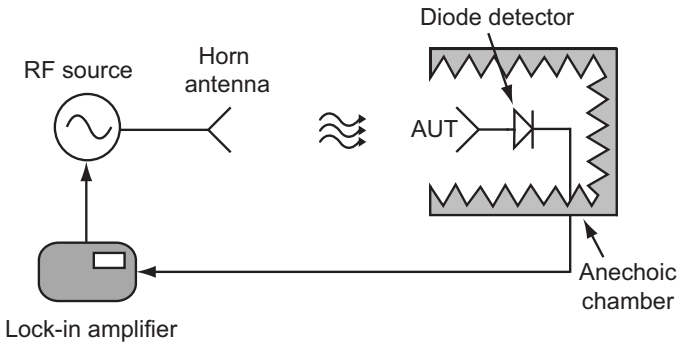

Figure D.1: Block diagram of the radiation pattern measurement setup.

Fig. D.1 shows a block diagram of the radiation patterns measurements setup. The radiation patterns of antenna under test (AUT) are measured in the receive mode. The RF signal is amplitude modulated with a low frequency signal from the lock-in amplifier the RF modulated signal is transmitted through a standard gain horn antenna. The received signal from the antenna under test is detected using a schottky diode detector which can be a planar diode detector mounted on the same board with the antenna or a coaxial diode detector attached to the antenna using a coaxial connector. The detected low frequency signal is then measured using the lock-in amplifier. The

anechoic chamber and the radiation patterns measurement setup is ahown in Fig.

D.2 Absolute Gain Measurements

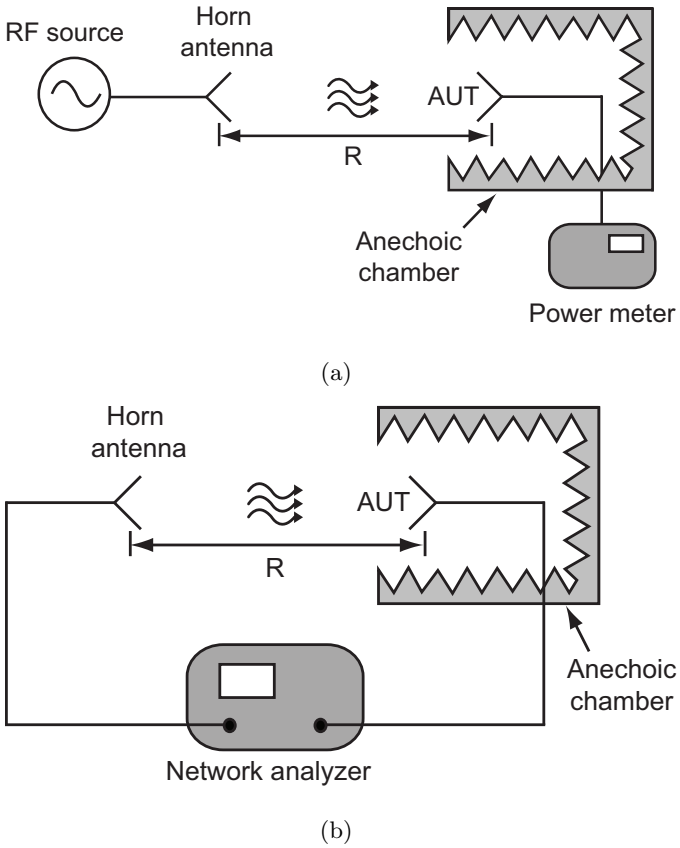

Figure D.2: Block diagram of the antenna absolute gain measurements: (a) using absolute power measurements with calibrated power meter, (b) using the gain transfer method with network analyzer.

The antenna absolute gain can be measured using pure power measurement with a power meter as shown in Fig. D.2(a). The radiating antenna is a standard gain horn antenna with a pre-measured gain. The gain of the antenna under test is then calculated from Friis transmission formula:

$$P_r = P_t G_t G_r \left(\frac{\lambda}{4\pi R}\right)^2 \tag{D.1}$$

where after measuring P_r and P_t, the only unknown is the gain of the antenna under test G_r and can be easily calculated. All the losses between the RF source and the

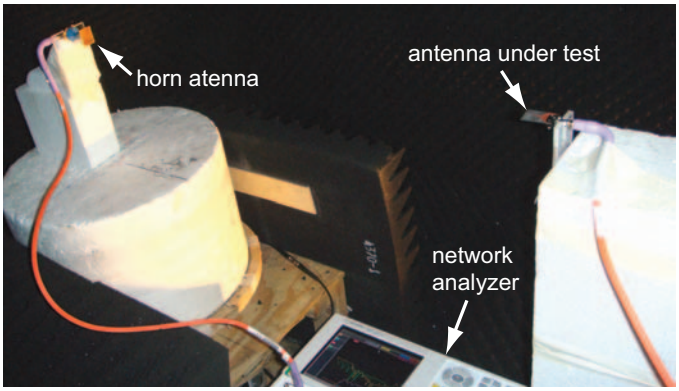

Figure D.3: Antenna gain measurement setup using gain transfer method with network analyzer.

transmitting antenna and between the antenna under test and the power meter, including connector and antenna feeding line losses, are calibrated out from the measured gain.

The antenna gain can also be measured using the gain transfer method with network analyzer (Fig. D.2(b)). Two identical horn antennas are first connected to the two ports of the network analyzer. Their gain is calculated from the measured S_{21} using Friis formula (see D.1). One antenna is then replaced by antenna under test and the gain of the antenna under test is calculated from the horn antenna gain and the difference in the measured S_{21} in both cases. A picture of the antenna gain setup with a network analyzer is presented in Fig. D.3.

Bibliography

[1] K. Yngvesson, D. Schaubert, T. Korzeniowski, E. Kollberg, T. Thungren, and J. Johansson, "Endfire tapered slot antennas on dielectric substrates," *IEEE Transactions on Antennas and Propagation*, vol. 33, no. 12, pp. 1392 – 1400, December 1985.

[2] K. Yngvesson, T. L. Korzentowski, Y. Kim, E. L. Kollberg, and J. F. Johansson, "The tapered slot antenna - a new integrated element for millimeter-wave applications," *IEEE Transactions on Microwave Theory and Techniques*, vol. 37, no. 2, pp. 365 – 374, February 1989.

[3] S. Sugawara, Y. Maita, K. Adachi, K. Mori, and K. Mizuno, "A mm-wave tapered slot antenna with improved radiation pattern," *IEEE MTT-S International Microwave Symposium Digest*, vol. 2, pp. 959 – 962, 1997.

[4] ——, "Characteristics of a MM-wave tapered slot antenna with corrugated edges," *IEEE MTT-S International Microwave Symposium Digest*, vol. 2, pp. 533 – 536, 1998.

[5] H. Sato, K. Sawaya, Y. Wagatsuma, and K. Mizuno, "Design of narrow-width Fermi antenna with circular radiation pattern," *IEEE Antennas and Propagation Society International Symposium*, vol. 4, pp. 4312 – 4315, 2004.

[6] J. B. Rizk and G. M. Rebeiz, "Millimeter-wave Fermi tapered slot antennas on micromachined silicon substrates," *IEEE Transactions on Antennas and Propagation*, vol. 50, no. 3, pp. 379 – 383, March 2002.

[7] B. Schoenlinner, X. Wu, J. P. Ebling, G. V. Eleftheriades, and G. M. Rebeiz, "Wide-scan spherical-Lens antennas for Automotive Radars," *IEEE Transactions on Microwave Theory and Techniques*, vol. 50, no. 9, pp. 2166–2175, Sept. 2002.

[8] L. Pazin and Y. Leviatan, "A compact 60 GHz tapered slot antenna printed on LCP substrate for WPAN applications," *IEEE Antennas and Wireless Propagation Letters*, 2010.

[9] W. R. Deal, N. Kaneda, J. Sor, Y. Qian, and T. Itoh, "A new quasi-Yagi antenna for planar active antenna arrays," *IEEE Trans. Microwave Theory and Tech*, vol. 48, no. 6, pp. 910–918, June 2000.

[10] N. Kaneda, W. R. Deal, Y. Qian, R. Waterhouse, and T. Itoh, "A Broad-band planar Quasi-Yagi antenna," *IEEE Trans. Antennas and Propagation*, vol. 50, no. 8, pp. 1158–1160, Aug. 2002.

[11] P. R. Grajek, B. Schoenlinner, , and G. M. Rebeiz, "A 24-GHz high-gain Yagi-Uda antenna array," *IEEE Trans. Antennas and Propagation*, vol. 52, pp. 1257–1261, May 2004.

[12] G. Zheng, A. A. Kishk, A. B. Yakovlev, and A. W. Glisson, "Simplified feed for a modified printed Yagi antenna," *Electronics Letters*, vol. 40, no. 8, pp. 464–465, April. 2004.

[13] Y. Lee and S. Chung, "Design of a 38-GHz printed Yagi antenna with multiple directors," *IEEE Antennas and Propagation Symposium*, vol. 3, pp. 606–609, July 2001.

[14] G. M. Rebeiz, D. P. Kasilingam, Y. GUO, P. A. Stimson, and D. B. Rutledge, "Monolothic Millimeter-Wave Two-Dimensional Horn Imaging Arrays," *IEEE Transactions on Antennas and Propagation*, vol. 38, no. 9, pp. 1473 – 1482, 1990.

[15] G. V. Eleftheriades, W. Y. Ali-Ahmad, L. Katehi, and G. M. Rebeiz, "Millimeter-wave integrated-horn antennas. I. Theory," *IEEE Transactions on Antennas and Propagation*, vol. 39, no. 11, pp. 1575–1581, 1991.

[16] W. Y. Ali-Ahmad, G. V. Eleftheriades, L. Katehi, and G. M. Rebeiz, "Millimeter-wave integrated-horn antennas. II. Experiment," *IEEE Transactions on Antennas and Propagation*, vol. 39, no. 11, pp. 1582–1586, 1991.

[17] W. Y. Ali-Ahmad and G. M. Rebeiz, "92 GHz dual-polarized integrated horn antennas," *IEEE Transactions on Antennas and Propagation*, vol. 39, no. 6, pp. 820–825, 1991.

[18] G. V. Eleftheriades and G. M. Rebeiz, "Design and analysis of quasi-integrated horn antennas for millimeter and submillimeter-wave applications," *IEEE Transactions on Microwave Theory and Techniques*, vol. 41, no. 6, pp. 954 – 965, 1993.

[19] H. Kazemi, C. Nguyen, B. Brar, G. M. Rebeiz, G. Nagy, L. Tran, A. Young, and E. R. Brown, "Low cost modular integrated horn antenna array using heterojunction barrier diode detectors," *IEEE MTT-s International Microwave Symposium Digest*, pp. 297 – 300, June 2008.

[20] V. Douvalis, Y. Hao, and C. G. Parini, "A monolithic active conical horn antenna array for millimeter and submillimeter wave applications," *IEEE Transactions on Antennas and Propagation*, vol. 54, no. 5, pp. 1393 – 1398, May 2006.

[21] K. Huang and Z. Wang, "Millimeter-wave circular polarized beam-steering antenna array for Gigabit wireless communications," *IEEE Transactions on Antennas and Propagation*, vol. 54, no. 2, pp. 743 – 746, February 2006.

[22] B. Pan, Y. Li, G. E. Ponchak, J. Papapolymerou, and M. M. Tentzeris, "A 60-GHz CPW-fed high-gain and broadband integrated horn antenna," *IEEE Transactions on Antennas and Propagation*, vol. 57, no. 4, pp. 1050 – 1056, April 2009.

[23] J. Grzyb, D. Liu, U. Pfeiffer, and B. Gaucher, "Wideband cavity-backed folded dipole superstrate antenna for 60 GHz applications," *IEEE Antennas and Propagation Society International Symposium*, pp. 3939 – 3942, July 2006.

[24] T. Zwick, D. Liu, and B. P. Gaucher, "Broadband planar superstrate sntenna for integrated millimeterwave transceivers," *IEEE Transactions on Antennas and Propagation*, vol. 54, no. 10, pp. 2790 – 2796, October 2006.

[25] Y. Zhang, M. Sun, and L. Guo, "On-chip antennas for 60 GHz radios in silicon technology," *IEEE Trans. Electron Devices*, vol. 52, no. 7, pp. 1664–1668, July 2005.

[26] H. Chuang, S. Kuo, C. Lin, and L. Kuo, "A 60 GHz millimeter-wave CMOS RFIC-on-chip dipole antenna," *Microwave Journal*, vol. 50, no. 1, p. 144, January 2007.

[27] A. Shamim, L. Roy, N. Fong, and N. G. Tarr, "24 GHz On-chip antennas and balun on bulk Si for air transmission," *IEEE Transactions on Antennas and Propagation*, vol. 56, no. 2, pp. 303 – 311, February 2008.

[28] C.-C. Lin, S.-S. Hsu, C.-Y. Hsu, and H.-R. Chuang, "A 60-GHz millimeter-wave CMOS RFIC-on-chip triangular monopole antenna for WPAN applications," *IEEE Antennas and Propagation Society International Symposium*, pp. 3939 – 3942, July 2006.

[29] I.-S. Chen, H.-K. Chiou, and N.-W. Chen, "V-band on-chip dipole-based antenna," *IEEE Transactions on Antennas and Propagation*, vol. 57, no. 10, pp. 2853 – 2861, October 2009.

[30] J. Hirokawa, K. Kimishima, M. Ando, and Y. Hirachi, "Dipole antenna on thick resin layer on the back side of silicon chip at 60 GHz," *Proceedings of the 39th European Microwave Conference*, vol. 57, no. 12, pp. 528–531, 2009.

[31] S. T. Nicolson, A. Tomkins, K. Tang, A. Cathelin, D. Belot, and S. P. Voinigescu, "A 1.2 V, 140 GHz receiver with on-die antenna in 65 nm CMOS," *IEEE Radio Frequency Integrated Circuits Symposium*, pp. 229 – 232, 2008.

[32] Y. Tsutsumi, M. Nishio, S. Sekine, H. Shoki, and T. Morooka, "A triangular loop antenna mounted adjacent to a lossy Si substrate for millimeter-wave wireless PAN," *IEEE Antennas and Propagation Society International Symposium*, pp. 1008–1011, June 2007.

[33] H. Wu, M. Tekle, C. Nallani, N. Zhang, and K. K. O, "Bond-wire antenna/feed for operation near 60 GHz," *IEEE Trans. Microwave Theory Techniques*, vol. 57, no. 12, pp. 2966–2972, Dec. 2009.

[34] R. Willmot, D. Kim, and D. Peroulis, "Yagi-Uda array of high-efficiency wire-bond antennas for on-chip radio applications," *IEEE Trans. Microwave Theory Techniques*, vol. 57, no. 12, pp. 3315–3321, Dec. 2009.

[35] A. A. Eldek, A. Z. Elsherbeni, and C. E. Smith, "Wide-band modified printed bow-tie antenna with single and dual polarization for C and X-band applications," *IEEE Trans. Antennas and Propagation*, vol. 5, no. 9, pp. 3067–3070, Sept. 2005.

[36] G.-Y. Chen and J.-S. Sun, "Printed dipole antenna with microstrip tapered balun," *Microwave Opt. Tech. Lett.*, vol. 40, no. 4, pp. 344–346, February 2004.

[37] G. Zheng, A. A. Kishk, A. B. Yakovlev, and A. W. Glisson, "A broad band printed bow-tie antenna with a simplified feed," *Antennas and Propagation Society International Symposium*, vol. 4, pp. 4024–4027, June 2004.

[38] J. Sowers, N. Byer, B. Edward, D. McPherson, S. Weinreb, and F. Rucky, "Electronically steered, receive monopulse, active phased array at 94 GHz," *IEEE MTT-S International Microwave Symposium Digest*, vol. 3, pp. 1581–1584, June 1996.

[39] *Ansoft HFSS11*, www.ansoft.com, Ansoft Corporation Inc., Pittsburgh, Pennsylvania.

[40] www.southwestmicrowave.com, Southwest Microwave Inc., Tempe, Arizona.

[41] www.dorado-intl.com, Dorado International, Seattle, Washington.

[42] www.agilent.com, Agilent Technologies Inc., Santa Clara, California.

[43] C. Y. Hang, W. R. Deal, Y. Qian, and T. Itoh, "High-Efficiency push-pull power amplifier integrated with Quasi-Yagi antenna," *IEEE Trans. Microwave Theory and Tech*, vol. 49, no. 6, pp. 1155–1161, June 2001.

[44] L. Zhu and K. Wu, "Model-based characterization of CPS-fed printed dipole for innovative design of uniplanar integrated antenna," *IEEE Microwave and Guided wave letters*, vol. 9, no. 9, pp. 342–344, Sept. 1999.

[45] G. R. DeJean and M. M. Tentzeris, "A new high-gain microstrip Yagi array antenna awth a high front-to-back (F/B) ratio for WLAN and millimeter-wave applications," *IEEE Trans. Antennas and Propagation*, vol. 55, pp. 298–304, Feb. 2007.

[46] D. Woo, Y. Kim, K. Kim, and Y. Cho, "A simplified design of Quasi-Yagi antennas using the new microstrip-to-CPS transitions," *IEEE Antennas and Propagation Symposium*, pp. 781–784, June 2007.

[47] H. K. Kan, R. B. Waterhouse, A. M. Abbosh, and M. E. Bialkowski, "Simple broadband planar CPW-fed Quasi-Yagi antenna," *IEEE Antennas and Wireless Propagation Letters*, vol. 6, pp. 18–20, 2007.

[48] S. Hsu, K. Wei, C. Hsu, and R. Chuang, "A 60-GHz Millimeter-wave CPW-fed Yagi antenna fabricated by using 0.18-m CMOS technology," *IEEE Electron Device Lett*, vol. 29, pp. 625–627, June 2008.

[49] W. L. Stutzman and G. A. Thiele, *Antenna Theory and Design*. New York: Wiley, 1998.

[50] A. Tomkins, R. A. Aroca, T. Yamamoto, S. T. Nicolson, Y. Doi, and S. P. Voinigescu, "A zero-IF 60 GHz 65 nm CMOS transceiver with direct BPSK modulation demonstrating up to 6 Gb/s data rates over a 2 m wireless link," *IEEE Journal of Solid-State Circuits*, vol. 44, no. 8, pp. 42 085 – 2099, August 2009.

[51] S. Reynolds, B. A. Floyd, U. R. Pfeiffer, T. Beukema, J. Grzyb, C. Haymes, B. Gaucher, and M. Soyuer, "A silicon 60 GHz receiver and transmitter chipset for broadband communications," *IEEE J. Solid-State Circuits*, vol. 41, no. 12, pp. 2820–2831, December 2006.

[52] M. Tanomura, Y. Hamada, S. Kishimoto, M. Ito, N. Orihashi, K. Maruhashi, and H. Shimawaki, "TX and RX front-ends for 60 GHz band in 90nm standard bulk CMOS," *IEEE ISSCC Dig. Tech. Papers*, pp. 558–559, February 2008.

[53] T. Mitomo, R. Fujimoto, N. Ono, R. Tashibana, H. Hoshino, Y. Yoshihara, Y. Tsutsumi, and I. Seto, "A 60 GHz CMOS receiver front-end with frequency synthesizer," *IEEE J. Solid-State Circuits*, vol. 43, no. 4, pp. 2820–2831, April 2008.

[54] W. Shin, M. Uzunkol, and G. M. Rebeiz, "Ultra low power 60 GHz ASK receiver with 3-6 GBPS capabilities," *IEEE Compound Semiconductor Integrated Circuit Symposium*, pp. 1–4, October 2009.

[55] J. Lee, Y. Chen, and Y. Huang, "A low-power low cost fully-integrated 60-GHz transceiver system with OOK modulation and on-board antenna assembly," *IEEE Journal of Solid-State Circuits*, vol. 45, no. 2, pp. 264 – 275, February 2010.

[56] J.-H. Lee, N. Kidera, S. Pinel, J. Laskar, and M. Tentzeris, "60 GHz high-gain aperture-coupled microstrip antennas using soft-surface and stacked cavity on LTCC multilayer technology," *IEEE International Symposium. on Antennas and Propagation*, pp. 1621–1624, July 2006.

[57] A. Lamminen, A. Vimpari, and J. Saily, "UC-EBG on LTCC for 60-GHz frequency band antenna applications," *IEEE Transactions on Antennas and Propagation*, vol. 57, no. 10, pp. 2904 – 2912, October 2009.

[58] S. Holzwarth and L. Baggen, "Planar antenna design at 60 GHz for high date rate point-to-point connections," *IEEE Antennas and Propagation Symposium*, vol. 1A, pp. 346–349, July 2005.

[59] C. Karnfelt, P. Hallbjorner, H. Zirath, and A. Alping, "High gain active microstrip antenna for 60-GHz WLAN/WPAN applications," *IEEE Trans. on Microwave Theory and Techniques*, vol. 54, no. 6, pp. 2593–2603, June 2006.

[60] K. Jeong-Geun, L. H. Suk, L. Ho-Seon, A. J.-B. Yoon, , and S. Hong, "60-GHz CPW-fed post-supported patch antenna using micromachining technology," *IEEE Microwave and Wireless Components Letters*, vol. 15, pp. 635–637, 2005.

[61] M. Barakat, C. Delaveaud, and F. Ndagijimana, "Performance of a 0.13 μm SOI integrated 60 GHz dipole antenna," *IEEE Antennas and Propagation International Symposium*, pp. 2526–2529, June 2007.

[62] R. A. Alhalabi and G. M. Rebeiz, "High-efficiency endfire angled-dipole antennas for millimeter-wave phased array applications," *IEEE Transactions on Antennas and Propagation*, vol. 56, no. 10, pp. 3136–3142, October 2008.

[63] D. Neculoin, G. Konstantinidis, L. Bary, D. Vasilache, A. Stavrinidis, Z. Hazopulos, A. Pantazis, R. Plana, and A. Muller, "Yagi-Uda antennas fabricated on thin GaAs membrane for millimeter wave applications," *IEEE International Workshop on Antenna Technology*, pp. 418–421, March 2005.

[64] R. A. Alhalabi and G. M. Rebeiz, "High-gain Yagi-Uda antennas for millimeter-wave switched-beam systems," *IEEE Transactions on Antennas and Propagation*, vol. 57, no. 11, pp. 3672–3676, November 2009.

[65] ——, "Differentially-fed millimeter-wave Yagi-Uda antennas with folded dipole feed," *IEEE Transactions on Antennas and Propagation*, vol. 58, no. 3, pp. 966 – 969, March 2010.

[66] Y. A. Atesal, B. Cetinoneri, and G. M. Rebeiz, "Low-loss 0.13 m CMOS 50-70 GHz SPDT and SP4T switches," *IEEE Radio Frequency Integrated Circuits Symposium*, pp. 43 – 46, June 2009.

[67] J. Johnson and Y. Rahmat-Samii, "The tab monopole," *IEEE Trans. Antennas and Propagation*, vol. 45, no. 1, pp. 187–188, January 1997.

[68] H. M. Chen, "Microstrip-fed dual frequency printed triangular monopole," *Electronics Letters*, vol. 38, no. 13, pp. 619–620, June 2002.

[69] C. Lin, Y. Kan, L.Kuo, and H.Chuang, "A planar triangular monopole antenna for UWB communication," *IEEE Microwave and Components Letters*, vol. 15, no. 10, pp. 624–626, October 2005.

[70] S. Suh, W. Stutzman, and W. Davis, "A new ultra wide band printed monopole antenna: the planar inverted cone antenna (PICA)," *IEEE Trans. Antennas and Propagation*, vol. 52, no. 5, pp. 1361–1364, May 2004.

[71] Y. Lin and K. Hung, "Compact ultrawideband rectangular aperture antenna and band-notched designs," *IEEE Trans. Antennas and Propagation*, vol. 54, no. 11, pp. 3075–3081, November 2006.

[72] N. P. Agrawall, G. Kumar, and K. P. Ray, "Wideband planar monopole antennas," *IEEE Trans. Antennas and Propagation*, vol. 46, no. 2, pp. 294–295, February 1998.

[73] A. M. Abbosh and M. E. Bialkowski, "Design of Ultra-wideband Planar Monopole Antennas of Circular and Elliptical Shape," *IEEE Trans. Antennas and Propagation*, vol. 56, no. 1, pp. 17–23, January 2008.

[74] G. M. Rebeiz, "Millimeter-wave and terahertz integrated circuit antennas," *Proceedings of the IEEE*, vol. 80, pp. 1748–1770, Nov. 1992.

[75] N. G. Alexopoulos, P. B. Katehi, and D. B. Rutledge, "Substrate optimization for integrated circuit antennas," *IEEE Trans. Microwave Theory and Techniques*, vol. 31, no. 7, pp. 550–557, July 1983.

[76] C. Cao, Y. Ding, X. Yang, J.-J. Lin, H. Wu, A. Verma, J. Lin, F. Martin, and K. K. O, "A 24 GHz transmitter with on-chip dipole antenna in 0.13-m CMOS," *IEEE J. Solid-state Circuits*, vol. 43, no. 6, pp. 1394–1402, June 2008.

[77] R. Garg, P. Bhartia, I. Bahl, and A. Ittipiboon, *Microstrip Antenna Design Handbook*. Artech House, 2001.

[78] *BiCMOS 8HP design manual*, IBM Microelectronics Division, Essex Junction, VT, July 2007.

[79] H. Oltman and D. Huebner, "Electromagnetically coupled microstrip dipoles," *IEEE Transactions on Antennas and Propagation*, vol. 29, no. 1, pp. 151–157, January 1981.

[80] A. A. Eldek, "Double dipole antenna for wideband phased array applications ," *IEEE International Workshop on Antenna Technology Small Antennas and Novel Metamaterials*, pp. 273–276, March 2006.

[81] T. C. Edwards and M. B. Steer, *Foundations of Interconnect and Microstrip Design*, 3rd ed. John Wieley and Sons, Ltd, 2000.